

Spring 2002

Experimental and theoretical study of an integrated silicon Mach-Zehnder interferometer for chemical sensing applications

Yew Fong Hor

New Jersey Institute of Technology

Follow this and additional works at: <https://digitalcommons.njit.edu/dissertations>



Part of the [Other Physics Commons](#)

Recommended Citation

Hor, Yew Fong, "Experimental and theoretical study of an integrated silicon Mach-Zehnder interferometer for chemical sensing applications" (2002). *Dissertations*. 529.

<https://digitalcommons.njit.edu/dissertations/529>

This Dissertation is brought to you for free and open access by the Theses and Dissertations at Digital Commons @ NJIT. It has been accepted for inclusion in Dissertations by an authorized administrator of Digital Commons @ NJIT. For more information, please contact digitalcommons@njit.edu.

Copyright Warning & Restrictions

The copyright law of the United States (Title 17, United States Code) governs the making of photocopies or other reproductions of copyrighted material.

Under certain conditions specified in the law, libraries and archives are authorized to furnish a photocopy or other reproduction. One of these specified conditions is that the photocopy or reproduction is not to be “used for any purpose other than private study, scholarship, or research.” If a user makes a request for, or later uses, a photocopy or reproduction for purposes in excess of “fair use” that user may be liable for copyright infringement,

This institution reserves the right to refuse to accept a copying order if, in its judgment, fulfillment of the order would involve violation of copyright law.

Please Note: The author retains the copyright while the New Jersey Institute of Technology reserves the right to distribute this thesis or dissertation

Printing note: If you do not wish to print this page, then select “Pages from: first page # to: last page #” on the print dialog screen

The Van Houten library has removed some of the personal information and all signatures from the approval page and biographical sketches of theses and dissertations in order to protect the identity of NJIT graduates and faculty.

ABSTRACT

EXPERIMENTAL AND THEORETICAL STUDY OF AN INTEGRATED SILICON MACH-ZEHNDER INTERFEROMETER FOR CHEMICAL SENSING APPLICATIONS

**by
Yew Fong Hor**

This thesis involves the design, fabrication and characterization of an integrated optical waveguide sensor. Prior to fabrication, design parameters of the waveguide need to be determined and optimized. The waveguide parameters such as waveguide dimension and the refractive index of the core and cladding are obtained from the single-mode cutoff frequency calculated using either analytical or numerical methods. In this thesis, details of analytical calculations to determine the cutoff frequency in terms of the waveguide parameters will be presented. The method discussed here is Marcatili's approximation. The purpose is to solve the scalar wave equation derived from Maxwell's equations because it describes the mode properties inside the waveguides. The Finite Element Method is used to simulate the electric and magnetic fields inside the waveguides and to determine the propagation characteristics in optical waveguides. This method is suited for problems involving complicated geometries and variable index of refraction.

Fabrication of the Integrated Mach-Zehnder Interferometer sensor involves several important standard processes such as Chemical Vapor Deposition (CVD) for thin film fabrication, photolithography for mask transfer, and etching for ridge waveguide formation. The detailed fabrication procedures of the tested Mach-Zehnder Interferometer sensors are discussed.

After completion of the sensor fabrication processes, the characterizations were carried out for the thin film of SiO₂ and PSG, the waveguides and the Y-junction separately. The waveguides were analyzed to make sure that the sensors are working as expected. The experimental testing on the separated waveguide portions of the first batch Integrated Mach-Zehnder Interferometer (MZI) sensors are described. These testing procedures were also performed for the subsequent fabricated batches of the integrated MZI sensors until optimum performance is achieved.

A new concept has been proposed for chemical sensing applications. The novelty of the approach is mainly based on utilizing the multi-wavelength or broadband source instead of single wavelength input to the integrated MZI. The shifting of output spectra resulting from the interference has shown the ability of the MZI to analyze the different concentrations of a chemical analyte. The sensitivity of the sensor is also determined from the plot of intensity versus concentration, which is around 0.013 (%ml)⁻¹ and 0.007 (%ml)⁻¹ for the white light source and the 1.5 μm broadband source, respectively, while the lowest detectable concentration of ethanol for the sensor detection is around 8% using a intensity variation method and 0.6% using a peak wavelength variation method.

**EXPERIMENTAL AND THEORETICAL STUDY OF
AN INTEGRATED SILICON MACH-ZEHNDER INTERFEROMETER
FOR CHEMICAL SENSING APPLICATIONS**

**By
Yew Fong Hor**

**A Dissertation
Submitted to the Faculty of
New Jersey Institute of Technology and
Rutgers, The State University of New Jersey - Newark
In Partially Fulfillment of the Requirement for the Degree of
Doctor of Philosophy in Applied Physics**

Federated Department of Physics

May 2002

Copyright © 2002 by Yew Fong Hor

ALL RIGHTS RESERVED

APPROVAL PAGE

EXPERIMENTAL AND THEORETICAL STUDY OF AN INTEGRATED SILICON MACH-ZEHNDER INTERFEROMETER FOR CHEMICAL SENSING APPLICATIONS

Yew Fong Hor

Dr. John F. Federici, Dissertation Advisor Associate Chair and Professor of Applied Physics Department, NJIT Professor of Biomedical Engineering Department, NJIT	Date
--	------

Dr. Kenneth B. Farmer, Committee Member Associate Professor of Applied Physics Department, NJIT Director, Microelectronics Research Center, NJIT	Date
---	------

Dr. Nuggehalli M. Ravindra, Committee Member Professor of Applied Physics Department, NJIT	Date
---	------

Dr. Pushpendra Singh, Committee Member Associate Professor of Mechanical Engineering Department, NJIT	Date
--	------

Dr. Haimin Wang, Committee Member Professor of Applied Physics Department, NJIT Associate Director, Big Bear Solar Observatory, NJIT	Date
---	------

BIOGRAPHICAL SKETCH

Author: Yew Fong Hor
Degree: Doctor of Philosophy
Date: May 2002

Undergraduate and Graduate Education:

- Doctor of Philosophy in Applied Physics,
New Jersey Institute of Technology, Newark, NJ, May 2002
- Master of Science in Physics
Western Illinois University, Macomb, IL, May 1997
- Bachelor of Science in Microelectronics and Physics,
Campbell University, Buies Creek, NC, July 1994

Major: Applied Physics

Publications and Presentations:

D. H. Luo, Y. F. Hor, J. F. Federici, R. A. Levy
“An Integrated Photonic Sensor for In-situ Monitoring of Hazardous Emissions”,
(submitted to Materials Letters)

Yew F. Hor, John F. Federici, Dianhong Luo, Roland A. Levy
“Integrated Mach-Zehnder Interferometer as Chemical Sensor Using Broadband
NIR Source”, (to be submitted to Appl. Optics)

Yew F. Hor, John F. Federici, Dianhong Luo, Roland A. Levy
“Integrated Optical Waveguide Sensors Based On The Principle of Mach-Zehnder
Interferometer”, Second AIMS Materials Research Symposium, NJ, May 2002

D. H. Luo, Y. F. Hor, J. F. Federici, R. A. Levy
“Development of An Integrated Photonics Sensor for Monolithic Hazardous
Organics”, Second AIMS Materials Research Symposium, NJ, May 2002

D. H. Luo, Y. F. Hor, J. F. Federici, R. A. Levy
“Fabrication of An Integrated Photonics Sensor for Hazardous Organics”, Ninth
Annual UNI-TECH Conference, NJ, April 2000

Y. F. Hor, D. Soltys, R. A. Levy, J. F. Federici
“Integrated Mach-Zehnder Interferometer for Chemical Sensing Applications”,
First AIMS Materials Research Symposium, NJ, May 1998

Dedicated to
my beloved husband, *Hee Chuan Lim*,
and to
my parents, brothers and sisters.

ACKNOWLEDGEMENT

I would like to express my gratitude to Dr. John F. Federici, who is my mentor and not only served as my dissertation advisor, providing insightful and intuitive suggestion, but also gave me support and encouragement throughout my tenure here. I would also like to thank Dr. Kenneth R. Farmer of the Microelectronics Research Center for his research grant financial support from Spring 1998 to Fall 2001, and also for serving as one of my Committee member. Special thanks are given to Dr. Pushpendra Singh for helping in the theoretical modeling using FEM in this dissertation; Dr. Nuggehalli Ravindra contributed in numerous helpful and insightful theoretical discussion; and Dr. Haimin Wang for serving on my dissertation Committee. I would also like to thank the following people: Dr. Edip Niver and Dr. Anthony Johnson for their generosity in loaning their top of the line equipment for my research; Dr. Jan Opyrchal and Mr. Herminio Ramirez for his expertise and help in the machine laboratory; Mrs. Renee Crawley and Mrs. Leslie Williams for their generous help; and Dr. Roland Levy for his help in fabricating the Mach-Zehnder waveguide.

I would like to dedicate this achievement in honor of my father, Mr. Hang Pang Hor, and my mother, Madam Ah Yen Lee, who have encouraged and supported me spiritually throughout my education journey. My special gratitude to my husband, who has stood by me with encouragement through all the difficult moments and has helped me overcome some major obstacles in pursuing my Ph. D. degree.

TABLE OF CONTENTS

Chapter	Page
1 INTRODUCTION	1
1.1 Objectives	1
1.2 Waveguide Mode Analysis	2
1.2.1 Approximation Methods	3
1.2.2 Computational/Numerical Methods	5
1.3 Integrated Mach-Zehnder Interferometric Sensor	8
2 WAVEGUIDE DESIGN, TESTING AND FABRICATION	12
2.1 Analogous of the Mach-Zehnder Interferometers	13
2.2 Wave Theory of Optical Waveguides	17
2.3 Analytical Waveguide Design	19
2.3.1 Basic Equations	19
2.3.2 Dispersion Equation for TM Mode	22
2.4 Y-Junctions	25
2.4.1 Tapered Section	26
2.4.2 Splitting Angle	28
2.5 Masks Design	29
2.5.1 Sensor Mask	29
2.5.2 Window Mask	32
2.6 Fabrication By Deposition and Etching	33
2.6.1 LPCVD	34

TABLE OF CONTENTS (Continued)

Chapter	Page
2.6.2 Photolithography	37
2.6.3 Etching	38
2.6.4 Fabrication of the Integrated MZI Sensors	42
2.7 Functionality Testing on Integrated MZI Sensor	45
2.7.1 Wave Guiding Core	45
2.7.2 Y-junction	47
2.7.3 Sensing Area	51
3 COMPUTATIONAL WAVEGUIDE DESIGN WITH FEM	54
3.1 Basic Concept of Wave Theory	55
3.1.1 Time-Harmonic Maxwell's Equation	55
3.1.2 Wave Equation.....	59
3.2 Finite Element Method	61
3.3 One-Dimensional FEM.....	64
3.4 Two-Dimensional FEM	67
3.4.1 Two-Dimensional Basis Functions	68
3.4.2 Two-Dimensional Wave Equations	69
3.4.3 Discretization of The Two-Dimensional Wave Equation.....	751
3.5 Integrated MZI Single Waveguide Mode Solver.....	83
4 INTEGRATED CHEMICAL SENSOR	88
4.1 Multi-Wavelength Experiment	90

TABLE OF CONTENTS (Continued)

Chapter	Page
4.2 Experimental Procedures	92
4.3 Data Acquisition	93
4.4 Power Loss.....	95
5 RESULTS AND DISCUSSION.....	102
5.1 Marcatili's Solution	102
5.2 FEM Solutions	104
5.3 Experimental Results	115
5.3.1 White Light Source.....	115
5.3.2 1.5 μm Broadband Source	124
5.4 Discussion.....	126
5.5 Anticipated Vision	135
5.6 Summary	138
APPENDIX A FABRICATION PROCEDURES FOR THE INTEGRATED MZI	140
APPENDIX B FEM GLOBAL MATRIX ASSEMBLY TABLES.....	143
APPENDIX C ONE-DIMENSIONAL FEM CODE.....	147
APPENDIX D FEM TM AND TE FIELDS FOR AIR	149
APPENDIX E FEM TM MODE FOR DIELECTRIC	157
APPENDIX F FEM TE MODE FOR DIELECTRIC.....	163
APPENDIX G FEM TM MODES CUTOFF	169

TABLE OF CONTENTS (Continued)

Chapter	Page
APPENDIX H FEM TE MODES CUTOFF	181
APPENDIX I WAVEGUIDE PROFILE GENERATION CODE.....	187
APPENDIX J 3D CONTOUR PLOTTING CODE.....	188
APPENDIX K MATHEMATICA PROGRAM FOR MARCATILI'S METHOD	189
BIBLIOGRAPHY.....	190

LIST OF TABLES

Table		Page
3.1	One-dimensional FEM solution with exact analytical solution.....	66
3.2	Cutoff wavenumbers for a rectangular waveguide	81
4.1	Output power splitting ratio (reference arm: sampling arm) for 10 mm and 2 mm length at 1.3 μm , 1.4 μm , and 1.5 μm wavelengths.....	98
4.2	Output power measured from reference arm and sampling arm of different sensors and the Y-junction.....	99
4.4	Total power loss in a straight waveguide with respect to three different wavelengths.....	101

LIST OF FIGURES (Continued)

Figure		Page
1.1	Schematic of an integrated Mach-Zehnder Interferometer pressure sensor.	9
1.2	Schematic of an integrated Mach-Zehnder Interferometer for sensing electric field.	10
2.1	The Mach-Zehnder Interferometer constructed from bulk optics.....	14
2.2	The structure of Integrated Mach-Zehnder Interferometer.....	15
2.3	Side view of the configuration of the Integrated Mach-Zehnder Interferometer shows the exposed sampling arm.....	16
2.4	Two-dimensional rectangular waveguide proposed by Marcatili.....	20
2.5	Mode definitions and electric field distributions in Marcatili's method.....	24
2.6	Schematic of a simple Y-junction.....	26
2.7	(a) A tapered waveguide, and (b) the core cross-section at corresponding positions along (a).....	27
2.8	Schematic of a single sensor mask overlapped with a window mask.....	29
2.9	Sensor mask design with five different arm lengths grouped together.....	30
2.10	Layout of the sensor mask. (Not drawn to scale).....	31
2.11	Window mask with different lengths grouped together.....	32
2.12	Schematic representation of photolithography process.	38
2.13	Isotropic and anisotropic etching profile.	40
2.14	Fabrication processes of the Integrated MZI sensor. (Not drawn to scale) (continued).	43
2.15	Fabrication processes of the Integrated MZI sensor. (continued).....	44
2.16	Experimental setup for the waveguide core testing.	45

LIST OF FIGURES (Continued)

Figure	Page
2.17 PSG is transparent to light with wavelengths of (a) 633 nm and (b) 830 nm.	46
2.18 Experimental setup for the testing of the 3dB splitter.	47
2.19 The output arms profile of a Y-junction before coupling light in.....	48
2.20 Light propagates through the Y-junction.....	49
2.21 Schematic setup to examine the light coherency.	49
2.22 Interference caused by superimposed of two beams output from a symmetry Y- junction.	50
2.23 Window misalignment: (a) off from the sampling arm, and (b) overlapped on both arms.....	52
2.24 Over-etching into the waveguide core of the sampling arm.	53
3.1 Illustration of the differential element ds and the contour C	59
3.2 Triangular element.	67
3.3 Area coordinates of a triangle.	69
3.4 Node coordinates for the e^{th} triangle and illustration of the node-based expansion function $N_i^e(x, y)$	75
3.5 Element geometry for matrix assembly.	79
3.6 Calculated TE_{10} mode fields in a rectangular waveguide.	82
3.7 Calculated TM_{11} mode in a metallic rectangular waveguide.....	84
3.8 Refractive index profile of the MZI single waveguide with each element width of $1.0 \mu\text{m}$	86
3.9 Refractive index profile of the MZI sampling arm (without cladding).	87

LIST OF FIGURES (Continued)

Figure	Page
4.1 Schematic of the experimental setup for the MZI chemical sensor using broadband source.	90
4.2 Spectrum of the Anritsu MG922A white light source.	91
4.3 Spectrum of the JDS Uniphase 1.5 μm broadband source.	92
4.4 Labview program flow-chart for controlling the optical spectrum analyzer.	94
4.5 Experimental setup to measure the output power from both the sampling arm and the reference arm of a Y-junction.	96
4.6 Output results of reference arm and sampling arm with 6 μm core width and 10 mm arm length.	96
4.7 Output results of reference arm and sampling arm with 2 mm arm length.	97
4.8 Output results of straight waveguides with 3.1 cm and 1.4 cm long.	100
5.1 Cutoff values for the three lowest TM modes solved by using the Marcatili's approximation for the 6 μm core waveguide.	104
5.2 Two-dimensional graphic of TM_{11} at 1500 nm wavelength as simulated by FEM with 200 elements for the 6 μm core waveguide.	105
5.3 Two-dimensional graphic of TM_{11} at 1400 nm wavelength as simulated by FEM with 800 elements for the 5 μm core waveguide.	106
5.4 Three-dimensional graphic for TM_{11} mode at 1500 nm wavelength for 6 μm waveguide.	107
5.5 TM_{11} at 1100 nm wavelength for 6 μm waveguide.	107
5.6 Two-dimensional graphic of TM_{21} at 1100 nm wavelength for 6 μm waveguide.	108
5.7 Three-dimensional graphic for TM_{21} mode at 1500 nm wavelength for 6 μm waveguide.	108

LIST OF FIGURES (Continued)

Figure	Page
5.8	TM ₁₁ at 1000 nm wavelength for 6 μ m waveguide..... 109
5.9	Two-dimensional graphic of TM ₂₁ at 1000 nm wavelength for 6 μ m waveguide. 109
5.10	Two-dimensional graphic of TM ₁₂ at 1000 nm wavelength for 6 μ m waveguide. 110
5.11	Three-dimensional graphic for TM ₁₂ mode at 1000 nm wavelength for 6 μ m waveguide..... 110
5.12	Dispersion curves for the lowest four TM modes as determined by FEM for 6 μ m core waveguide. 111
5.13	Dispersion curves for the lowest four TE modes as determined by FEM for 6 μ m core waveguide. 111
5.14	Comparison of the dispersion curves for TM and TE modes in the integrated MZI single waveguide for 6 μ m waveguide..... 112
5.15	Dispersion curves for the lowest four TM modes as determined by FEM for 5 μ m core waveguide. 112
5.16	TM ₁₁ at 1500 nm wavelength as simulated by FEM with 200 elements for the 6 μ m core waveguide without cladding..... 113
5.17	Dispersion curves for the lowest four TM modes as determined by FEM for 6 μ m core waveguide without cladding. 114
5.18	Dispersion curves for the lowest four TM modes as determined by FEM for 6 μ m core sampling arm with 50% of ethanol..... 115
5.19	Comparison among the output profiles of the integrated MZI sensor, the single waveguide and input light profiles. 116
5.20	Experimental results showing the interference spectrums shifted corresponding to the various concentration of ethanol on a 5 μ m MZI waveguide sensor with 8 mm arm length. 117

LIST OF FIGURES (Continued)

Figure		Page
5.21	Experimental results showing the interference spectrums shifted corresponding to the various concentration of ethanol on a 6- μ m MZI waveguide sensor with 8 mm arm length.	118
5.22	Experimental results showing the interference spectrums shifted corresponding to the various concentration of ethanol on a 6 μ m MZI waveguide sensor with 10 mm arm length.	119
5.23	Experimental results showing the interference spectrums shifted corresponding to the various concentration of methanol on a 5 μ m MZI waveguide sensor with 10 mm arm length.	120
5.24	Experimental results of methanol on a 6 μ m MZI waveguide sensor with 8 mm arm length.	120
5.25	Experimental results of methanol on a 6- μ m MZI waveguide sensor with 10 mm arm length.	121
5.26	Comparison between the experimental results of 50% concentration of ethanol and 50% concentration of methanol on a 5 μ m MZI waveguide sensor with 8 mm arm length.	121
5.27	Output spectra of water before and after 50 seconds.	122
5.28	Normalized intensity vs. concentration of methanol based on the experimental data at 1420 nm, 1460 nm, and 1480 nm wavelengths from Figure 5.23.	124
5.29	Experimental results showing the interference spectrums shifted corresponding to the various concentration of methanol on a 5 μ m MZI waveguide sensor with 10 mm arm length using 1.5 μ m broadband source.	125
5.30	Normalized intensity vs. concentration of ethanol based on the experimental data at 1520 nm, 1548 nm, and 1570 nm wavelengths from Figure 5.28.	125
5.31	Schematic of a buried channel waveguide structure.	127
5.32	Schematic of a ridge waveguide structure.	128

LIST OF FIGURES (Continued)

Figure		Page
5.33	Comparison among the output profiles of the integrated MZI sensor, the single waveguide and input light profiles.	129
5.34	Peak wavelength versus refractive index difference of ethanol from water.....	130
5.35	Fringe visibility as a function of wavelength.....	132
5.36	Comparison between the experimental result and theoretical data.....	133
5.37	Schematic of a V-groove for stabilizing the optical fiber.....	134
5.38	A 4 cm long flow cell adhered on top of a sample with two dies of integrated MZI sensors.	135
5.39	Schematic of a Micro-Concentration integrated with MZI.....	136
5.40	Schematic of a multi-channel chemical selectivity device.	137

CHAPTER 1

INTRODUCTION

1.1 Objectives

This study involves the design, fabrication and characterization of an integrated optical waveguide sensor, which will provide a practical means for chemical sensing and monitoring. Though the emphasis of the topic is experimental research and development of the pollutant sensor, the main technical content focuses on the waveguide design and waveguide characterization. The integrated waveguide sensor, specifically an integrated Mach-Zehnder Interferometer sensor was fabricated partially in NJIT's class 10 cleanroom.

The objective of this dissertation is to provide knowledgeable insight on analytical design in addition to computational design of square and rectangular dielectric waveguides, which contribute to the foundation of the integrated Mach-Zehnder Interferometer optical sensor. This is a technically important topic since planar optical waveguides are the key devices to construct integrated optical circuits and semiconductor lasers. Generally, the rectangular waveguides consist of a square or rectangular core surrounded by a cladding with a lower refractive index than that of the core. Mode properties of the light propagation along the longitudinal axis of the waveguide is determined and discussed thoroughly because of its significant dependence on the waveguide design and functionality. Cutoff wavelengths are fundamental design constraints that have traditionally been difficult to calculate. Hence, using computational techniques to solve the problem is one of the major achievements in the design of the

integrated waveguide technology. Here, the proposed computational method for the purpose is the Finite Element Method, and the analytical method used is Marcatili's Approximation.

Experiments are presented to show the performance ability of the sensor using different light sources and various chemical concentrations. The relation of the intensity to the change in wavelengths and concentrations are reported. Future implementation can be achieved to demonstrate chemical species selectivity based on the output intensity variation of the sensor or absorption due to a chemical at certain wavelengths, which is also known as the *fingerprint* of that chemical.

Essentially, this dissertation comprises of two major parts:

1. Fabrication and testing of the integrated Mach-Zehnder Interferometer sensors, and
2. Numerical simulations using the finite element method.

1.2 Waveguide Mode Analysis

Several methods of the analytical and computational design analysis of the waveguides are discussed briefly below for comparison and illustrative purposes. The advantages as well as the shortcomings of each method are also discussed so that prospect selection of the analysis can be chosen wisely. Although the analytical methods are approximate methods, which predicted spurious modes at cutoff, the essential light wave transmission mechanism in the waveguides can be fully investigated. Some of the methods are only capable of approximating the solution for step-index profile and simple waveguide geometry, namely, the planar optical waveguides. Complicated cross-sectional

waveguide geometries such as rib waveguides can be treated precisely by computational methods. However, computational methods have drawback of complexity in programming, and require considerably large memory and hard disk space to compensate for the running time.

1.2.1 Approximation Methods

Marcatili's Approximation

A famous approximation method for solving the scalar wave equation of the form

$$\nabla_t^2 H_z + (k^2 - \beta^2) H_z = 0$$

for the rectangular or square cross-sections with a step index profile is due to Macatili¹. The accuracy of this method improves with the increasing values of the normalized frequency but it provides reasonable estimates for the range of the normalized frequencies in the practical single-mode region. This method is appropriate for solving a square or rectangular waveguides with symmetrical cross-section such as an embedded waveguides or buried channel waveguides. This approximation will be discussed in detail in Chapter 2 since it is the method used for the mode analysis of the Mach-Zehnder waveguides design for the project. The Marcatili's method predicts a *spurious* cutoff wavelength for the fundamental mode at low frequency. Furthermore, it has the deficiency for determining the modal fields, especially near the corners of the core-cladding interface.

Effective Index Method

The ridge waveguide is difficult to analyze by the Marcatili's method since the waveguide structure is complicated to deal with by the division of waveguide. In order to

analyze ridge waveguide, one should use numerical methods; such as finite element method and the finite difference method. The effective index method² is an analytical method applicable to complicated waveguides such as ridge waveguides and diffused waveguides in LiNbO₃. The accuracy of the effective index method is almost the same as that of Marcatili's method; but effective index method gives a larger estimation than the accuracy solution, whereas Marcatili's method gives a lower estimation than the accurate solution, respectively. The effective index method avoids the spurious cutoff problem of the Marcatili's approach, but suffers from the same deficiency for determining the modal fields.

Gaussian Approximation

Gaussian Approximation is another form of approximation that using the theory of variational methods.^{3,4,5} In this approach, a relatively simple functional dependence is assumed as a trial function for the spatial variation of the fundamental mode. The fundamental mode field of the weakly guiding waveguide has an approximately parabolic variation within the core, and an exponentially decreasing form in the uniform cladding. This suggests that a Gaussian function is a close approximation to the exact solution over both regions, since it is approximately parabolic close to the waveguide axis. The basis of the Gaussian Approximation is to obtain an equation for the optimal spot size of the Gaussian function by requiring the solution to be stationary. One of the disadvantages of this Gaussian Approximation, like the Marcatili's approximation, is the prediction of a spurious cutoff of the fundamental mode of the square waveguide.

1.2.2 Computational/Numerical Methods

Point-Matching Method

The basic idea of the Point-Matching Method⁶ is that, for regions of constant refractive index, there are discrete, separable solutions of the scalar wave equation in cylindrical polar coordinates based on the central axis of the waveguide as the origin in the cross section. Each solution is the product of a Bessel function (giving the radial dependence) and trigonometric function (giving the azimuthally dependence). The general solution in each region consists of the sum over the basic set of these products. For computational purposes, two limited expansions are used: one for the core and one for the cladding. These two expressions and their first derivatives are matched at N points on the core-cladding interface and a system of linear equations is derived for the expansion coefficients and propagation constants; this is solved using standard numerical techniques. The disadvantages of the point matching method are the limitation to the step-profile waveguides only, and a very large number of coefficients are required in the expansions close to cutoff.

Harmonic Boundary Method

The Harmonic Boundary Method² is based on an expansion of the field in terms of a Fourier-Bessel series in the core and cladding. This method is similar to the Point Matching Method used by Goell⁶ except the procedure used to transform the solutions of the scalar wave equation into a set of coupled linear equations. The Point Matching Method used point matching of the field on the boundary for evaluation of the mode field while the Harmonic Boundary Method expanded the field into a Fourier series and a set of linear equations for the coefficients of the decomposition is generated, by matching the

core and the cladding fields. This method also has the advantage of being able to determine the modal field at cutoff by replacing the Fourier-Bessel expansion over the cladding by cylindrical harmonics, i.e. solutions of the Laplace equation in cylindrical polar coordinates. The major drawback of this method is that, like the Point Matching Method, it is restricted to step-index profile waveguiding structures.

Beam Propagation Method (BPM)

This method⁷ solves the scalar wave equation by incremental propagation along the length of a waveguide. It can deal with graded index profile and arbitrary cross-sectional geometries. BPM was originally derived for longitudinally dependent variations, such as Y-junctions, but is highly inefficient for translationally invariant waveguides. This drawback is a consequence of the basic algorithm being based on the full three-dimensional scalar wave equation, rather than the separable two-dimensional equation for the transverse modal dependence. Numerous improved forms have been developed to increase the accuracy, such as Finite-Difference Beam Propagation Method (FDBPM)⁸, Finite-Integration Beam Propagation Method (FIBPM)⁹ and Finite-Element Beam Propagation Method (FEBPM)¹⁰ to specifically solve a variety of waveguide and device propagation problems.

Fourier Decomposition Method and Modified Fourier Decomposition Method (MFDM)

This Fourier Decomposition Method¹¹ is based on a decomposition of the modal field into complete set of sinusoidal basis functions, and can be readily applied to the square or rectangular waveguides. In other words, it uses the orthogonality of trigonometric functions to reduce the scalar wave equation to a system of linear equations. An attraction of this algorithm is the subdivision of the domain into rectangular regions where the

integration, related to scalar products of trigonometric functions can be performed analytically. This method has several advantages over other numerical approaches, namely, it is easy to implement because it relies on well-known Fourier analysis, and it gives the modal fields of the waveguides in terms on a single expansion defined on the whole domain which simplifies the programming task. However, it has the drawback of becoming less and less accurate as a mode approaches its cutoff wavelength, i.e. this method can only be used to calculate modal field distributions that are reasonably well confined to the core region. As the cutoff is approached, the modal fields spread farther into the cladding and the implicit assumption of zero fields at the boundary requires a prohibitively large bounding box.

A modified method from the original version avoids this limitation by mapping the infinite cross-sectional x-y plane of the waveguide into a finite domain, and then applying the Fourier Decomposition. This method, labeled as Modified Fourier Decomposition Method (MFDM),¹² leads to accurate values of cutoff wavelength for most waveguiding structures.

Finite Difference Method (FDM)

The Finite Difference Method^{13,14,15} is the oldest known method for solving partial differential equations with boundary conditions, and has been used with success in the analysis of non-homogeneous waveguides, because it subdivides the domain into many subregions, where the partial differential equation is replaced by finite difference equation. The system of linear equations obtained is simpler than those obtained by the Finite Element Method (FEM), and the solution is free from numerical artifact (the so-called spurious modes) that is observed when using FEM.

Finite Element Method (FEM)

The Finite Element Method has been very successful in the numerical solution of the partial differential equations because of its ability to model the most intricate domain geometries.¹⁶ It extends the concept of the Finite Difference Method subdivision of the domain to arbitrary element shapes on which the basic shape functions are defined. The advantage of the FEM is that it can determine modal parameters accurately close to cutoff.^{17,18,19} Another important advantage is the ability to treat geometrically complex structures and it can be applied to material with non-constant properties.

1.3 Integrated Mach-Zehnder Interferometric Sensor

Optical sensors exhibit interesting properties for sensing chemical species and their concentration. The most significant advantages of optical sensors are: immunity to electromagnetic interference, noninteractivity with the sensor environment, and high sensitivity when using optics fundamentals such as interferometry.²⁰

Silicon-based integrated optics technology is a really attractive way for the development of optical sensors.²¹ It has a lot of advantageous characteristics such as: advanced processing technology associated with the substrate and the materials used for the optical waveguides, the possibility of obtaining efficient coupling between optical fibers and waveguides, and the possible association of optical and electrical circuits on the same chip.

Several integrated optical sensors based on the Mach-Zehnder interferometer and using different technologies have been reported. For example, Vadekar et al.²² have presented a novel pressure sensor designed using the concept of the integrated silicon

Mach-Zehnder Interferometer. The integrated MZI waveguides are of the ARROW type, which is the antiresonant reflecting optical waveguide, instead of the classic total internal reflection waveguide. The main feature of the ARROW is that it allows for low index core waveguide on a high index substrate without thick isolation layer. Another feature is its high polarization selectivity. The pressure measurement mechanism is achieved by having the sampling arm of the interferometer fabricated on a thin silicon diaphragm, as depicted in Figure 1.1. When an applied pressure deflects the diaphragm, it will cause a change in the optical path length, and hence changing the phase shift with respect to the reference arm.

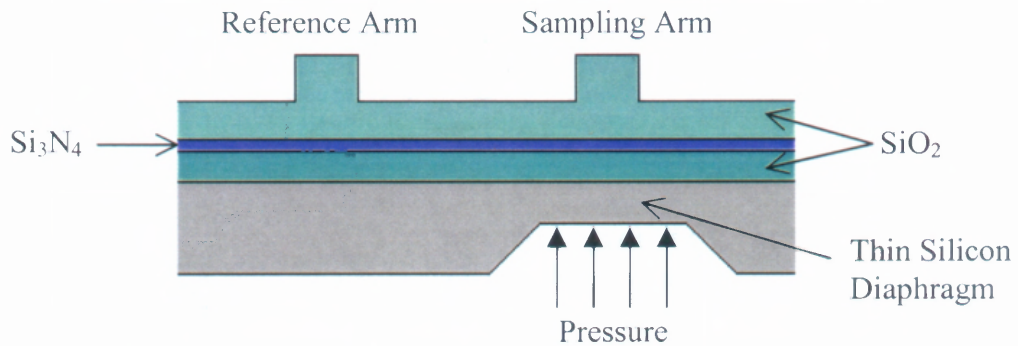


Figure 1.1 Schematic of an integrated Mach-Zehnder Interferometer pressure sensor.

Naghski et al.²³ reported another innovative configuration for the integrated Mach-Zehnder Interferometric electric field sensor device utilizing the electro-optics effect for sensing electric fields, as illustrated in Figure 1.2. In his study, lithium niobate is used as the waveguides material instead of silicon, and the sensing mechanism using a reversed-poled crystal orientation region. The device operates by immersion in an electric

field, and the reverse poling of the sensing arm of the interferometer provides opposing optical phase changes in the two interferometer arms.

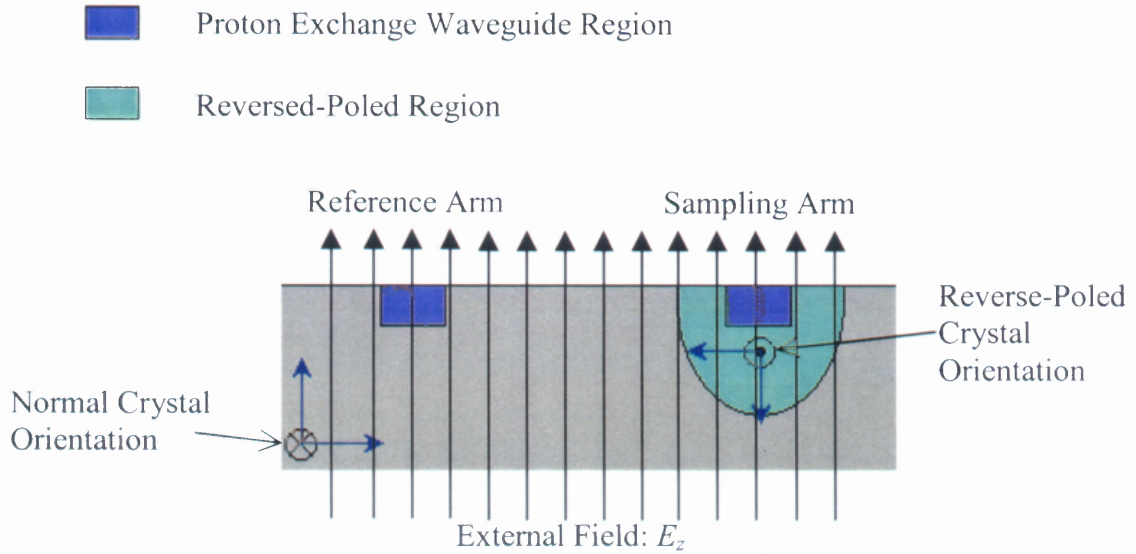


Figure 1.2 Schematic of an integrated Mach-Zehnder Interferometer for sensing electric field.

Another typical application using the integrated Mach-Zehnder Interferometer is the immunosensor,^{24,25} which uses the evanescent field to detect small refractive changes at the sampling arm. The key idea is to have an antibody receptor surface on the sampling arm to directly detect the binding of the antigen to the receptor surface. Similar ideology is found in the biosensor, the humidity sensor, and the refractometer.^{26,27,28}

This project suggests an integrated symmetry Mach-Zehnder Interferometer to serve as the basis for chemical sensing application. Kherrat et al.²⁹ have reported a chemical sensor based on the integrated planar waveguide designed as a Mach-Zehnder interferometer with taper end instead of a Y-junction. The change in the refractive index

due to the absorption of the organic molecules at the sensing arm causes phase shift at the interferometer, which is proportional to the change in chemical concentration.

Most of the experimental techniques using integrated MZI sensor for sensing purposes involved only the single wavelength source. The limitation of using single wavelength source is that, it confines the application of the sensor only to single analyte detection. In this dissertation, a new idea is presented by using multi-wavelength source³⁰ as the input light source instead of the single wavelength source. The choice of multi-wavelength source leads to the possibility of multiple chemicals concentration detection, as different chemical species exhibits its own characteristic fingerprint.

CHAPTER 2

WAVEGUIDE DESIGN, TESTING AND FABRICATION

Prior to fabrication, design parameters of the waveguide need to be determined and optimized. The waveguide parameters such as waveguide dimension and the refractive index of the core and the cladding are obtained from the single-mode cutoff frequency calculated using either the analytical or the numerical methods. In this section, the details of analytical calculation to determine the cutoff in terms of the waveguide parameters will be presented. The method discussed here is Marcatili's approximation since it is the easiest among the other analytical techniques. The purpose is to solve the scalar wave equation derived from Maxwell's equations because it describes the mode properties inside the waveguides.

The wave equation is the key to understand the electromagnetic field propagation inside a dielectric waveguide. The solution to this eigen value problem displays the properties of the mode propagation (i.e. the eigenvalue) and the field distribution (i.e. the eigen function), provided that the boundary conditions are satisfied. The solution can be solved analytically using Marcatili's approximation together with the waveguide parameters for the TM or TE modes. The cutoff condition for the single mode propagation, which is determined from the eigenvalue, provides the basic idea of the single mode waveguide design. However, the solution is not exact as discussed in Chapter 1. The exact solution and field distribution can be fully studied by Finite Element Method as discussed in Chapter 3.

Fabrication of the Integrated Mach-Zehnder Interferometer sensor involves several important standard processes like Chemical Vapor Deposition (CVD) for thin film fabrication, photolithography for mask transfer, and etching for rib waveguide formation. The detailed fabrication procedures of the tested Mach-Zehnder Interferometer sensors are discussed. After completion of the sensor fabrication processes, the functionality testing experiments were carried out for the thin film of SiO_2 and PSG, the waveguides and the Y-junction separately.

Before going through the details of analytical design of the rectangular waveguides, the structure of the Mazh-Zehnder Interferometer (MZI) is discussed with the comparison between the bulk optics setup of MZI and the integrated optical waveguide MZI. The important part of the interferometer structure is the *sensing area*, where the sensing mechanism takes part, which contributes to the functionality as a sensor.

2.1 Analogous of the Mach-Zehnder Interferometers

The construction and structure of the interferometer as well as the operating function involving light source and phase shift device is described in this section. The analogous between the bulk optics and integrated optics gives the basic concept of the evolution of the novel integrated Mach-Zehnder Interferometer Sensor.

The Mach-Zehnder Interferometer is basically used to measure variations of refractive index, and hence of density, in compressible gas flows. The arrangement of the Mach-Zehnder Interferometer using lenses, beam-splitters, and mirrors, is shown in Figure 2.1. Light from a source S in the focal plane of a well-corrected lens L_1 is divided at the semireflecting surface A_1 of a plane-parallel glass plate D_1 into two beams, which,

after reflection at plane mirrors M_1 , M_2 , are recombined at the semireflecting surface A_2 of a second identical plane-parallel plate D_2 , and emerge to a well-corrected collecting lens L_2 . The four reflecting surfaces are usually arranged to be approximately parallel, with their centers at the corners of a parallelogram. Suppose the source is a point source of quasi-monochromatic light. Let W_1 be a plane wave-front in the beam between M_2 and D_2 , W_2 the corresponding plane wave-front in the beam between M_2 and D_2 , W_1' the virtual plane wave-front between M_2 and D_2 which would emerge from D_2 coincident and cophasal with W_1 . At a point P on W_2 , the virtual phase difference between the emergent beams is then

$$\delta = \frac{2\pi}{\lambda_o} nh \quad (2.1)$$

where $h = PN$ is the normal distance from P to W_1' , λ_o is the wavelength of the light source, and n is the refractive index of the medium between W_2 and W_1' .

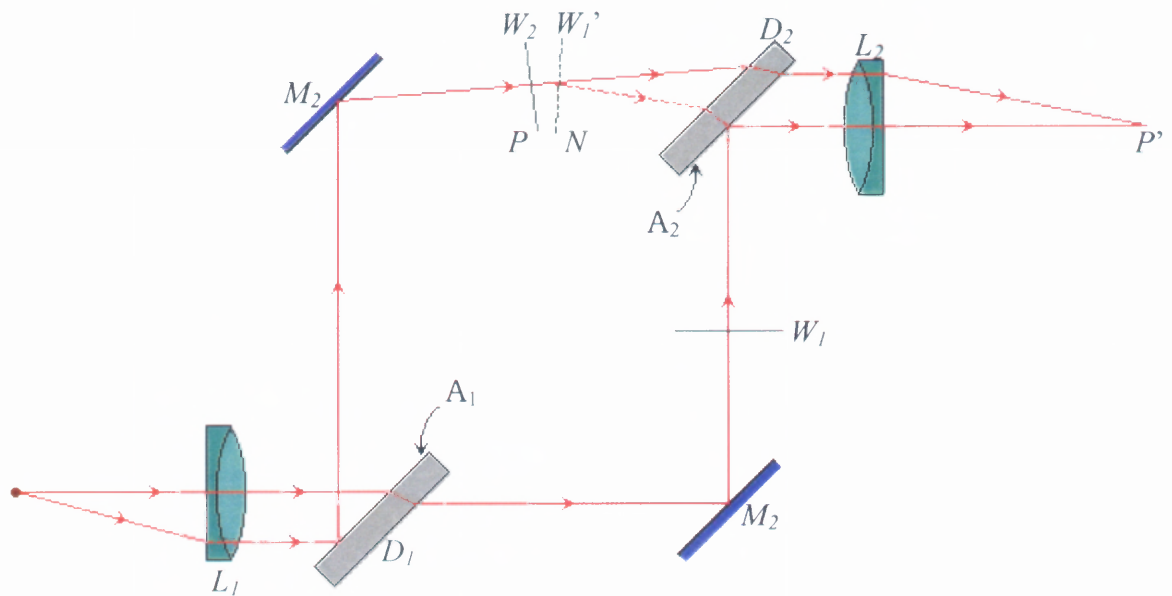


Figure 2.1 The Mach-Zehnder Interferometer constructed from bulk optics.

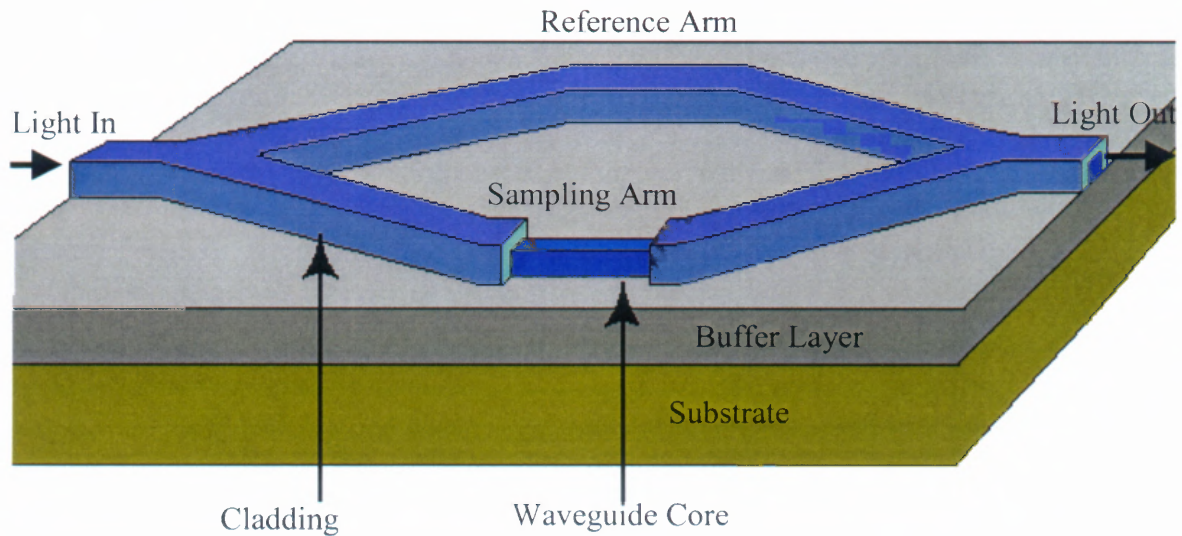


Figure 2.2 The structure of Integrated Mach-Zehnder Interferometer.

The integrated Mach-Zehnder interferometer is constructed from two planar single-mode waveguides connected by two 3 dB Y-splitters at both ends as illustrated in Figure 2.2. The sampling arm of the interferometer is exposed directly to the chemical species, while a protective oxide buffer layer covers the reference arm from the influence of the liquid as shown in Figure 2.3. Laser light is coupled into the waveguide and split into the reference and sampling arms by the Y-splitter configuration. The presence of the analyte in proximity of the sampling waveguide causes an effective index change within the sampling waveguide arm. Therefore, a phase difference, $\Delta\phi$, exists between the two arms. When light from the two interferometer-arms recombines, constructive or destructive interference occurs and the light intensity exiting the interferometer, I_x , ratio to the input light I_o , is given by:

$$\frac{I_x}{I_o} = \frac{1}{2}(1 + \cos \delta) \quad (2.2)$$

$$\delta = \frac{2\pi}{\lambda_o}(L_2 n_2 - L_1 n_1) \quad (2.3)$$

where L is the length of the waveguide arms, λ_o is the wavelength of the incident light and n is the refractive indices with the subscripts refer to sampling arm and reference arm respectively. If the two arms of the interferometer are the same length ($L_1=L_2=L$), then equation (2.2) becomes

$$\frac{I_x}{I_o} = \frac{1}{2} \left[1 + \cos \frac{2\pi L}{\lambda_o} (n_2 - n_1) \right] \quad (2.4)$$

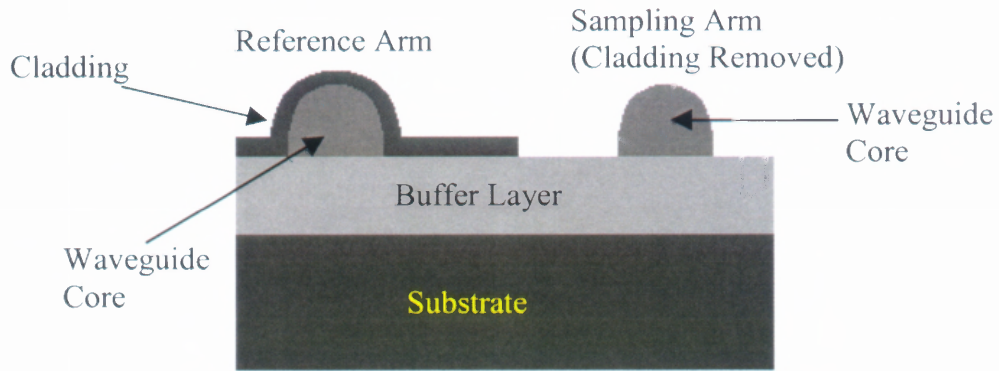


Figure 2.3 Side view of the configuration of the Integrated Mach-Zehnder Interferometer shows the exposed sampling arm.

2.2 Wave Theory of Optical Waveguides

Optical waveguide analysis requires the explicit understanding of the electrodynamics of the propagation waves, i.e. the electromagnetic field. The spatial dependence of the electric field $\tilde{\mathbf{E}}(x, y, z)$ and the magnetic field $\tilde{\mathbf{H}}(x, y, z)$ of the optical waveguide is determined by Maxwell's equations, and have the following forms for source-free, dielectric media³¹

$$\nabla \times \tilde{\mathbf{E}} = -\mu_o \frac{\partial \tilde{\mathbf{H}}}{\partial t} \quad (2.5)$$

$$\nabla \cdot \tilde{\mathbf{E}} = 0 \quad (2.6)$$

$$\nabla \times \tilde{\mathbf{H}} = \epsilon_o n^2 \frac{\partial \tilde{\mathbf{E}}}{\partial t} \quad (2.7)$$

$$\nabla \cdot \tilde{\mathbf{H}} = 0 \quad (2.8)$$

where ϵ_o and μ_o are the free space dielectric constant and permeability respectively, and n is the refractive index profile.

The refractive index profile resulting from the fabrication process determines the propagation along the waveguides. For simplicity, we assume that the waveguides are isotropic and non-absorbing, so the profile $n(x, y, z)$ is a real scalar function. Since the waveguides are translationally invariant, the index profile does not change along the z -axis, so the profile has only transverse dependence, i.e. $n = n(x, y)$.

The independence of the refractive index on the longitudinal coordinates allows the electric field \mathbf{E} and the magnetic field \mathbf{H} vectors to be written in the separable forms

$$\tilde{\mathbf{E}}(x, y, z) = \mathbf{E}(x, y) \exp(-j\beta z) \exp(j\omega t) \quad (2.9)$$

$$\tilde{\mathbf{H}}(x, y, z) = \mathbf{H}(x, y) \exp(-j\beta z) \exp(j\omega t) \quad (2.10)$$

where the \mathbf{E} and \mathbf{H} are the vectors contain the transverse dependence of the electric and magnetic fields. The term βz denotes the phase change at distance z along the waveguide in terms of propagation constant β while the term $-i\omega t$ denotes the time dependence of the phase in term of the source frequency ω and time t .

It is convenient to decompose the $\tilde{\mathbf{E}}$ and $\tilde{\mathbf{H}}$ fields into longitudinal components, parallel to the waveguide axis, denoted by the scalar quantities $\mathbf{E}_z(x, y)$ and $\mathbf{H}_z(x, y)$ respectively; and transverse components, orthogonal to the waveguide axis, denoted by $\mathbf{E}_\perp(x, y)$ and $\mathbf{H}_\perp(x, y)$ respectively, where

$$\mathbf{E}(x, y) = \mathbf{E}_\perp(x, y) + \mathbf{E}_z(x, y)\hat{\mathbf{z}} \quad (2.11)$$

$$\mathbf{H}(x, y) = \mathbf{H}_\perp(x, y) + \mathbf{H}_z(x, y)\hat{\mathbf{z}} \quad (2.12)$$

and $\hat{\mathbf{z}}$ is the unit vector parallel to the z axis.

There are certain discrete electromagnetic resonances in the cross-section, corresponding to *bound modes* of the waveguide. Each bound mode has its own propagation constant β , which is the solutions of the eigenvalue equation, and the associated electric and magnetic field distribution. The flow of the electromagnetic power in a mode is always parallel to the waveguide axis. A *single-mode* waveguide can only support one bound mode, which is known as fundamental mode. Single-mode waveguide is of primarily concern because of the broad application as described in Chapter 1. The parameter values and the source wavelength are the key values for determination of the single-mode waveguide.

The range of values that the propagation constant β of any bound mode can take is related to the refractive indices of the waveguide, that is

$$kn_{clad} \leq \beta \leq kn_{core} \quad (2.13)$$

where $k = 2\pi/\lambda$ is the wavenumber, n_{clad} is the cladding refractive index, n_{core} is the core refractive index, and λ is the source wavelength. The cutoff of a mode corresponds to the smallest permissible value of the propagation constant, that is $\beta = kn_{clad}$. Below this value, the mode is no longer guided. In general, the cutoff wavelength of the second mode is used to determine the largest wavelength below which the waveguide is single-mode

2.3 Analytical Waveguide Design

There are very few exact analytical solutions to waveguides analysis because of the complexity of the Maxwell's equations, or equivalently the vector wave equations, due to the coupling of the three scalar components of both the electric and magnetic fields vectors. Conveniently, most silica-based waveguides have only a small difference of refractive index change over their cross section. Thus, it is sufficient to use a scalar analysis, which considerably simplifies the analysis because scalar wave equation involves only one component of the electric fields.

2.3.1 Basic Equations

In this section, the analytical method, proposed by Marcatili,¹ to deal with the two-dimensional optical waveguide, as shown in Figure 2.4, is described. The important assumption of this method is that the electromagnetic field in the shaded area in Figure 2.4 can be neglected, since the electromagnetic field of the well-guided mode decays

quite rapidly in the cladding region. Then the boundary conditions for the electromagnetic field are not imposed in the shaded area.

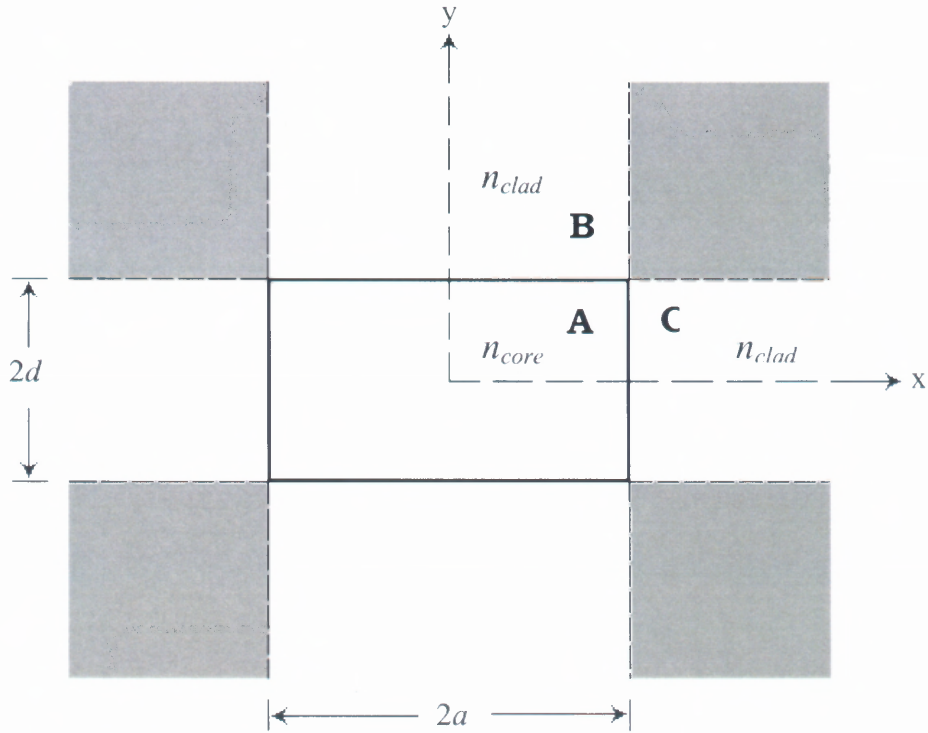


Figure 2.4 Two-dimensional rectangular waveguide proposed by Marcatili.

A set of equations for the electromagnetic field components is first obtained by substituting equations (2.9) and (2.10) into equations (2.5) and (2.7):

$$\frac{\partial E_z}{\partial y} + j\beta E_y = -j\omega\mu_o H_x \quad (2.14)$$

$$-j\beta E_x - \frac{\partial E_z}{\partial x} = -j\omega\mu_o H_y \quad (2.15)$$

$$\frac{\partial E_y}{\partial x} - \frac{\partial E_x}{\partial y} = -j\omega\mu_o H_z \quad (2.16)$$

$$\frac{\partial H_z}{\partial y} + j\beta H_y = j\omega\epsilon_o n^2 E_x \quad (2.17)$$

$$-j\beta H_x - \frac{\partial H_z}{\partial x} = j\omega\epsilon_o n^2 E_y \quad (2.18)$$

$$\frac{\partial H_y}{\partial x} - \frac{\partial H_x}{\partial y} = j\omega\epsilon_o n^2 E_z \quad (2.19)$$

First, consider the electromagnetic mode in which the E_x and H_y are predominant. According to Marcatili's treatment, H_x is set to zero in equations (2.14) – (2.19). Then the wave equation and the electromagnetic field representation are obtained as

$$\frac{\partial^2 H_y}{\partial x^2} + \frac{\partial^2 H_y}{\partial y^2} + (k^2 n^2 - \beta^2) H_y = 0 \quad (2.20)$$

$$H_x = 0 \quad (2.21)$$

$$E_x = \frac{\omega\mu_o}{\beta} H_y + \frac{1}{\omega\epsilon_o n^2 \beta} \frac{\partial^2 H_y}{\partial x^2} \quad (2.22)$$

$$E_y = \frac{1}{\omega\epsilon_o n^2 \beta} \frac{\partial^2 H_y}{\partial x \partial y} \quad (2.23)$$

$$E_z = -\frac{j}{\omega\epsilon_o n^2} \frac{\partial H_y}{\partial x} \quad (2.24)$$

$$H_z = -\frac{j}{\beta} \frac{\partial H_y}{\partial y} \quad (2.25)$$

On the other hand, H_y is set to zero in equations (2.14) – (2.19) to consider the electromagnetic field in which E_y and H_x are predominant. The wave equation and the electromagnetic field representation are given by

$$\frac{\partial^2 H_x}{\partial x^2} + \frac{\partial^2 H_x}{\partial y^2} + (k^2 n^2 - \beta^2) H_x = 0 \quad (2.26)$$

$$H_y = 0 \quad (2.27)$$

$$E_x = -\frac{1}{\omega\epsilon_o n^2 \beta} \frac{\partial^2 H_x}{\partial x \partial y} \quad (2.28)$$

$$E_y = -\frac{\omega\mu_o}{\beta} H_x - \frac{1}{\omega\epsilon_o n^2 \beta} \frac{\partial^2 H_x}{\partial y^2} \quad (2.29)$$

$$E_z = \frac{j}{\omega\epsilon_o n^2} \frac{\partial H_x}{\partial y} \quad (2.30)$$

$$H_z = -\frac{j}{\beta} \frac{\partial H_x}{\partial x} \quad (2.31)$$

The modes in equations (2.20) – (2.25) are described as E_{pq}^x (p and q are integers), since E_x and H_y are the dominant electromagnetic fields. Conversely, the modes in equations (2.26) – (2.31) are called E_{pq}^y , since E_y and H_x are the dominant electromagnetic fields. In the following section, the solution method of the dispersion equation for the E_{pq}^x mode is described in detail.

2.3.2 Dispersion Equation for TM Mode

Since the rectangular waveguide shown in Figure 2.4 is symmetrical with respect to the x- and y- axis, only regions A, B, and C are analyzed. The solution fields that satisfy the wave equation (2.20) is expressed as

$$A = \begin{cases} A \cos(k_x x - \phi) \cos(k_y y - \psi) & \text{region A} \\ A \cos(k_x a - \phi) e^{-\gamma_x(x-a)} \cos(k_y y - \psi) & \text{region B} \\ A \cos(k_x x - \phi) e^{-\gamma_y(y-d)} \cos(k_y d - \psi) & \text{region C} \end{cases} \quad (2.32)$$

where the transverse wavenumbers k_x , k_y , γ_x , and γ_y and the optical phases ϕ and ψ are given by

$$\begin{cases} -k_x^2 - k_y^2 + k^2 n_{core}^2 - \beta^2 = 0 & \text{region } \mathcal{A} \\ \gamma_x^2 - k_y^2 + k^2 n_{clad}^2 - \beta^2 = 0 & \text{region } \mathcal{B} \\ -k_x^2 + \gamma_y^2 + k^2 n_{clad}^2 - \beta^2 = 0 & \text{region } \mathcal{C} \end{cases} \quad (2.33)$$

and

$$\begin{cases} \phi = (p-1)\frac{\pi}{2} & (p=1, 2, \dots) \\ \psi = (q-1)\frac{\pi}{2} & (q=1, 2, \dots) \end{cases} \quad (2.34)$$

Note that the p and q starts from one because it follows from the mode definition by Marcatili. By the conventional mode definition, the lowest mode in the rectangular waveguides is $E_{p=1,q=1}^x$ or $E_{p=1,q=1}^y$ mode as illustrated in Figure 2.5, which has only one electric field peak along both the x-and y-axis directions. Therefore, in the mode definition by Marcatili, integers p and q represent the number of local electric field peaks along the x- and y-axis directions. The boundary conditions such that the electric field $E_z \propto \left(1/n^2\right) \frac{\partial H_y}{\partial x}$ should be continuous at $x = a$ and the magnetic field $H_z \propto \frac{\partial H_y}{\partial y}$ should be continuous at $y = d$, are applied to the wave equation to obtain the following dispersion equations:

$$k_x a = (p-1)\frac{\pi}{2} + \tan^{-1}\left(\frac{n_{core}^2 \gamma_x}{n_{clad}^2 k_x}\right) \quad (2.35)$$

$$k_y d = (q-1)\frac{\pi}{2} + \tan^{-1}\left(\frac{\gamma_y}{k_y}\right) \quad (2.36)$$

Transverse wavenumbers k_x , k_y , γ_x , and γ_y are related, by equation (2.33), as

$$\gamma_x^2 = k^2(n_{core}^2 - n_{clad}^2) - k_x^2 \quad (2.37)$$

$$\gamma_y^2 = k^2(n_{core}^2 - n_{clad}^2) - k_y^2 \quad (2.38)$$

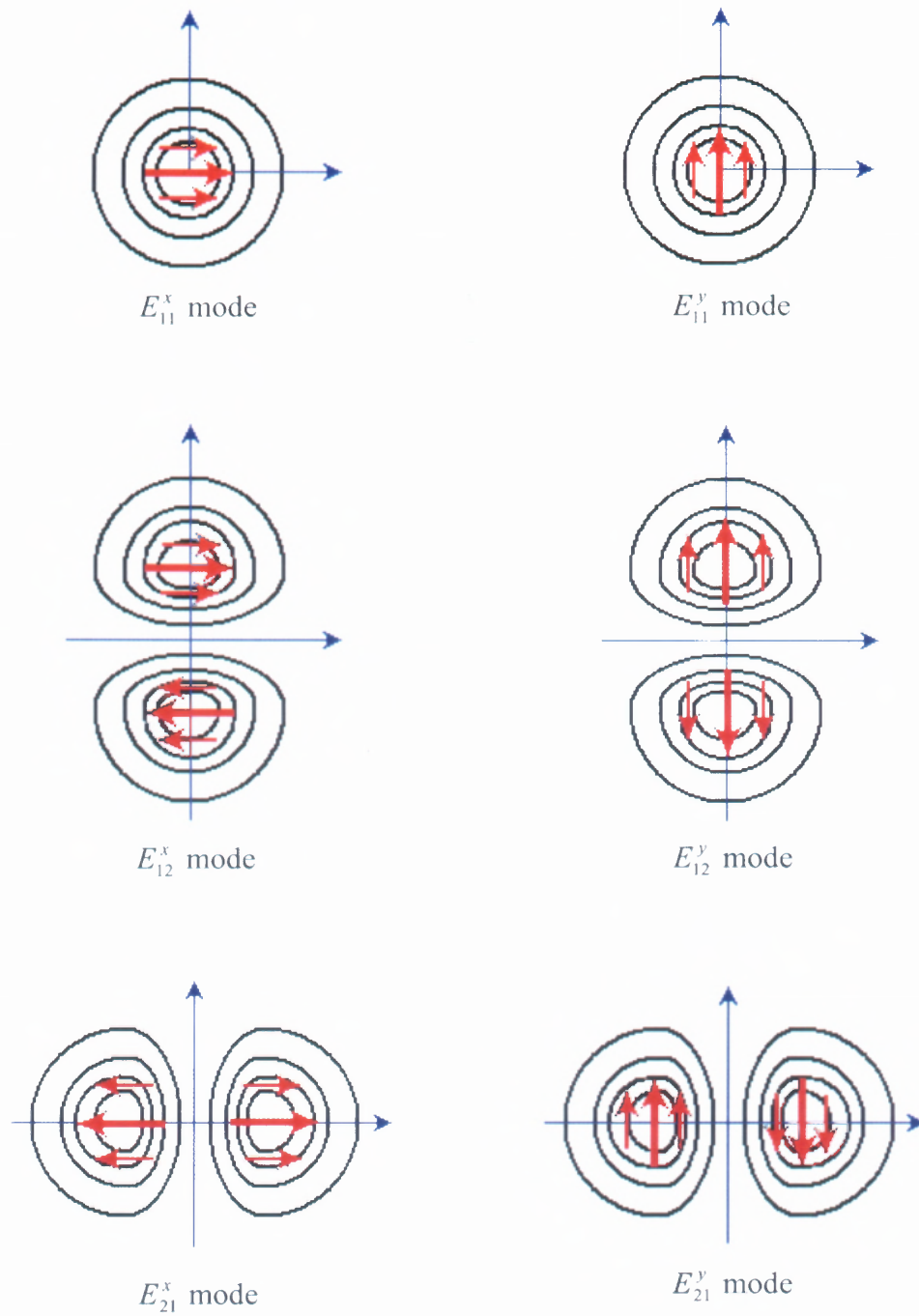


Figure 2.5 Mode definitions and electric field distributions in Marcatali's method.

k_x is acquired from equations (2.35) and (2.37), while k_y is obtained from equations (2.36) and (2.38), respectively. The propagation constant β is then determined from

$$\beta^2 = k^2 n_{core}^2 - (k_x^2 + k_y^2) \quad (2.39)$$

2.4 Y-Junctions

An important passive device in the planar optical technology is the single-mode symmetric Y-junction, illustrated schematically in Figure 2.6. The Y-junction is the most critical feature of the sensor design since it has the smallest dimensions near the splitting part of the Y where the angle section approaches the 2 μm limit of the NJIT's exposure tool in the photolithography process. The functionality of the Y-junction depends exclusively on its symmetry. If the fundamental mode is excited in the stem, it will split equally between the two arms and, even allowing excess loss, the optical power exiting the two arms will be equal. In other words, the device is technically a 3 dB splitter. Moreover, since the splitting action depends only on symmetry, it is independent of wavelength. Thus the Y-junction is a 3 dB wavelength-independent splitter. When the Y-junction is operated in the reverse direction, the fundamental mode of either arm propagates through the junction to become the fundamental mode of the stem, but with a 50% loss of power. The 50%, or 3dB loss is also independent of wavelength, and is a consequence of the reciprocity property of the Y-junction.

The emphasis in this section is on the design of an optimally low-loss Y-junction, using simple physical principles, and constrained by the limitations imposed by the lithographical and fabrication processes. In the following sections, the analyses of the

tapered and splitting sections are presented in order to develop a complete low-loss Y-junction design.

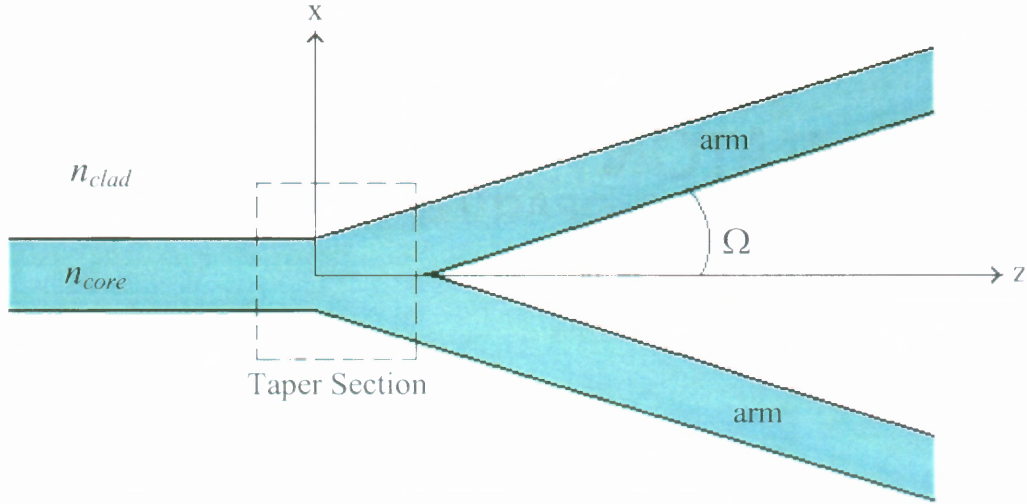


Figure 2.6 Schematic of a simple Y-junction.

2.4.1 Tapered Section

Changing the cross-section of a single-mode waveguide by tapering necessarily induces radiation loss from the fundamental mode, because of the loss of translationally invariance. Fundamentally, loss can be kept arbitrarily small by making the taper angle sufficiently small, but such devices are difficult to fabricate and impractically long. Hence, optimal taper shape, which minimizes the length for a given overall loss,^{32,33} is discussed below to aid the design.

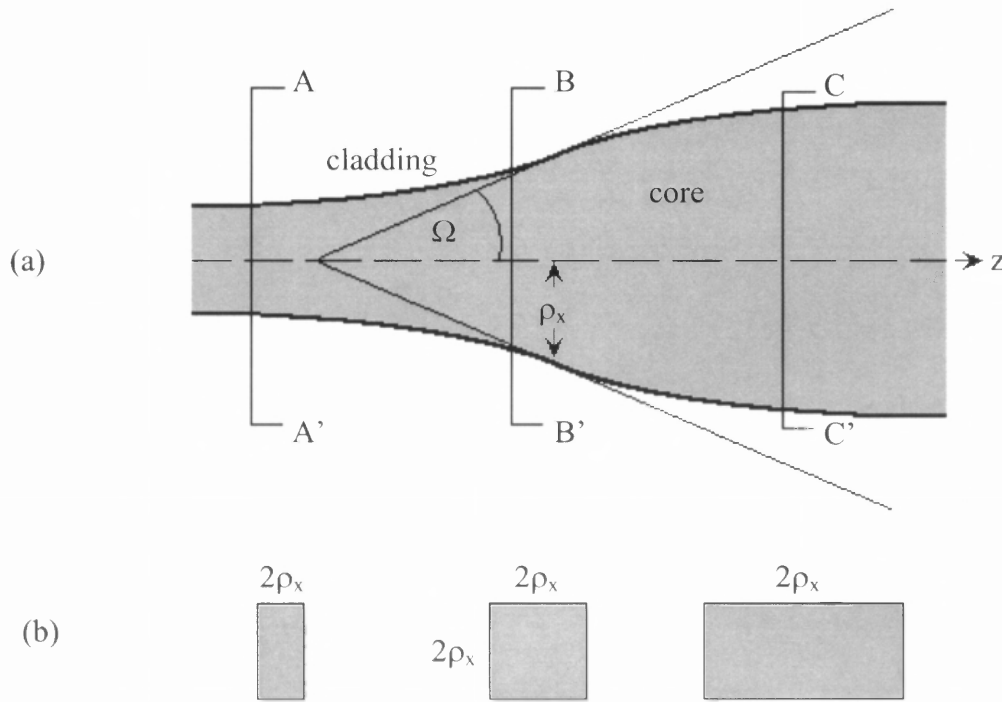


Figure 2.7 (a) A tapered waveguide, and (b) the core cross-section at corresponding positions along (a).

A tapering section of a square or rectangular waveguide has a constant height in the vertical plane, while the horizontal width varies throughout the waveguide axis. Figure 2.7 shows such a tapered mask design with the cross-section BB' corresponds to a square-core cross-section with side $2\rho_x=2\rho_y$; CC' to a down-tapered cross-section with width $2\rho_x<2\rho_y$; and AA' to an up-tapered cross-section with width $2\rho_x>2\rho_y$.

Assume the waveguide parameter is defined as

$$V = k(\rho_x \rho_y)^{1/2} (n_{co}^2 - n_{cl}^2)^{1/2} = k(\rho_x \rho_y)^{1/2} n_{co} (2\Delta)^{1/2} \quad (2.40)$$

where Δ is the relative index difference defined as $\Delta = \frac{n_{co}^2 - n_{cl}^2}{2n_{co}^2}$. Suppose that the square cross-section BB' corresponds to $\rho_x = \rho_y$ and $V=2$ for single-mode propagation, then the waveguide at cross-section AA' has $V>2$, and at CC' has $V<2$ to conserve the mode. It is then convenient to introduce a comparable normalized modal parameter W , defined by

$$W = (\rho_x \rho_y)^{1/2} (\beta^2 - k^2 n_{cl}^2)^{1/2} \quad (2.41)$$

with the local propagation constant β determined from the eigenvalue equation. Thus, the maximum permissible taper angle is expressible as

$$\Omega = \frac{\sqrt{2\Delta} W^2}{4\pi V} \quad (2.42)$$

2.4.2 Splitting Angle

The divergence of the two arms of the Y-junction in Figure 2.6 is equivalent to an up-taper, which introduces excess loss through coupling of the local supermodes to the radiation field. The excess loss will increase with increasing the angle θ of Figure 2.6. Thus, a splitter with arbitrarily low loss could be designed by making this angle sufficiently small. However, this would lead to an unacceptably long device difficult for fabrication as with the taper discussed above. Fortunately, it is possible to balance the two requirements of low loss and compactness using simple physical considerations to obtain a simple upper bound on this angle.³⁴ Since the splitting angle is a continuous from the taper, then it follows from equation (2.16) that

$$\theta < \frac{(2\Delta)^{1/2} W^2}{4\pi V} \quad (2.43)$$

where θ is the half-branching angle.

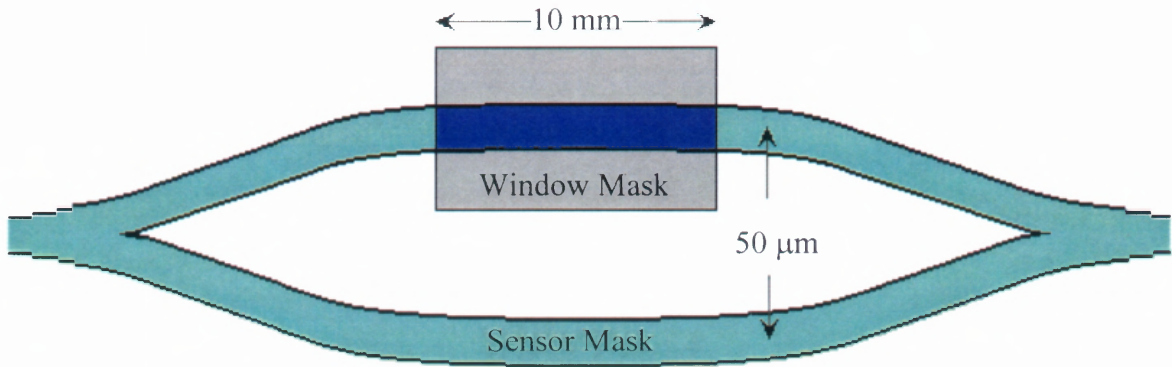


Figure 2.8 Schematic of a single sensor mask overlapped with a window mask.

2.5 Masks Design

The fabrication of the Integrated Mach-Zehnder Interferometer sensor involves two lithographic masks, one for the pattern of the sensors and the other for the opening windows of the sampling arms. Dave Soltys, an undergraduate student of NJIT, designed the masks with Mentor Graphics IC Station on a Sparc 20 workstation network. The ultra-violet exposure tool with a resolution limit of $2\ \mu\text{m}$ was used with the positive photoresist spun on the wafer.

2.5.1 Sensor Mask

The sensor mask was designed such that sensors with different arm lengths and core widths can be produced on a standard 5-inch wafer for optimal performance testing. An Integrated Mach-Zehnder Interferometer sensor with 10 mm arm length and $50\ \mu\text{m}$ of separation between both arms is as shown in Figure 2.8. The splitting angle of the Y-junction was design to meet the design criterion explained in Section 2.4.2, which was less than 2° . This was the best angle that could be achieved because of the limitation of

fabrication as mentioned early in this section. The 2- μm limitation in lithography process has produced “U” shape taper instead of the desired “V” shape Y-junction. In the mask design, sensors with different arm lengths of 10, 8, 6, 4, and 2 mm were grouped together as illustrated in Figure 2.9, and the groups with various core widths of 6, 5, 4, and 3 μm were then formed a “die”. This means a “die” consists of twenty sensors with different dimensions, and there are a total of ten “dies” on a 5-inch wafer, as shown in Figure 2.10.

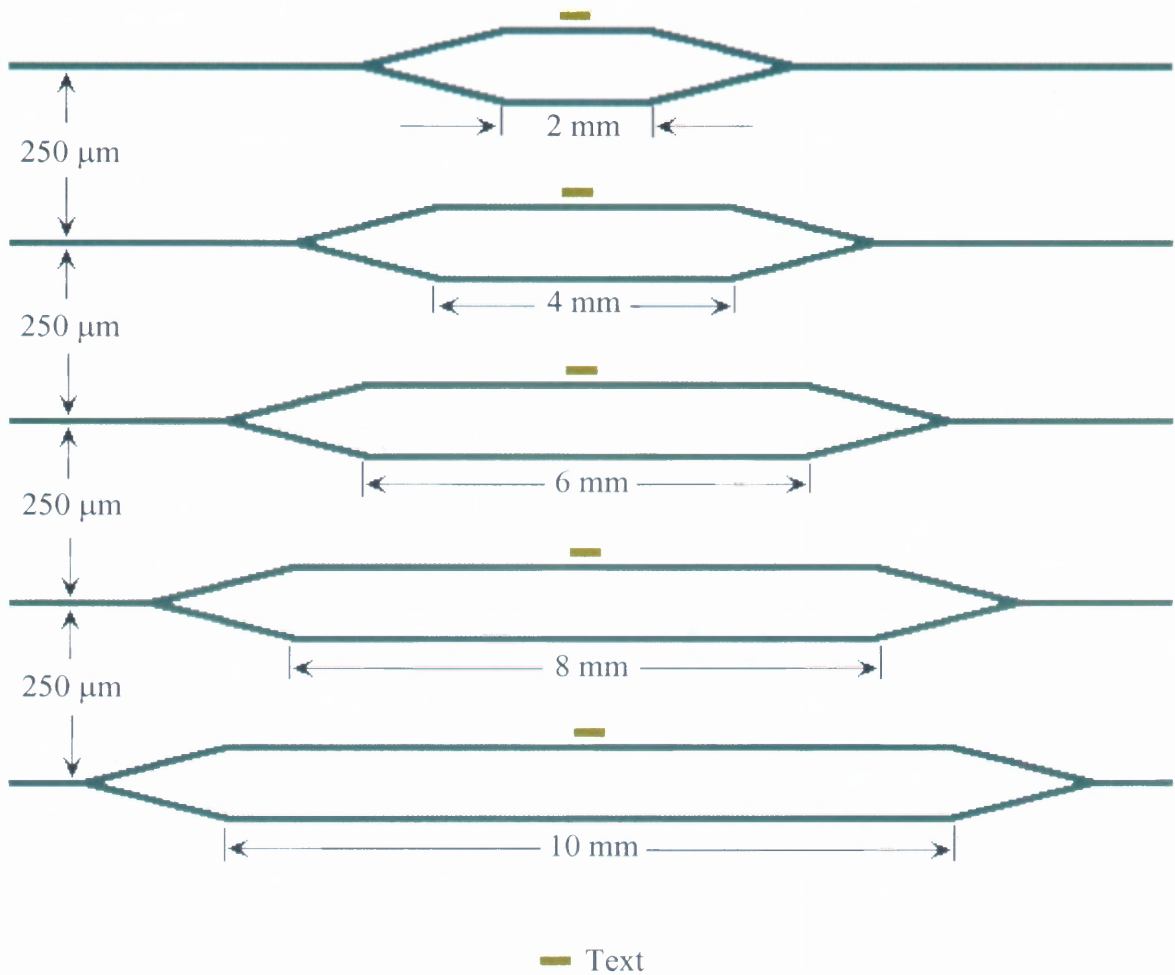


Figure 2.9 Sensor mask design with five different arm lengths grouped together.

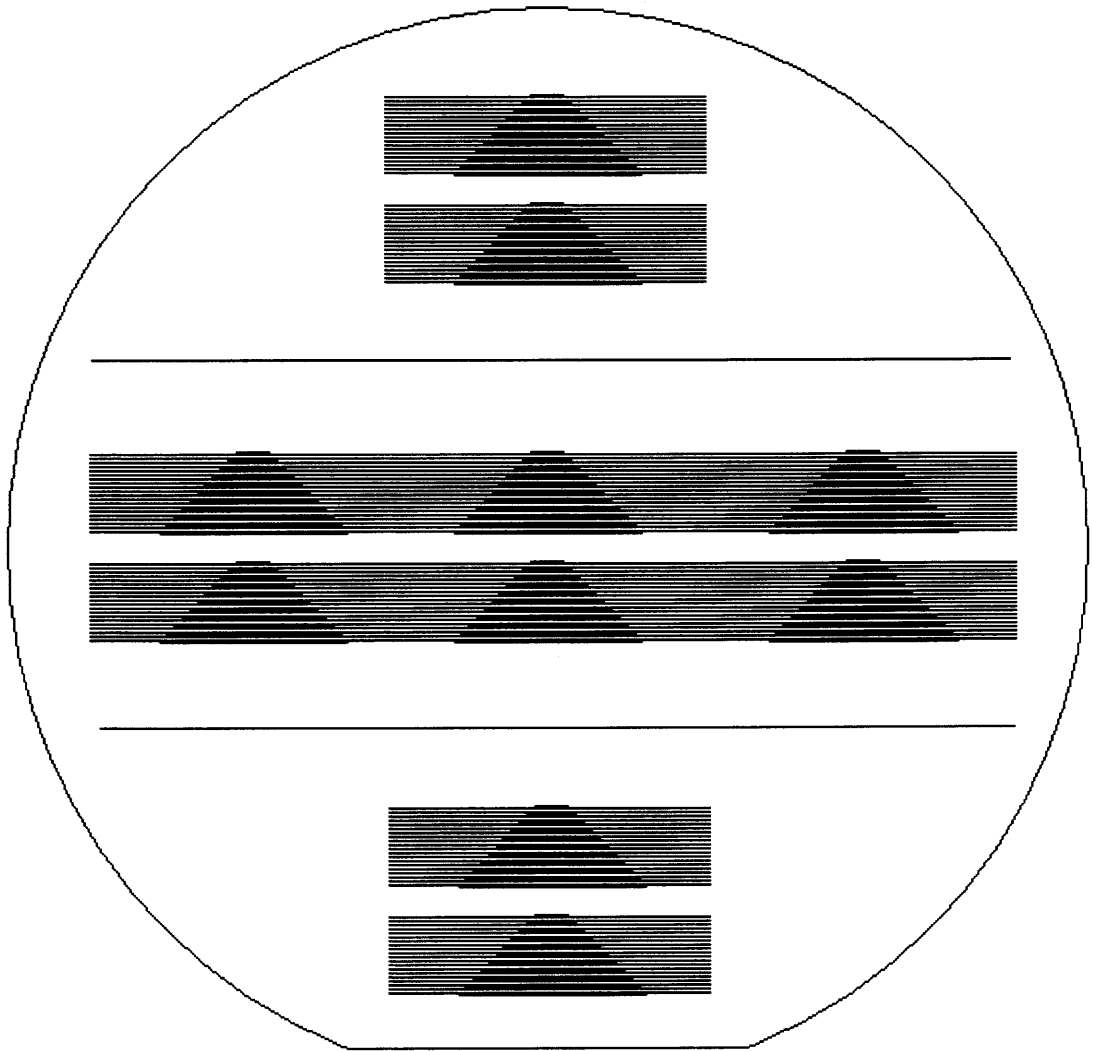


Figure 2.10 Layout of the sensor mask. (Not drawn to scale).

The core widths designed were meant for single-mode operation in the near infrared region. A small block of text describing the dimension of the sensor also imprinted for easy identifying. The texts are in the form of Width \times Length, for example, $4\text{ }\mu\text{m} \times 6\text{ mm}$. This mask was designed to pattern the actual interferometer sensor structure, so the field of the mask was selected to be in clear region except the sensor

patterns were in dark region. The clear region allows radiation goes through and exposes the photoresist coating during photolithography process so that the sensor patterns can be printed on the wafer.

2.5.2 Window Mask

Another mask needed to complete the sensor design is the window-opening mask. This mask is used to pattern an opening onto the protective oxide layer over the entire length of the sampling arm. Thus, the alignments of the window patterns have to be consistent with the sensor patterns of the sensor mask, otherwise, misalignment will occur. The lengths of the window patterns are also in 10, 8, 6, 4, and 2 μm , which is similar to the arm lengths of the sensor patterns.

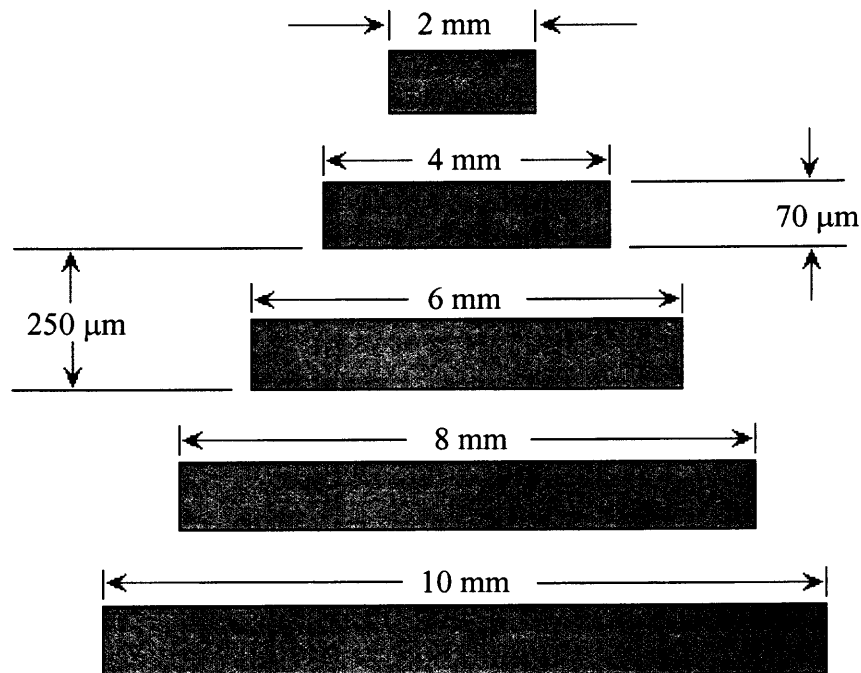


Figure 2.11 Window mask with different lengths grouped together.

The layout of a group of the window patterns is illustrated in Figure 2.11. The entire field of the mask was selected to be in dark region while the window patterns were in clear region so that the printed windows can be etched off to reveal the waveguide cores. The window width was set to 70 μm , which is remarkably large compare to the sensor arm width. The purpose of doing so is to ensure that the entire sampling arm would be properly exposed after the fabrication processes. The large window width, however, became a major problem in the photolithography processes for the window alignment, which has caused the overlapping of the window mask on both the reference and sampling arms, as discussed in Section 2.7.3.

2.6 Fabrication By Deposition and Etching

In a typical fabrication process, the silicon wafer is sometimes pre-heated in a furnace or immersed in a steam bath for an extended period in order to oxidize a layer several microns thick within and below the wafer surface to facilitate the adhesive of deposited silica and to form part of the buffer layer. After that, a uniform layer of pure silica is deposited on the surface of the wafer to a depth of 10 μm or more by Low Pressure Chemical Vapor Deposition. The thickness of the buffer layer should be large enough to minimize the loss of light through tunneling to the silicon substrate, which has a much higher index than the silica. A second layer of glass with slightly higher index than the buffer layer is deposited to form the core layer. The thickness of the core layer is determined by the requirements that the waveguide is single-mode and that the splice loss to single-mode fiber is minimum. The higher index of the core layer can be achieved by doping with suitable elements such as phosphorous, nitrogen, fluorine and germanium.

Lithography processes are then performed to transfer the waveguide pattern from the pre-designed mask on the core layer. The parts of the core layer not covered by the mask are etched away by etching processes to reveal the waveguide cross-section. A final deposition of silica completes the cladding surrounding the core waveguide.

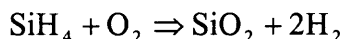
2.6.1 LPCVD

LPCVD is one of the significant developments in chemical vapor deposition processing. The introduction of this low-pressure reactor system to the semiconductor industry has brought in the intensive growth in advanced IC technology and in mass fabrication of silicon based products. These reactors can be divided into *hot wall* and *cold wall* systems. Hot wall system have the advantage that the temperature flow is distributed evenly through out the whole chamber to eliminate the convection effect, while the cold wall system is capable to reduce the deposition on the chamber wall. The deposition on the chamber wall lead to formation of deposition particles and hence contaminate the wafers. The gas pressure employed in the LPCVD reactors is ranging from 0.1 to 1.0 Torr, which is considerably low compared to the conventional CVD process with around 760 Torr of gas pressure. However, the concentration of the input reactant gas has to be increased relative to the atmospheric reactor case to compensate for the low pressure.

The most common reactor is horizontal LPCVD reactor, consists of a cylindrical quartz tube heated by wire wound elements. The wafers to be deposited are lined vertically along the chamber. A large mechanical pump is required to accommodate the gas flow rates and to maintain the gas pressure. A recent innovative vertical LPCVD reactor has been introduced and this system has more advantage than the horizontal

reactor such as the wafers are stacked up along the chamber horizontally for easy access by robotic handling, and the reduced particles counts.

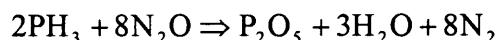
2.6.1.1 LPCVD of SiO₂. LPCVD of SiO₂ is generally based on the reaction between silane and oxygen under low-pressure:



Some new precursors such as diethylsilane and butoxysilane have been used to replace the toxic and explosive silane for generating good quality films and optimizing the deposition conditions. The deposition temperature is set to around 475°C and gas pressure is controlled at around 0.5 Torr for the diethylsilane and oxygen interaction to form the silica film. Diethylsilane has a vapor pressure as high as 207 Torr at room temperature. It is more favorable in used as the reactant for the SiO₂ deposition because no heating of the liquid source is necessary and it is environmentally safe. The silica film deposited under these conditions has refractive index of 1.456 and etching rate ranging from 850 to 1000 Å/min. depends on the etching method used.

2.6.1.2 LPCVD of Phosphosilicate Glass. The core material of a waveguide determines the mode properties of the optical waveguide. In order to maintain mode propagation, the core must have higher index of refraction compare to that of the cladding and buffer layer surrounding the core to sustain the total internal reflection. This can be achieved by doping of phosphorous into the silica to form the so-called phosphosilicate glass (PSG). The PSG can be synthesized on top of the buffer layer by means of LPCVD process.

The adding of a small amount of phosphorous into the LPCVD reactor together with the oxidation of silane by either nitrous oxide or oxygen produces a thin layer of PSG on top of the silica buffer layer. The chemical processes can be summarized as below,



It is easy to integrate the P_2O_5 into the SiO_2 to form the PSG material, as the $\text{SiO}_2:\text{P}_2\text{O}_5$ ratio in the deposited film is controlled by the ratio of $\text{SiH}_4:\text{PH}_3$ in the flowing gas.

SiO_2 film has been deposited at reduced pressure and low temperature, taking the advantages of the LPCVD. The phosphosilicate film, however unfortunately, does not have these advantages. The step coverage of the film deposited at low temperature is non-conformal. Heat-treatment at around 1100°C usually used to flow the glass in order to get uniform step coverage but this high temperature treatment is not acceptable for very short channel devices where shallow junctions are required. This can be improved by using the decomposition of organosilicon and organophosphorus compound in mid-temperature ranging from 600°C to 800°C , to get consistent step coverage.

PSG is a binary glass that consists of two compounds, namely SiO_2 and P_2O_5 . The physical properties of the phosphorous-doped silica glass are expected to be related to the chemical structure and composition of the phosphorous species in the silica network. When the PSG film was formed at a relatively low temperature, the phosphorous in the film was considered to be in such a state that small particles of P_2O_5 , rather than the compound $\text{SiO}_2.\text{P}_2\text{O}_5$, were dispersed in the SiO_2 matrix.³⁵ The SiO_2 matrix, which is water-insoluble, protects the P_2O_5 from being diffused by the water. As the P_2O_5 reached

a certain critical concentration, the volume fraction of the P_2O_5 to the SiO_2 matrix increases, and the SiO_2 matrix no longer effective in protecting the P_2O_5 from the moisture attack. The SiO_2 has a larger angular distribution width of Si-O-Si bond when formed at low temperature, and becomes highly porous to water,³⁶ causing the P_2O_5 to dissolve. Heat treatment increases the density of the SiO_2 matrix, which in turn makes it hard for water vapor to diffuse the P_2O_5 , and also intensifies the reaction between P_2O_5 and SiO_2 matrix to form the water-insoluble compound $(SiO_2)_x.(P_2O_5)_y$.

The concentration of the P_2O_5 is an important parameter for forming the PSG film because of its solubility to water as explained above. The phosphorous content inside the PSG film controlled the film properties. At high concentration, the PSG film becomes hygroscopic, produces corrosive compounds, and forms microcrystallites. While at low concentration, the refractive index of the PSG film is not increased enough to be the waveguide core. So it is important to control and determine this composition so as to make it useful. This is accomplished by controlling the temperature and reactant gas composition during the deposition of the PSG film.

2.6.2 Photolithography

One of the most important procedures in the integrated optics fabrication is the photolithography process. Opto-electronics circuits or devices are in the micron range, and this required micro technology processes to increase the resolution. Photolithography is the process used to transfer the integrated circuit's pattern to the buffer layer. Before doing so, a thin coat of photoresist material is applied on top of the buffer layer. The photoresist coating is then exposed to a form a radiation, such as UV, electrons, or X-rays, with the mask positioned on top of the wafer, as shown in Figure 2.12. The pattern

formed on the photoresist layer according to the mask pattern is then undergone subsequent development steps to produce the integrated optical pattern on the buffer layer.

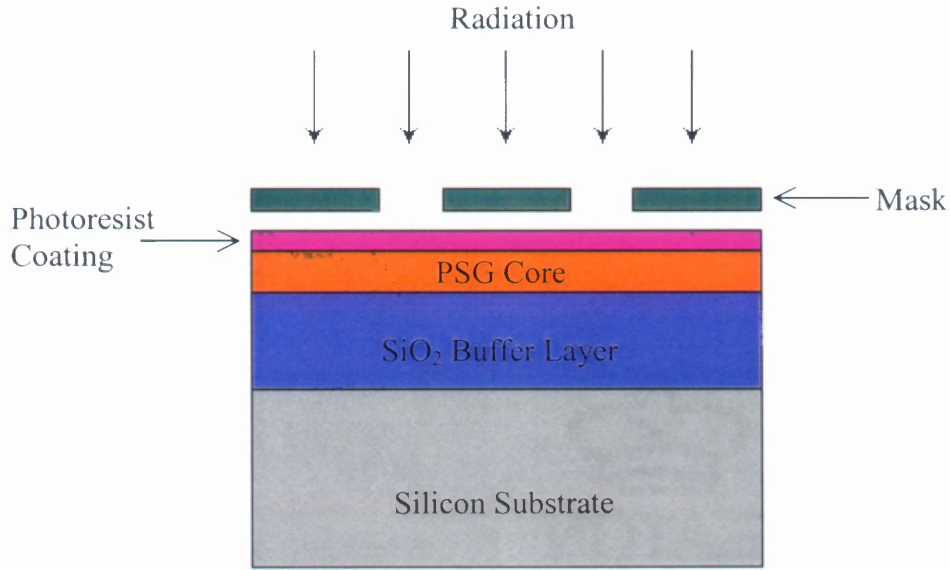


Figure 2.12 Schematic representation of photolithography process.

The photoresist area that is exposed to the radiation is made soluble or insoluble in a specific solvent known as developer, to produce the so-called positive photoresist or negative photoresist, respectively. After development, the regions not covered by the photoresist are removed by etching process, thereby replicating the mask pattern on the buffer layer.

2.6.3 Etching

Etching is the process to remove parts of the materials that is not covered by the photoresist from the thin film on the buffer layer or substrate surface. This process is not

completely capable to transfer the pattern established from the photolithography process into the underlying materials. Degree to which the process fails to satisfy the ideal etching is specified by two parameters, i.e. bias and tolerance. Bias is the difference between the etched image and the mask image created by the photolithography process, while the tolerance is a measure of statistical distribution of bias values that characterizes the uniformity of etching.

The rate at which the materials are etched off is known as etch-rate with units of Å/min., µm/min, etc. In general, high etch rates are desirable as they allow higher production throughputs. In some cases, however, high etch rates become a trouble in controlling lateral etching, since material removal can happen in both horizontal and vertical directions. The horizontal etch rate has to be established in order to characterize an etching process.

In the cases of an ideal etch process the mask pattern would be transfer to the underlying layer with zero bias so that a vertical edge is created. This means that the lateral etch rate would be zero as well. For non-zero lateral etch rate, the material is etched to some degree under the mask, and hence create the *undercut* effect. When the etching proceeds in all directions at the same rate, it is said to be isotropic. Otherwise, it is anisotropic if the etching proceeds only in vertical direction. The typical isotropic and anisotropic etch profile is shown in Figure 2.13. Isotropic etch profile can be corrected by using a special technique called *Dry Etching*, instead of *Wet Etching*, as discussed in the following section

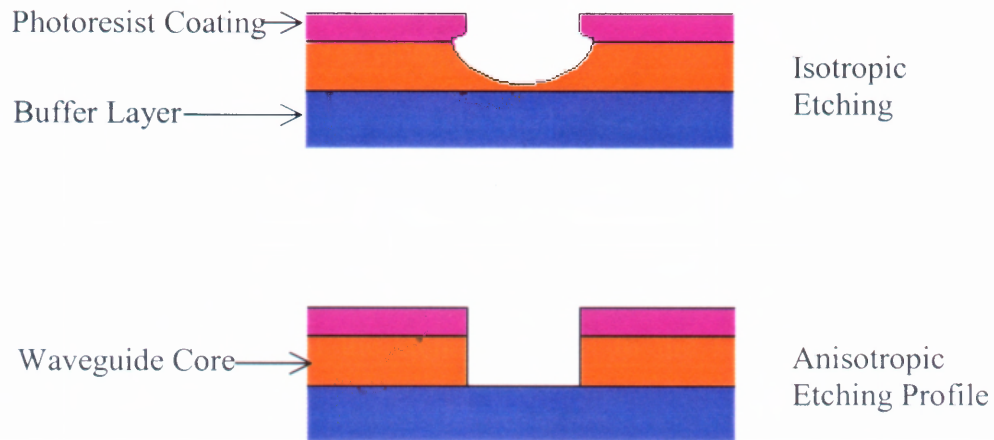


Figure 2.13 Isotropic and anisotropic etching profile.

Both the photoresist and the buffer layer are etch-able by the etchant, and this effect plays a significant role in the etching process. Fortunately, different materials have different etch rates, and the ratio of the etch rates of different materials is known as selectivity of an etching process. Hence, both the selectivity with respect to the photoresist material and the selectivity with respect to the buffer layer are important characteristic to the etching process.

2.6.3.1 Wet Etching. Wet etching is a purely chemical process that can have serious drawbacks such as lack of anisotropic, poor process control, and excessive particle contamination. However, wet etching can be highly selective and usually does not damage the photoresist and the layer underneath. This etching process consists of three steps: (i) movement of the etchant species to the surface of the wafer; (ii) a chemical reaction with the exposed film that produces soluble byproducts; and (iii)

movement of the reaction products away from the wafer. Since all three steps must occur at once, the slowest one, called the rate limiting step, will determine the etch rate.

For most wet etching process, the film to be etched is not directly soluble in the etchant solution. It is usually needed to change the material to be etched from a solid to a liquid or a gas. If the etching process produces a gas, unpredicted bubbles will be formed from the gas, and prevent the fresh etchant near the film surface. This problem is most profound near the pattern edges. In order to overcome this, agitation in the wet chemical bath is used to assist the movement of fresh etchant to the surface of the wafer. Besides, it will also reduce the ability of the bubbles to adhere to the wafer. Another common problem for wet etching is the undetected resist scum, occurs when some of the exposed photoresist is not completely removed in the development process due to incomplete exposure or insufficient developing of the pattern. A very thin layer of this photoresist remaining is sufficient to block the wet etching process.

2.6.3.2 Dry Etching. Undercutting due to isotropic etching sometimes can be intolerable if the thickness of the film being etched is comparable to the minimum pattern dimension. Another alternative pattern transfer method that offers the capability of anisotropic etching is dry etching. There are a variety of dry etching processes. The mechanism of etching in each type of process can have (i) a physical bias, for example, glow-discharge sputtering; (ii) a chemical bias, such as plasma etching; (iii) a combination of the two, i.e. reactive ion etching (RIE); and (iv) reactive ion beam etching (RIBE).

In processes that depend mainly on the physical mechanism of sputtering, including the reactive ion beam etching, the strongly directional nature of the incident

energetic ions allows the materials to be removed in a highly anisotropic manner, i.e. essentially vertical etch profiles are produced. However, this mechanism does not produce selectivity against both the photoresist and the layer underneath the film being etched. On the other hand, purely chemical mechanism for etching can exhibit a very high selectivity against both the photoresist and underlying materials. Such purely chemical etching mechanism, however, typically etch in an isotropic fashion.

By adding a physical component to a purely chemical etching mechanism, the shortcomings of both the physical based and purely chemical dry etching process can be prevailed. An ideal dry etching process based solely on chemical mechanism for material removal consists of six steps: (i) reactive species are generated in plasma state; (ii) these species diffuse to the surface of the material being etched; (iii) the species are absorbed on the surface; (iv) chemical reaction occurs with the formation of a volatile by-product; (v) the by-product is desorbed from the surface; and (vi) the desorbed by-product diffuse into bulk of gas. The overall etching process will end if any of these steps fail to occur. Many reactive species can react rapidly with a solid surface but unless the product has a reasonable vapor pressure so that desorption occurs, no etching will take place.

2.6.4 Fabrication of the Integrated MZI Sensors

Figure 2.14 and Figure 2.15 show the fabrication procedures of the ridge-waveguide Integrated Mach-Zehnder Interferometer sensor. The first two layers of the thick SiO₂ and the PSG are deposited on the silicon wafer by LPCVD. The mask of the Integrated Mach-Zehnder Interferometer sensor pattern is then transferred onto the wafer surface by using the standard technique of photolithography, namely, photoresist spinning, lithography exposure and development. After plasma etching and photoresist elimination

processes, the square waveguide goes through annealing at 1050°C to create a flow edge, to minimize coupling losses between fiber and waveguide. Another layer of SiO₂ is then deposited on top of the waveguide core to achieve light guiding by total internal reflection. Subsequently followed by transferring the window mask onto the wafer to open a window on the sensing arm, using similar steps of photolithography. The window mask has to be properly aligned on top of the sensors so that the windows opening are opened exactly on the sampling arm. This alignment is crucial since the window mask tends to misalign during the exposure process. After that, the plasma etching and photoresist removal steps finalize the Integrated Mach-Zehnder Interferometer sensor. The detail of the fabrication procedures is listed in Appendix A.

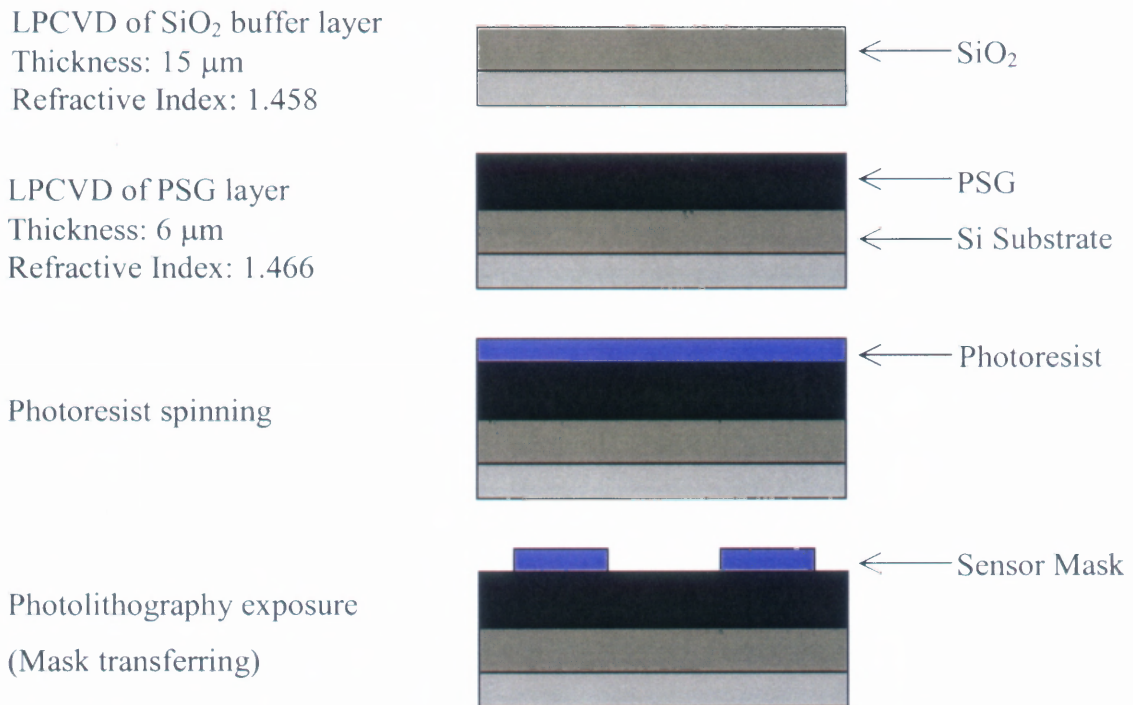


Figure 2.14 Fabrication processes of the Integrated MZI sensor. (Not drawn to scale) (continued).

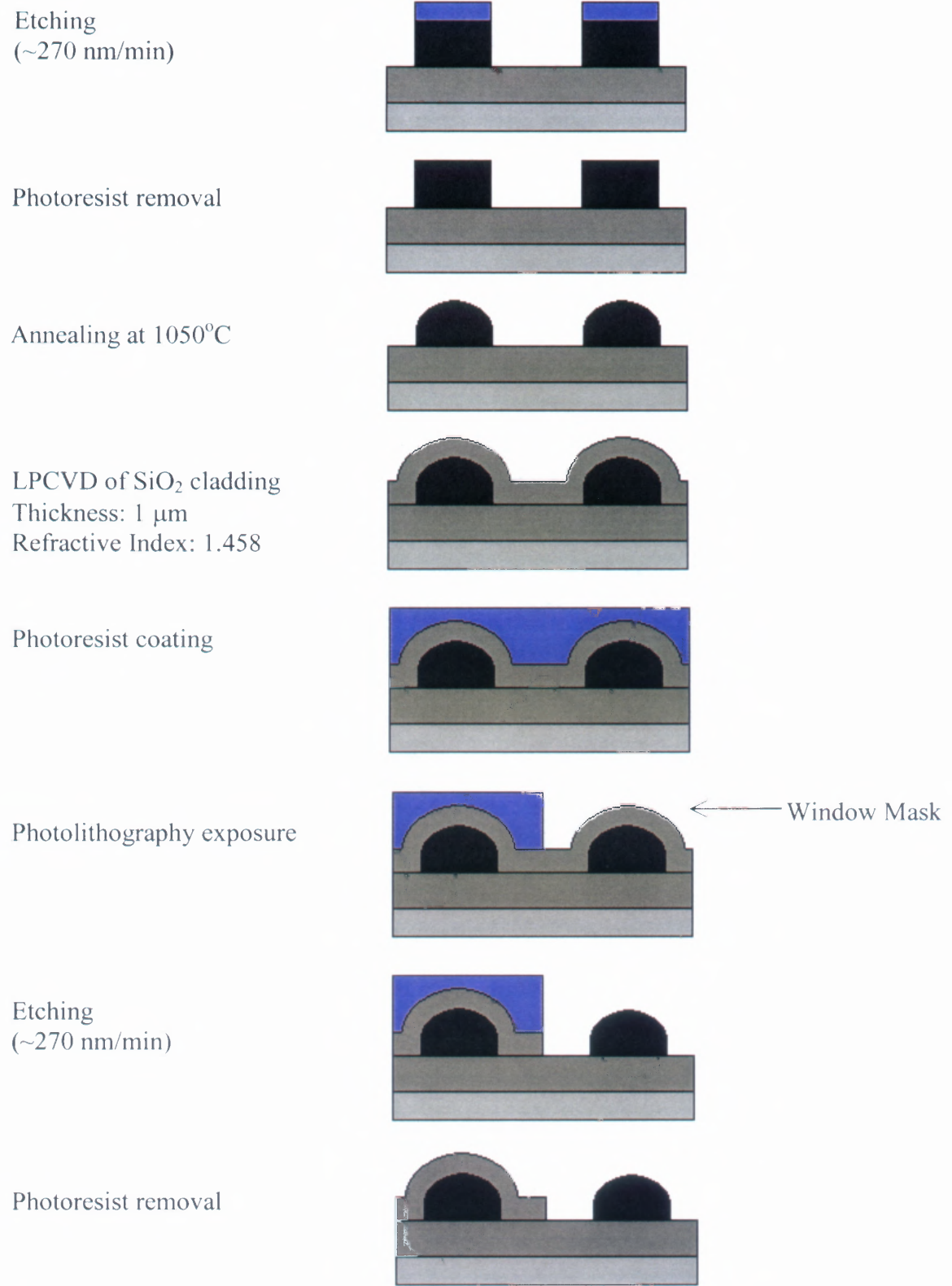


Figure 2.15 Fabrication processes of the Integrated MZI sensor. (continued)

2.7 Functionality Testing on Integrated MZI Sensor

It is important to analyze the waveguides after fabrication to make sure that the sensors are working as expected. The experimental testing on the separated waveguide portions of the first batch Integrated Mach-Zehnder Interferometer sensors are described. These testing procedures were also carried out for the subsequent fabricated batches of the integrated MZI sensors until optimum performance is achieved, and the testing results are discussed in detail in Chapter 5.

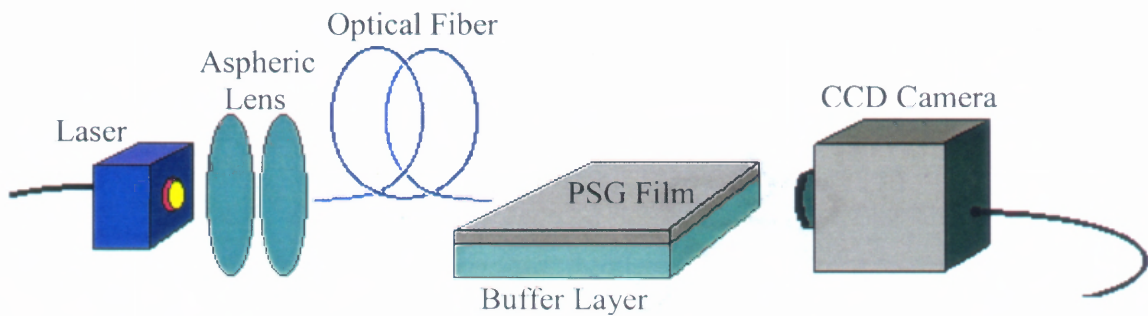


Figure 2.16 Experimental setup for the waveguide core testing.

2.7.1 Wave Guiding Core

The phosphosilicate glass (PSG) film has optical property of higher refractive index than its host, i.e. the silicon dioxide. This property is the only requirement for light transmitting along the waveguide via total internal reflection. The concentration of phosphorous in the silica controls the variation of this optical property and hence affects its functionality as waveguiding material. The condition of PSG deposition is crucial, as explained in Section 2.6.1, to create an optimal waveguide for sensing principle. Therefore, it was appropriate to test on the PSG film for different deposition conditions to

optimize the doping criterion. Figure 2.16 illustrates a simple experimental setup used to test the PSG film. Two different laser sources with 633 nm and 830 nm wavelengths were used, and as can be seen in Figure 2.17 that the PSG thin film is transparent to the light compare to that of the silica buffer layer.

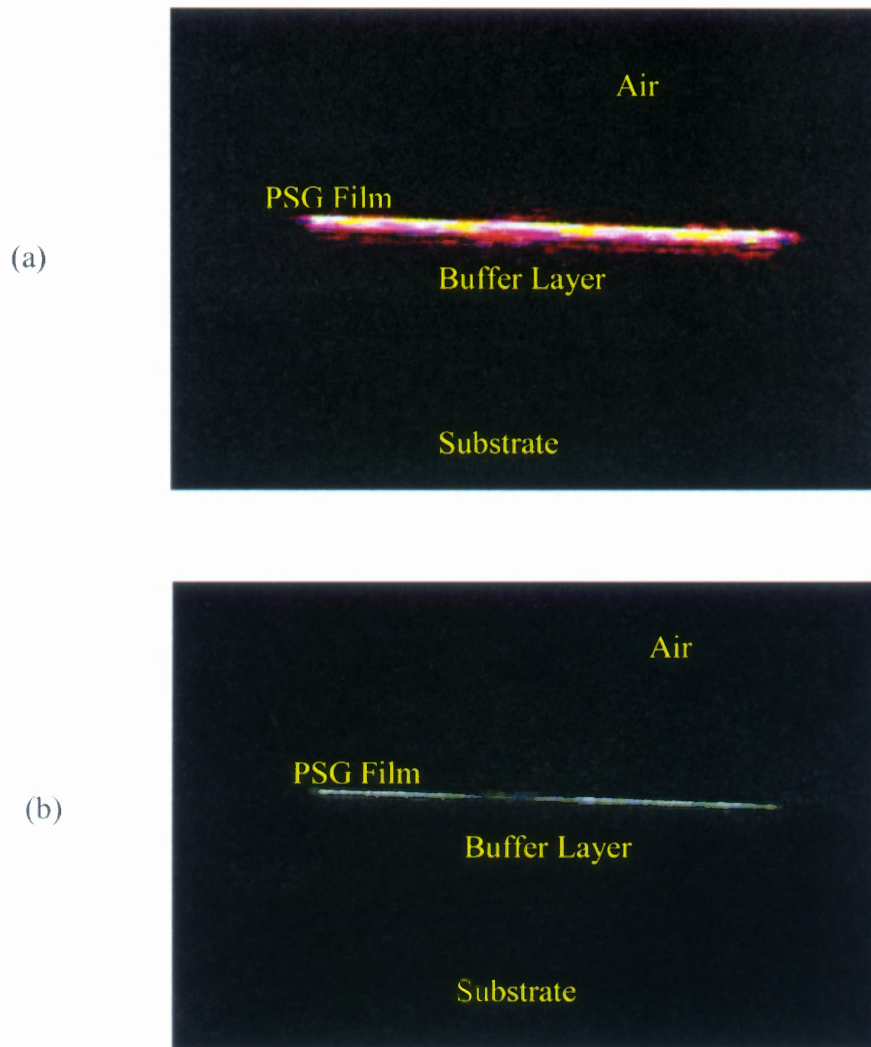


Figure 2.17 PSG is transparent to light with wavelengths of (a) 633 nm and (b) 830 nm.

2.7.2 Y-junction

The structure as well as the functionality of a Y-junction has been discussed in previous section. This Y-junction, also called the 3 dB Y-splitter is supposed to split the light equally into the two arms of the integrated Mach-Zehnder Interferometer sensor. The light split by the Y-junction will then recombined by another reversed Y-junction at the other end of the sensor to produce interference. Interference occurs only when the two recombined light beams are coherent. The coherency of the light may be affected by the waveguides due to scattering by defects produced during fabrication or by inconsistency of the phosphorous doped during deposition. Thus it is important to test the coherency of the light after the Y-junction in addition to the 3dB splitter.

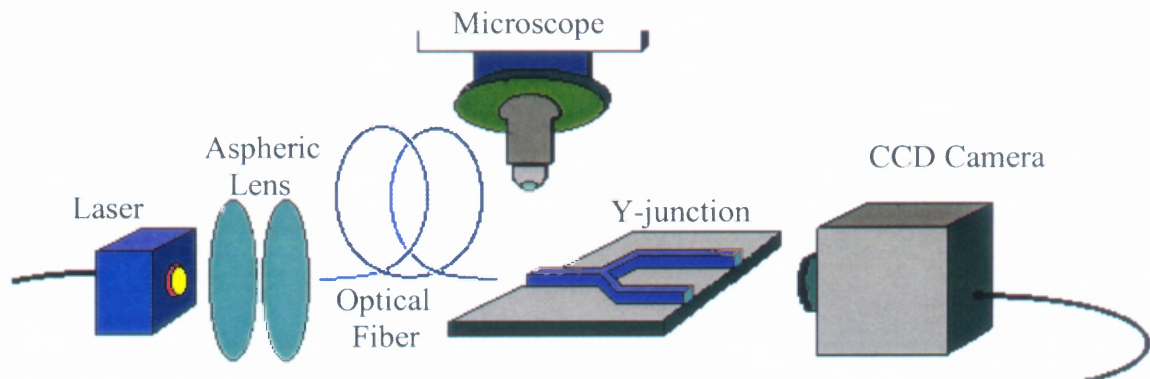


Figure 2.18 Experimental setup for the testing of the 3dB splitter.

2.7.2.1 3dB splitter. An experiment was set up to test the Y-junction portions of the integrated Mach-Zehnder Interferometer sensor. The schematic of the setup is illustrated in Figure 2.18. The sensor was cleaved across before the window opening of the sampling arm, showing the end side of the Y junction profile as shown in Figure 2.19.

The laser beam was coupled into the incidence opening and to be split evenly at the junction into the two arms, which would be detected at the two output ends of the waveguides by a CCD camera. Before coupling the laser beam into the waveguide, the output end of the Y-splitter did not illuminate, as can be seen in Figure 2.19, while Figure 2.20 indicates an *almost* equal light intensity at both output ends after the laser is coupled into the waveguide.

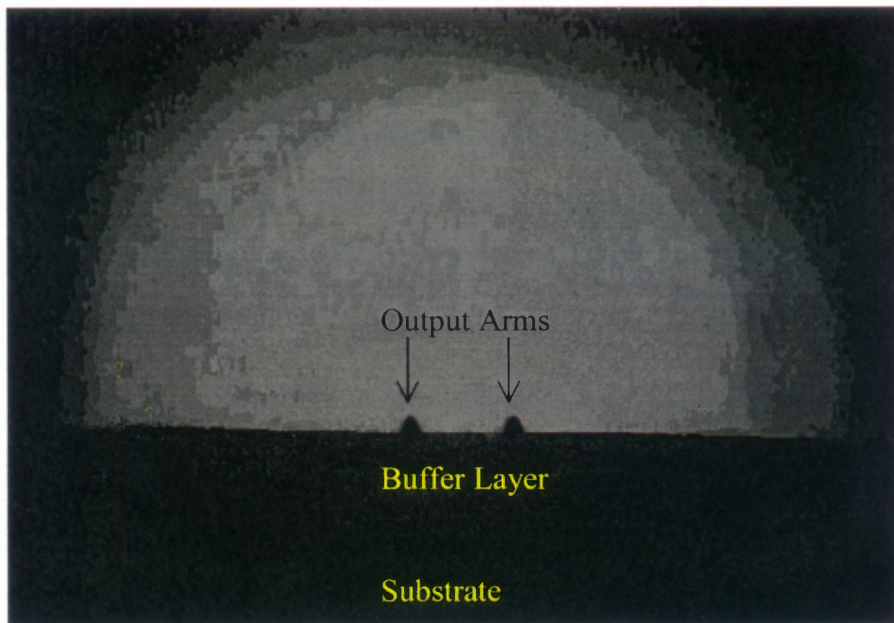


Figure 2.19 The output arms profile of a Y-junction before coupling light in.

The actual power split of the second-batched Y-junction was also investigated by replacing the CCD camera with a fiber out-coupled from the output end of the Y-junction to an optical spectrum analyzer for output intensity measurement using a broadband source. The power measured revealed that the second-batched Y-junction actually

exhibits a 60%-40% split (60% from reference arm, 40% from sampling arm) instead of the expected 50%-50% split, as discussed in Chapter 4.

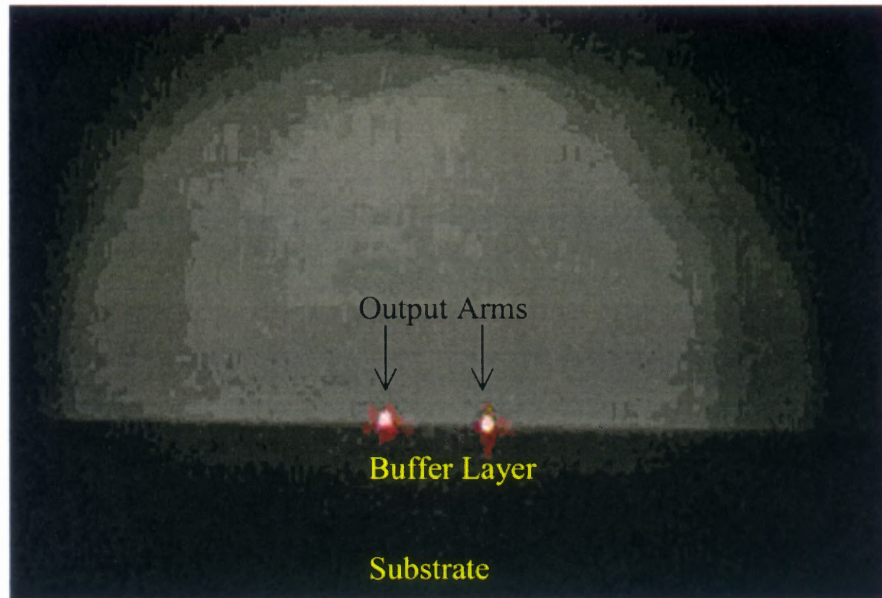


Figure 2.20 Light propagates through the Y-junction.

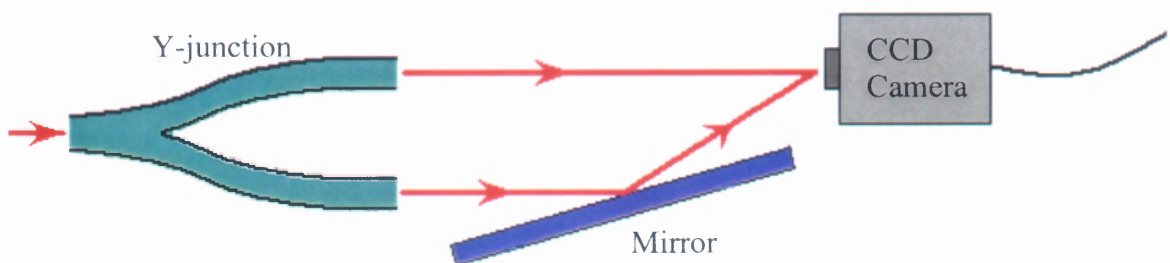


Figure 2.21 Schematic setup to examine the light coherency.

2.7.2.2 Interference. Subsequently, testing for the coherency of the output beams was performed by using a mirror to divert one beam to the other as illustrated in Figure 2.21. The result captured by the CCD camera exhibited the interference property of the light after propagating through the Y-junction when one of the beams was directed to superimpose with the other, as shown in Figure 2.22. It also demonstrated the fringe shifting caused by the displacement of the mirror. This has confirmed that the light does maintain its coherency after transmitting through the waveguides and the Y-junction.

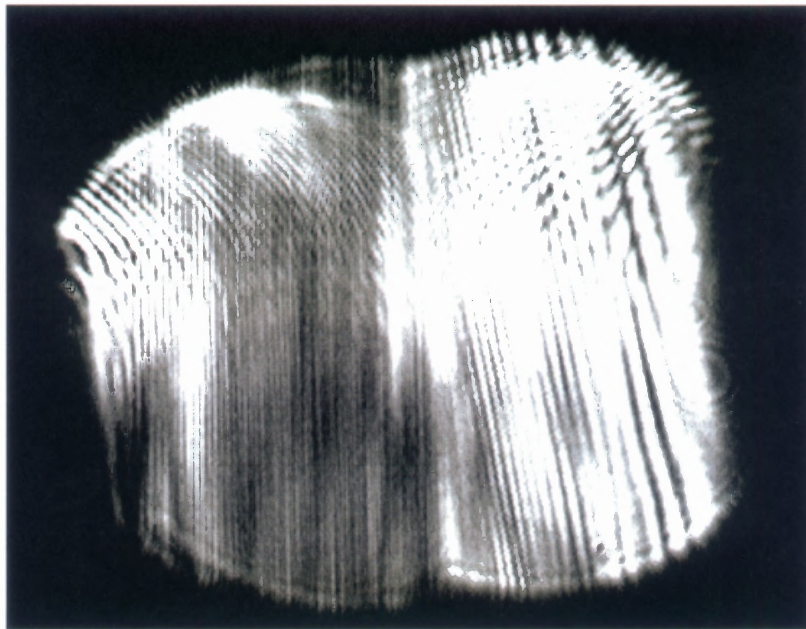


Figure 2.22 Interference caused by superimposed of two beams output from a symmetry Y- junction.

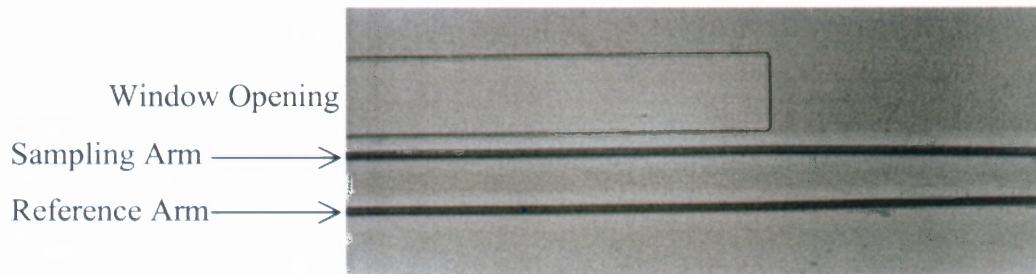
2.7.3 Sensing Area

The sensing area of the sampling arm consists of an opening window where the waveguide core is exposed to the chemical species when used as a chemical sensor. This means that the sensing area exhibits an important task for sensing chemical. If this area does not exposed adequately to the chemical species, then no sensing mechanism occurs, and this leads to the failure of the purpose. Another critical cause to the failure is the exposed waveguide core of the sampling arm became smaller than the waveguide core of the reference arm after the etching process, resulting in unequal light intensity emerge into the Y-combiner, consequently affect the output results.

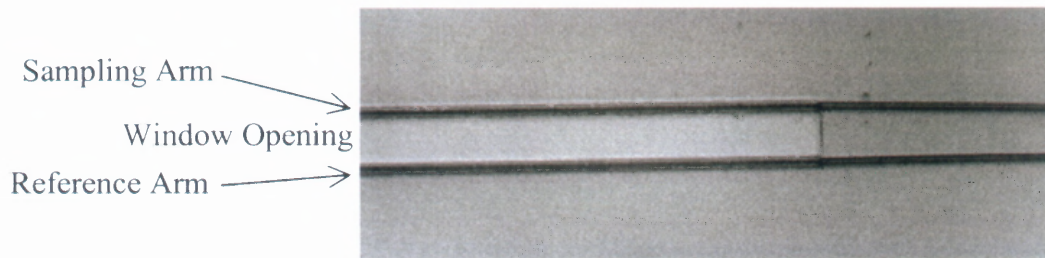
Hence, it is the idea of this section that the sensing area, which is the exposed arm or sampling arm as stated in previous section, be thoroughly scrutinized under the microscope for the investigation of fabrication defects as mentioned. At first, the sensor was placed flatly under the microscope for the window alignment examination. It was found that some of the sensors have serious misalignment. As can be seen in Figure 2.23(a), a window was not opened at the correct position on the waveguide of the sampling arm; instead it was located away from the sensor. In contrast, Figure 2.23(b) shows that the window was opened exactly on top of the waveguides of both sampling and reference arms.

Finally, those sensors with proper windows alignment were cleaved at the center of the window opening so that the core size could be inspected. The cleaved sensor was positioned such that the profile side to be investigated could be examined by the microscope. The image of the waveguide cores profile of the sampling and reference arms is demonstrated in Figure 2.24. The picture shows that the waveguide core of the

sampling arm is smaller compare to that of the reference arm. This “over-etched” situation is mainly due to the improper control of the selectivity etch rate during the etching process, and also because of the drawback of using the wet etching as discussed in Section 2.6.3.



(a)



(b)

Figure 2.23 Window misalignment: (a) off from the sampling arm, and (b) overlapped on both arms.

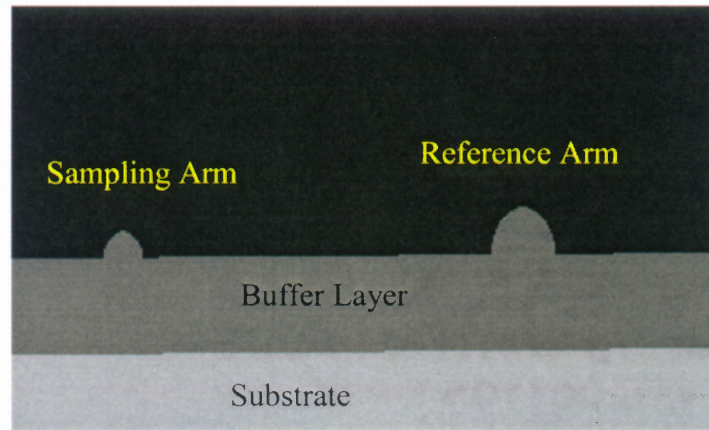


Figure 2.24 Over-etching into the waveguide core of the sampling arm.

The overlapping of the window mask and the sensor mask has to be properly aligned during the lithography exposure processes to overcome this misalignment condition. Moreover, the window mask should not be wider than the arms separation of the sensor, because after fabrication, the exact window will become broaden than the window mask itself due to the isotropic property of wet etching. As shown in Section 2.5, the window mask has $70\text{ }\mu\text{m}$ width while the sensor has only $50\text{ }\mu\text{m}$ separation in between the sampling arm and the reference arm. This has caused the overlapping of one window on top of both the sampling and reference arms.

CHAPTER 3

COMPUTATIONAL WAVEGUIDES DESIGN WITH FEM

The origin of the finite element method (FEM) is frequently traced to Courant who in the 1940s first discussed piecewise approximations.³⁷ In the 1950s, Argyris began putting together the many mathematical ideas that comprise the FEM for aircraft structural analysis.³⁸ The introduction of FEM to the engineering community occurred in the 1960s, while some feel that the conferences on finite elements held in 1965, 1968, and 1970 at the Wright Patterson Air Force Base in Dayton, Ohio, U.S. played a crucial role in advancing the method. Later development on absorbing boundary conditions, perfectly matched absorbers and hybridizations with boundary integral method have led to the successful application of the FEM to open domain problems in scattering, microwaves circuits and antennas.³⁹ The method's main advantages are its capability to treat any type of geometry and material inhomogeneity without a need to alter the formulation or the computer program. That is, it provides geometrical fidelity and unrestricted material treatment. Moreover, the application of the FEM leads to a sparse matrix system, which can be stored with low memory requirements when iterative solvers are employed for the solutions of these systems. Typically, FEM system have $O(N)$ storage requirements, implying that the memory needed for a solution of an FEM system is proportional to the number of unknowns N . This would depend on the number of dimension and the nature of the partial differential equation. For most cases, these memory requirements may range from $10N$ to $50N$ depending on the type of problem considered and the employed basis or shape functions approximating the field within the computation domain.

Finite Element Method will be used to determine the wave propagation characteristics in optical waveguides. The electromagnetic Maxwell equations, both in vacuum and in dielectric, are solved to study the wave properties. Scalar and vector finite elements shape functions are described. Elemental FEM matrix is determined, and assembled into a global FEM matrix. The FEM codes are written in Matlab program. This method is suited for problems involving complicated geometries and variable index of refraction. The essence of the Finite Element Analysis is the discretization of the waveguide's cross-section and its surrounding into a large number of small elements. It is important to model the dielectric waveguide region by as many elements as needed in order to show the physical behavior precisely. Herein, triangles or quadrilateral elements will be used. However, the triangle element is preferred because two triangles can be assembled into a quadrilateral. Therefore, only the elemental properties for a triangle will be used.

3.1 Basic Concept of Wave Theory

In this section, fundamental electromagnetic concepts and theorems are explained along with the notations employed throughout the whole chapter.

3.1.1 Time-Harmonic Maxwell's Equation

The study of harmonically varying fields with an angular frequency of $\omega = 2\pi f$ is of primary interest since finite element method for electromagnetics utilizes time-harmonic fields. The time-harmonic electric field is related to the time-dependent electric field by

$$\begin{aligned}\bar{E}(x, y, z; t) &= \text{Re}[E(x, y, z)e^{j\omega t}] \\ &= \hat{x}E_{x_0} \cos(\omega t + \phi_x) + \hat{y}E_{y_0} \cos(\omega t + \phi_y) + \hat{z}E_{z_0} \cos(\omega t + \phi_z)\end{aligned}\quad (3.1)$$

where $j = \sqrt{-1}$ and the complex vector

$$\mathbf{E}(x, y, z) = \hat{x}E_x e^{j\phi_x} + \hat{y}E_y e^{j\phi_y} + \hat{z}E_z e^{j\phi_z} \quad (3.2)$$

is referred to as the field phasor. A simplified set of equations can be obtained by introducing equations (3.1) and (3.2) into the time-dependent Maxwell's equations⁴⁰

$$\nabla \times \mathbf{H} = \mathbf{J} + j\omega\epsilon\mathbf{E} \quad (3.3)$$

$$\nabla \times \mathbf{E} = -\mathbf{M} - j\omega\mu\mathbf{H} \quad (3.4)$$

$$\nabla \cdot (\mu\mathbf{H}) = \rho_m \quad (3.5)$$

$$\nabla \cdot (\epsilon\mathbf{E}) = \rho \quad (3.6)$$

where the corresponding vector field and the current phasors are

\mathbf{E} = electric field intensity in volts/meter (V/m)

\mathbf{H} = magnetic field intensity in amperes/meter (A/m)

\mathbf{J} = free carrier current density in amperes/meter² (A/m²)

\mathbf{M} = magnetic current density in volts/meter² (V/m²)

And the two charge phasors are

ρ = free electric charge density in coulombs/meter³ (C/m³)

ρ_m = magnetic charge density in webers/meter³ (Wb/m³)

Both the \mathbf{M} and the ρ_m are fictitious quantities introduced for convenience, since there is no magnetic monopole exists, i.e. $\nabla \cdot \mathbf{B} = 0$, and hence $\rho_m = 0$.

Implied in these time-harmonic equations are the constitutive relations for an isotropic medium

$$\mathbf{D} = \epsilon\mathbf{E} = \epsilon_o\epsilon\mathbf{E} \quad (3.7)$$

$$\mathbf{B} = \mu\mathbf{H} = \mu_o\mu\mathbf{H} \quad (3.8)$$

$$\mathbf{J} = \sigma \mathbf{E} \quad (3.9)$$

$$\mathbf{M} = \sigma_m \mathbf{H} \quad (3.10)$$

where the two additional phasors

\mathbf{D} = electric flux density in coulombs/meter² (C/m²)

\mathbf{B} = magnetic field density in webers/meter² (Wb/m²)

are related to \mathbf{E} and \mathbf{H} , respectively. These constitutive equations are an important connection between the original time-dependent form of Maxwell's equations and the time-harmonic form used in the finite element method. Similarly, the phasor forms of the continuity equations are given by

$$\nabla \cdot \mathbf{J} + j\omega\rho = 0 \quad (3.11)$$

$$\nabla \cdot \mathbf{M} + j\omega\rho_m = 0 \quad (3.12)$$

The material constants are given by

ϵ_0 = free space permittivity = 8.854×10^{-12} farads/meter (F/m)

μ_0 = free space permeability = $4\pi \times 10^{-7}$ henrys/meter (H/m)

ϵ_r = medium's relative permittivity constant

μ_r = medium's relative permeability constant

σ = electric current conductivity in mhos/m

σ_m = magnetic current conductivity in ohms/m

Summarizations of Maxwell's equations in phasor form for isotropic media are

$$\nabla \times \mathbf{H} = \mathbf{J} + j\omega\epsilon\mathbf{E} \quad (3.13)$$

$$\nabla \times \mathbf{E} = -\mathbf{M} - j\omega\mu\mathbf{H} \quad (3.14)$$

$$\nabla \cdot (\mu\mathbf{H}) = -(\nabla \cdot \mathbf{M})/j\omega \quad (3.15)$$

$$\nabla \cdot (\epsilon \mathbf{E}) = -(\nabla \cdot \mathbf{J}) / j\omega \quad (3.16)$$

where equations (3.11) and (3.12) was employed to rewrite (3.5) and (3.6) as given above.

The corresponding integral representations of (3.13) to (3.16) are

$$\oint_C \mathbf{H} \cdot d\mathbf{l} = \iint_S (\mathbf{J} + j\omega\epsilon\mathbf{E}) \cdot d\mathbf{S} \quad (3.17)$$

$$\oint_C \mathbf{E} \cdot d\mathbf{l} = -\iint_S (\mathbf{M} + j\omega\mu\mathbf{H}) \cdot d\mathbf{S} \quad (3.18)$$

$$\oiint_{S_c} \mu\mathbf{H} \cdot d\mathbf{S} = -\iiint_V \frac{\nabla \cdot \mathbf{M}}{j\omega} dV = \iiint_V \rho_m dV \quad (3.19)$$

$$\oiint_{S_c} \epsilon\mathbf{E} \cdot d\mathbf{S} = -\iiint_V \frac{\nabla \cdot \mathbf{J}}{j\omega} dV = \iiint_V \rho dV \quad (3.20)$$

where C is the contour bounding the open surface S illustrated in Figure 3.1 and $d\mathbf{S} = \hat{n}dS$. The circle through the single integral indicates integration over a closed contour, whereas the same symbol through the surface integral denotes integration over the closed surface S_c which enclosed the corresponding volume V . The surface S associated with the integrals (3.17) and (3.18) is completely unrelated to S_c that encloses the volume V .

Equations (3.13) and (3.14) imply six scalar equations for the solution of the six components connected with \mathbf{E} and \mathbf{H} . Thus, for time-harmonic fields, equations (3.13) and (3.14) or equations (3.17) and (3.18) are sufficient for the solution of the electric and magnetic fields.

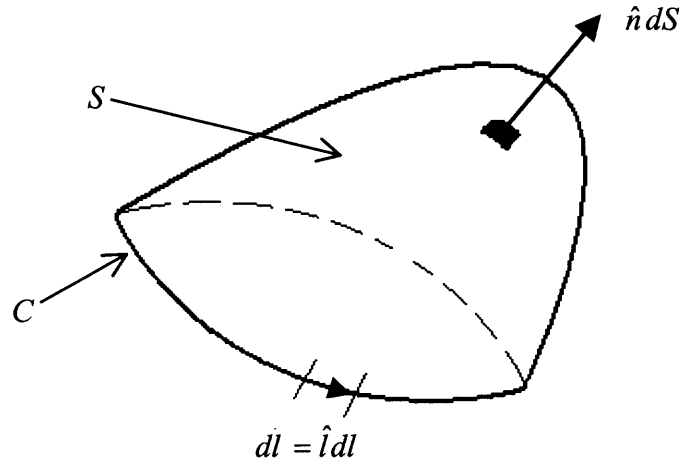


Figure 3.1 Illustration of the differential element ds and the contour C .

3.1.2 Wave Equation

Equations (3.13) and (3.14) are independent first-order vector equations, which lead to a unique solution subject to the specified boundary conditions. They may be combined together to produce a single second-order vector equation in terms of \mathbf{E} and \mathbf{H} as the wave equation. The finite element method is used to numerically approximate the solution of the wave equation.

The following vector wave equations are obtained by taking the curl of equations (3.13) and (3.14) and making use of other,

$$\nabla \times \left(\frac{\nabla \times \mathbf{E}}{\mu_r} \right) - k_o^2 \epsilon_r \mathbf{E} = -jk_o Z_o \mathbf{J} - \nabla \times \left(\frac{\mathbf{M}}{\mu_r} \right) \quad (3.21)$$

$$\nabla \times \left(\frac{\nabla \times \mathbf{H}}{\epsilon_r} \right) - k_o^2 \mu_r \mathbf{H} = -jk_o Y_o \mathbf{M} + \nabla \times \left(\frac{\mathbf{J}}{\epsilon_r} \right) \quad (3.22)$$

where the upper set of equations are the solution of the electric field while the lower set is for the solution of the magnetic field. In the equations, ϵ_r denotes the relative permittivity of the media and μ_r indicates the relative permeability of the media. These two quantities are unity for free space. Also, $Z_o = 1/Y_o = \sqrt{\mu_o/\epsilon_o}$ is the free space wave impedance. In materials other than free space, the wave impedance and the wave number are given by $Z = 1/Y = \sqrt{\mu/\epsilon}$ and $k = \omega\sqrt{\epsilon\mu}$, respectively.

By using the vector identity of $\nabla \times (\phi \mathbf{A}) = \nabla \phi \times \mathbf{A} + \phi \nabla \times \mathbf{A}$, equations (3.21) and (3.22) can be written in the form

$$\left(\frac{1}{\mu_r}\right) \nabla \times \nabla \times \mathbf{E} - k_o^2 \epsilon_r \mathbf{E} + \left[\nabla \left(\frac{1}{\mu_r}\right) \times \nabla \times \mathbf{E} \right] = -jk_o Z_o \mathbf{J} - \nabla \times \left(\frac{\mathbf{M}}{\mu_r}\right) \quad (3.23)$$

$$\left(\frac{1}{\epsilon_r}\right) \nabla \times \nabla \times \mathbf{H} - k_o^2 \mu_r \mathbf{H} + \left[\nabla \left(\frac{1}{\epsilon_r}\right) \times \nabla \times \mathbf{H} \right] = -jk_o Y_o \mathbf{M} + \nabla \times \left(\frac{\mathbf{J}}{\epsilon_r}\right) \quad (3.24)$$

Most implementations of the finite element method assume a homogeneous media within each finite element, hence the terms $\nabla \left(\frac{1}{\mu_r}\right)$ and $\nabla \left(\frac{1}{\epsilon_r}\right)$ can be set to zero.

By using an identity of $\nabla \times \nabla \times \mathbf{E} = \nabla \nabla \cdot \mathbf{E} - \nabla^2 \mathbf{E}$, the equation (3.23) can be arranged into a more important version for homogeneous media, i.e.

$$-\nabla(\nabla \cdot \mathbf{E}) + \nabla^2 \mathbf{E} + k_o^2 \epsilon_r \mu_r \mathbf{E} = jk_o Z_o \mu_r \mathbf{J} + \nabla \times \mathbf{M} \quad (3.25)$$

This equation can be simplified to

$$\nabla^2 \mathbf{E} + k^2 \mathbf{E} = 0 \quad (3.26)$$

in a source-free region, where $k = k_o \sqrt{\mu_r \varepsilon_r}$. Vector equation of (3.26) represents three field components each of which satisfies the scalar wave equation

$$\nabla^2 \psi + k^2 \psi = 0 \quad (3.27)$$

where ψ denotes E_x , E_y , or E_z . Similar equations can be obtained for the magnetic field from equation (3.24).

3.2 Finite Element Method

FEM geometrical adaptability and low memory requirements have made it one of the most popular numerical methods in all branches of engineering. Its application to boundary value problems⁴¹ involves the subdivision of the region where the fields are to be determined into smaller elements.³⁹ The subdivision of the domain into small elements is defined as meshing. It is also called discretization of the geometry and it is an important step in FEM solution procedure. In the context of the FEM, the equation for the unknown coefficients of the expansions is constructed by enforcing the wave equation in a weighted sense over each element. The next step involves the application of the boundary conditions leading to a secular matrix system.

$$[A]\{x\}=\{b\} \quad (3.28)$$

where $\{b\}$ is a column matrix and is determined on the basis of the boundary conditions, such as a current source or incident field, for each specific problem. The matrix $[A]$ is a square matrix, $N \times N$, typically symmetric unless nonreciprocal material exists in the computational domain. Its nonzero entries provide the relationship among fields of adjacent elements within the computational domain and its specific form is a characteristic of the problem geometry and discretization of the domain. With the system

equation constructed, its solution can be solved with the application of an iterative solver for large systems, since these solver avoid explicit storage of the entire matrix, or direct solver (LU decomposition) for smaller size system.

Suitable interpolation polynomials, commonly referred to as shape functions or basis functions, are used to approximate the unknown function within each element. Once these shape or basis functions are chosen, it is possible to compute and program the microprocessor to solve complicated geometries by solely specifying the shape or basis functions. The development of a unique element, which mimics the character of electric and magnetic fields, has proved to be the key in obtaining robust solutions to the two dimensional waveguides problems in electromagnetics.

In node based finite element, the form of the sought function in the element is controlled by the function values at its node. The approximating function can then be expressed as a linear combination of basis functions weighted by the nodal coefficients. If the function values u_i^e at the nodes are taken as nodal variables, then the approximating function for a two dimensional element e with p nodes has the form of

$$u^e(x, y) = \sum_{i=1}^p u_i^e N_i^e(x, y) \quad (3.29)$$

Since the equation (3.29) must be valid for any modal variable u_i^e , the basis function $N_i^e(x, y)$ must be unity at node i , and zero for all remaining nodes within the elements.

The FEM steps involved in generation and solution are as summarized below;

1. Define the problem's computational domain.
2. Select a mesh truncation scheme.
3. Select shape or basis functions and discrete elements.

4. Generate the mesh.
5. Enforce Maxwell wave equations over each element.
6. Generate the elemental matrix.
7. Apply boundary condition, either Neumann or Dirichlet BCs.
8. Assemble element matrices into global matrix.
9. Ensure matrix symmetry.
10. Select solver and solve matrix system.
11. Post-process field data to extract parameters of interest, i.e eigenvalues, fields, propagation constant, impedance, etc.

3.3 One-Dimensional FEM

One-dimensional finite elements are employed for solving problems where the discretization domain involves a curve or a contour around a two dimensional structure; for example the bounding curve of the cross section of an infinite cylinder. These basis functions can also be used in conjunction with higher dimensional finite elements when the modeled structure can be decomposed into a single dimension without loss of accuracy. It is most convenient to derive one-dimensional basis functions in terms of Lagrange polynomials.⁴² By considering a straight line with endpoints x_1^e and x_2^e . The basis functions for element e are then defined as

$$N_1^e(x) = \frac{x_2^e - x}{x_2^e - x_1^e} \quad (3.30)$$

$$N_2^e(x) = \frac{x - x_1^e}{x_2^e - x_1^e} \quad (3.31)$$

The basis functions have unit magnitude at one node and vanish at all others with linear variation between the nodes.

The solution of the one-dimensional differential equation⁴¹ is

$$-\frac{d}{dx}\left(p(x)\frac{dU(x)}{dx}\right) + q(x)U(x) = f(x) \quad 0 < x < x' \quad (3.32)$$

where $p(x)$, $q(x)$ and $f(x)$ are the known functions and $U(x)$ is the unknown field. This equation can be represented as different problems, depending on the interpretation of $U(x)$ given below as examples.

For an electric field between parallel plates of a capacitor,

$$U(x) = E_y(x); \text{ electric field between plates}$$

The boundary conditions are

$$E_y(0) = E_y(x') = 0;$$

$$p(x) = -1/\mu_r;$$

$$q(x) = k_o^2 \epsilon_r;$$

$$f(x) = \text{source function}$$

hence,

$$-\frac{d}{dx}\left(\frac{1}{\mu_r}\frac{d}{dx}E_y\right) + k_o^2 \epsilon_r E_y = f(x) \quad (3.33)$$

For the potential of a parallel plate capacitor,

$$U(x) = V(x); \text{ potential between plates.}$$

Boundary conditions:

$$V(0) = 0, V(x') = V';$$

$$p(x) = -1;$$

$$q(x) = 0;$$

$$f(x) = -\rho/\varepsilon, \text{ source function}$$

then,

$$\frac{d}{dx} \left(\frac{d}{dx} V(x) \right) = -\frac{\rho}{\varepsilon} \quad (3.34)$$

Appendix C lists the FEM program that illustrated the FEM application of various steps in constructing, assembling and solving the one-dimensional system. The FEM system is solved using 10 linear elements. The differential equation is also subjected to the following boundary conditions.

$$E_y(x=0) = E_y(x=1) = 0 \quad (3.35)$$

By comparison to the general form of the differential equation (3.2), the coefficients are;

$$\begin{aligned} p(x) &= 1 \\ q(x) &= \pi^2 \\ f(x) &= 2\pi^2 \sin(\pi x) \end{aligned} \quad (3.36)$$

The FEM results obtained from solving the eigenvalue equations in the matrix were also compared with the exact analytical solution, i.e. $E_y(x) = \sin(\pi x)$ and are tabulated in Table 3.1. From the table, it is observed that the difference between the exact and the numerical solution is in the third decimal place, indicating that the employed number of element are sufficient for an accurate representation of the field distribution.

3.4 Two-Dimensional FEM

Two-dimensional finite elements have found widespread use in modeling structures whose third dimension is significantly larger or smaller than the cross section, thus ensuring little variation in the unknown parameters in the third direction. Two-dimensional finite elements have also been used to obtain reliable estimates of three-

dimensional problems since the computational cost for obtaining two-dimensional solutions is vastly less expensive than for three dimensions. There are several types of shape function available for two-dimensional FEM analysis, namely rectangular, quadrilateral, and triangular elements shape function.

Table 3.1 One-dimensional FEM solution with exact analytical solution

Node location	E_y^{FEM} 10 elements	E_y^{EXACT}
1	0	0
2	0.3077	0.3090
3	0.5854	0.5878
4	0.8057	0.8090
5	0.9471	0.9511
6	0.9959	1.0
7	0.9471	0.9511
8	0.8057	0.8090
9	0.5854	0.5878
10	0.3077	0.3090
11	0	0

3.4.1 Two-Dimensional Basis Functions

The triangular elements are selected to be the basis function of the waveguide problems. Triangular elements are chosen because they are most versatile and can model arbitrary geometry profiles, comparing with other elements. The shape functions of the triangular elements are determined by using the Lagrange interpolation polynomials. In their final expression, the shape functions will be expressed in terms of the area coordinates. By considering, a point P within a triangular element shown in Figure 3.2 located at (x, y) , where (x_i^e, y_i^e) denote the coordinates of the i^{th} triangle node. The area of the smaller triangle formed by points P, 2, and 3 is given by

$$\Delta_1 = \frac{1}{2} \begin{vmatrix} 1 & x & y \\ 1 & x_2^e & y_2^e \\ 1 & x_3^e & y_3^e \end{vmatrix} \quad (3.37)$$

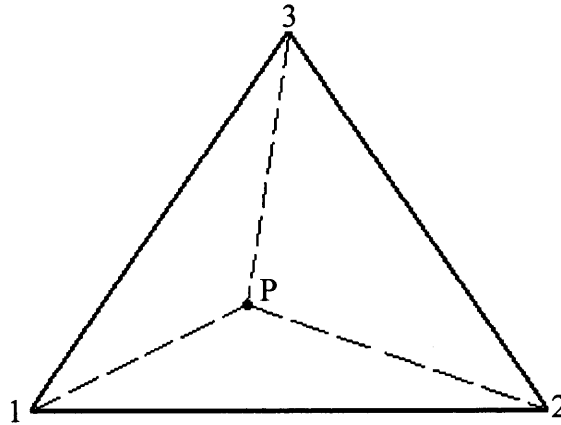


Figure 3.2 Triangular element.

The area coordinate L_i^e is then defined by

$$L_1^e = \frac{\Delta_1}{\Delta} = \frac{Area_P23}{Area_123} \quad (3.38)$$

where Δ is the area of the whole triangle and can be found from equation (3.37) by replacing x and y in the first row with x_1 and y_1 .

Similarly, the two remaining area coordinates L_2^e and L_3^e are given by

$$L_2^e = \frac{\Delta_2}{\Delta} = \frac{Area_P31}{Area_123} \quad (3.39)$$

$$L_3^e = \frac{\Delta_3}{\Delta} = \frac{Area_P12}{Area_123} \quad (3.40)$$

The values for x and y inside the triangle element reduce to

$$x = \sum_{i=1}^3 L_i^e x_i^e \quad (3.41)$$

$$y = \sum_{i=1}^3 L_i^e y_i^e \quad (3.42)$$

$$1 = \sum_{i=1}^{e=3} L_i \quad (3.43)$$

where equations (3.41)-(3.43) are a result of the area identity $\Delta_1 + \Delta_2 + \Delta_3 = \Delta$.

Alternatively, $L_{1,2,3}^e$ can be obtained in terms of x and y , and the vertex coordinates by solving the system equations (3.41)-(3.43).

The coordinate L_1^e is zero on the edge opposite to vertex 1 and unity at vertex 1. Its variation along the height of the triangle is displayed in Figure 3.3. The remaining two area coordinates associated with the other two vertices behave similarly, vanishing on the edge opposite to the corresponding vertex and having unit magnitude at the vertex it

belongs to. This feature combined with spatial locality qualifies the area coordinates as suitable basis functions N_i^e for a triangle when the interpolation order is linear. That is

$$N_i^e = L_i^e \quad (3.44)$$

Higher order basis functions for triangles can also be derived.^{42,43}

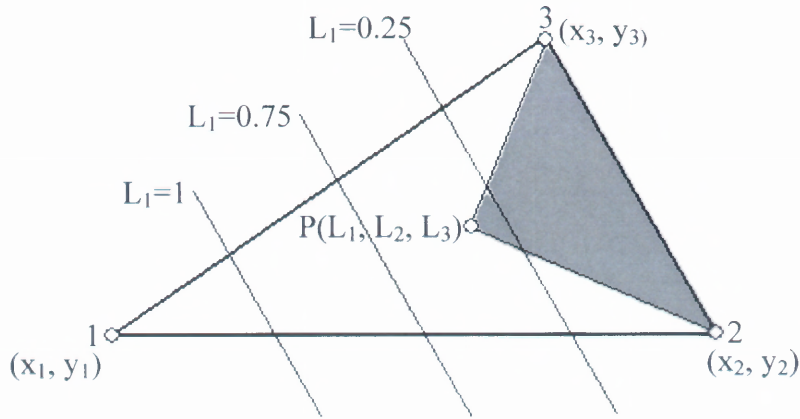


Figure 3.3 Area coordinates of a triangle.

3.4.2 Two-Dimensional Wave Equation

The electric and magnetic fields in waveguide propagation is assumed to be in the form

$$\mathbf{E} = \mathbf{U}_e(x, y)e^{-j\beta z} \quad (3.45)$$

$$\mathbf{H} = \mathbf{U}_h(x, y)e^{-j\beta z} \quad (3.46)$$

where β is the propagation constant along z and $\mathbf{U}(x, y)$ is the field value over the waveguide cross section, the subscripts of e and h represent the electric and magnetic fields, respectively. Recall from Section 3.1.2, the vector wave equations for the electric and magnetic fields are

$$\nabla^2 \mathbf{E} + k^2 \mathbf{E} = 0 \quad (3.47)$$

$$\nabla^2 \mathbf{H} + k^2 \mathbf{H} = 0 \quad (3.48)$$

These equations allow a decoupling of the differential equation among the field components provided that $\nabla^2 \mathbf{H} = \hat{x}\nabla^2 H_x + \hat{y}\nabla^2 H_y + \hat{z}\nabla^2 H_z$. Thus only the scalar wave equation needed to be solved for TE modes ($H_z \neq 0$, $E_z = 0$). By setting

$\frac{\partial^2 H_z}{\partial z^2} = -\beta^2 H_z$ the scalar wave equation is defined as

$$\nabla_t^2 H_z + (k^2 - \beta^2) H_z = 0 \quad (3.49)$$

where ∇_t denotes the surface gradient. Once the E_z is determined from equation (3.49), other field components can be obtained by using the expressions

$$E_y = \left(\frac{j\omega\mu}{\gamma^2} \right) \left(\frac{\partial H_z}{\partial x} \right) \quad (3.50)$$

$$E_x = - \left(\frac{j\omega\mu}{\gamma^2} \right) \left(\frac{\partial H_z}{\partial y} \right) \quad (3.51)$$

$$H_x = - \left(\frac{j\beta}{\gamma^2} \right) \left(\frac{\partial H_z}{\partial x} \right) \quad (3.52)$$

$$H_y = - \left(\frac{j\beta}{\gamma^2} \right) \left(\frac{\partial H_z}{\partial y} \right) \quad (3.53)$$

where $\gamma^2 = \sqrt{k^2 - \beta^2}$ is the wavenumber. Alternatively, the vector wave equation can also be solved,

$$\nabla_t \times \left(\frac{1}{\mu_r} \nabla_t \times \mathbf{E}_t \right) - \left(k_o^2 \epsilon_r - \frac{\beta^2}{\mu_r} \right) \mathbf{E}_t = 0 \quad (3.54)$$

in which

$$\mathbf{E}_t = \hat{x}E_x + \hat{y}E_y \quad (3.55)$$

is the total transverse electric field in the waveguide.

On the other hand, for the TM modes where $H_z = 0$ while $E_z \neq 0$, the appropriate scalar and vector wave equations are simply the duals of equations (3.49)-(3.55). However, the boundary conditions used are the Dirichlet type when solving for E_z and of the Neumann type when solving for H_z . The relation $\partial H_z / \partial n = 0$ serves as the boundary condition for the TE case.

3.4.3 Discretization of the Two-Dimensional Wave Equation

From the above presentation, a general form of the two-dimensional wave equation is

$$\nabla \cdot [p(x, y) \nabla U(x, y)] + k_o^2 q(x, y) U(x, y) = f(x, y) \quad (3.56)$$

where $\nabla = \nabla_t = \hat{x} \partial / \partial x + \hat{y} \partial / \partial y$. The equation can be specialized to the problems of scattering and waveguide propagation by choosing $p(x, y)$ and $q(x, y)$ appropriately. When TE mode is considered,

$$U(x, y) = H_z(x, y), \quad p(x, y) = \frac{1}{\varepsilon_r}, \quad q(x, y) = \mu_r$$

while for TM mode,

$$U(x, y) = E_z(x, y), \quad p(x, y) = \frac{1}{\mu_r}, \quad q(x, y) = \varepsilon_r$$

The steps to be followed for the solution of equation (3.59) via the FEM involve

1. Casting of the original wave equation to its *weak* form to obtain a single functional incorporating the conditions imposed by the wave equation and the boundary conditions.

2. Meshing of the computational domain allowing for a discretization of the *weak* form to a linear system of equations element by element.
3. Assembly of the element equation and imposition of the boundary conditions to attain the final linear system of equations.

In this section, the first two steps are discussed, and in the subsequent section the assembly of the elemental equations are considered to solve for the fields and eigenvalue associated with a metallic waveguide (closed domain problem).

3.4.3.1 Weak Form of the Wave Equation. In electrodynamics, the *weak* form of wave equation represents the scalar wave equation. The related residual of equation (3.56) is

$$R(x, y) = \nabla \cdot p(\mathbf{r}) \nabla U(\mathbf{r}) + k_o^2 q(\mathbf{r}) U(\mathbf{r}) - f(\mathbf{r}) \quad (3.57)$$

where as usual $\mathbf{r} = x\hat{x} + y\hat{y}$ denotes the position vector. The weak form of wave equation is derived from multiplying equation (3.60) by a weighting function $W(x, y)$ and enforce $R(\mathbf{r}) = 0$ over the domain of each element. This gives

$$\iint_{\substack{\text{Domain} \\ \text{of } W(r)}} W(\mathbf{r}) R(\mathbf{r}) dx dy = 0 \quad (3.58)$$

The weighting function must be compatible with the boundary conditions. To reduce the order of the derivatives in the residual and introduce the boundary terms, the identities below are used,

$$W \nabla \cdot p \nabla U = \nabla \cdot (p W \nabla U) - p \nabla W \cdot \nabla U \quad (3.59)$$

$$\iint_{\Omega} \nabla \cdot (p W \nabla U) ds = \oint_C p W (\nabla U \cdot \hat{n}) dl \quad (3.60)$$

in which Ω denotes the pertinent computational domain, C is the contour enclosed Ω , and \hat{n} refers to the outward directed unit normal vector to the contour C . Equation (3.60) is the divergence theorem, which can be considered as the generalization of integration by parts to two dimensions.

Substituting equations (3.62) and (3.63) into the weighting residual equation (3.61) yields

$$\iint_{\Omega} \left[-p(\mathbf{r}) \nabla W(\mathbf{r}) \cdot \nabla U(\mathbf{r}) + k_0^2 q(\mathbf{r}) W(\mathbf{r}) U(\mathbf{r}) - W(\mathbf{r}) f(\mathbf{r}) \right] ds + \oint_C p(\mathbf{r}) W(\mathbf{r}) [\hat{n} \cdot \nabla U(\mathbf{r})] dl = 0 \quad (3.61)$$

This is the *weak* form of the two-dimensional scalar wave equation. Note that the presence of the boundary integral over C allows for the imposition of the boundary conditions. Thus equation (3.61) provides a single statement incorporating the conditions implied by the wave equation and the pertinent boundary conditions, and this is at the heart of the finite element method.

3.4.3.2 Discretization of the Weak Wave Equation. To discretize equation (3.61), a discrete representation of the field $U(x,y)$ is introduced together with the proper choices for the weighting function $W(x,y)$. At first, the computational domain Ω is divided into small triangular elements. Then, by approximating the field in each triangle as a linear function, the expansion of basis function $N_i^e(x,y)$, as given in Section 3.4.1, can be chosen to represent $U(x,y)$ over Ω . Specifically, $U(x,y)$ can be expand into

$$U(x,y) = \sum_{e=1}^{N_e} \sum_{i=1}^3 U_i^e N_i^e(x,y) \quad (3.62)$$

where U_i^e are the unknown coefficients of the expansion and represent the field or potential values at the nodes of each triangle. This representation is therefore referred to as a node-based expansion. N_e is the number of elements used for meshing the domain.

The explicit form of the shape function is

$$N_i^e(x, y) = \begin{cases} \left(\frac{1}{2\Delta^e} \right) (a_i^e + b_i^e x + c_i^e y) & \mathbf{r} \in \Omega^e \\ 0 & \text{otherwise} \end{cases} \quad (3.63)$$

where

$$\Delta^e = \frac{1}{2} \det \begin{bmatrix} 1 & x_1^e & y_1^e \\ 1 & x_2^e & y_2^e \\ 1 & x_3^e & y_3^e \end{bmatrix} = \frac{1}{2} [(x_2^e - x_1^e)(y_3^e - y_1^e) - (x_3^e - x_1^e)(y_2^e - y_1^e)] \quad (3.64)$$

is the triangle area. The coefficients in equation (3.63) are given by

$$a_i^e = x_j^e y_k^e - x_k^e y_j^e, \quad b_i^e = y_j^e - y_k^e, \quad c_i^e = x_k^e - x_j^e \quad (3.65)$$

with the indices (i, j, k) following the cyclical rule. The shape functions $N_i^e(x, y)$ are equal to unity at the i^{th} node of the e^{th} element and taper linearly to zero at the other two nodes, as illustrated in Figure 3.4. Consequently, the e^{th} element expansion $\sum_{i=1}^3 U_i^e N_i^e(x, y)$ scales the shape functions depending on the value of the field or potential at the nodes of the e^{th} element.

Substituting equation (3.62) into equation (3.61) yields

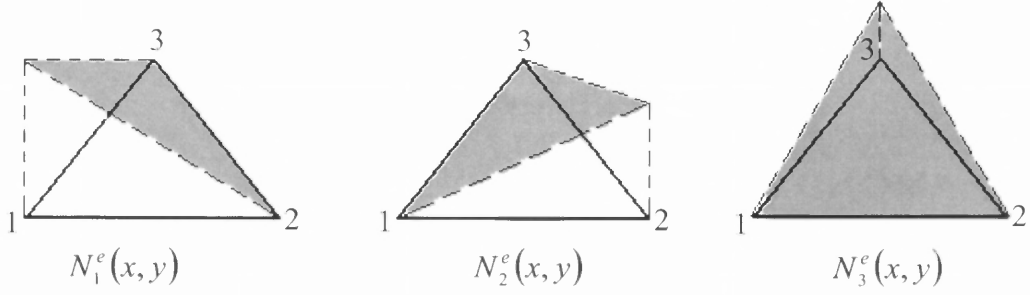


Figure 3.4 Node coordinates for the e^{th} triangle and illustration of the node-based expansion function $N_i^e(x, y)$.

$$\sum_{e=1}^{N_e} \sum_{i=1}^3 U_i^e \iint_{\Omega^e} \left[-p(\mathbf{r}) \nabla W(\mathbf{r}) \cdot \nabla N_i^e(\mathbf{r}) + k_0^2 q(\mathbf{r}) W(\mathbf{r}) N_i^e(\mathbf{r}) \right] dx dy + \int_C p(\mathbf{r}) W(\mathbf{r}) \hat{n} \cdot \nabla U(\mathbf{r}) dl = \iint_{\Omega^e} W(\mathbf{r}) f(\mathbf{r}) dx dy \quad (3.66)$$

A linear set of equations can be obtained by employing Galerkin's method where the weighting function $W(x, y)$ is chosen so that it is equal to the expansion basis function $N_i^e(x, y)$, $i = 1, 2, 3$. This yields

$$\sum_{i=1}^3 U_i^e \iint_{\Omega^e} \left[-p(\mathbf{r}) \nabla N_j^e(\mathbf{r}) \cdot \nabla N_i^e(\mathbf{r}) + k_0^2 q(\mathbf{r}) N_j^e(\mathbf{r}) N_i^e(\mathbf{r}) \right] dx dy + \int_C p(\mathbf{r}) N_j^e(\mathbf{r}) \hat{n} \cdot \nabla U(\mathbf{r}) dl = \iint_{\Omega^e} N_j^e(\mathbf{r}) f(\mathbf{r}) dx dy \quad j = 1, 2, 3 \quad (3.67)$$

From equation (3.67), a 3×3 system of equations can be obtained by running through all choices of $j = 1, 2, 3$ if the Neumann boundary condition $\hat{n} \cdot \nabla U = \partial U / \partial n = 0$ is assumed,

$$\begin{bmatrix} A_{11}^e & A_{12}^e & A_{13}^e \\ A_{21}^e & A_{22}^e & A_{32}^e \\ A_{31}^e & A_{32}^e & A_{33}^e \end{bmatrix} \begin{Bmatrix} U_1^e \\ U_2^e \\ U_{31}^e \end{Bmatrix} = \begin{Bmatrix} b_1^e \\ b_2^e \\ b_3^e \end{Bmatrix} \quad (3.68)$$

or

$$[A^e] \{U^e\} = \{b^e\}$$

which is the element matrix system. The explicit form of the matrix entries is

$$\begin{aligned} A_{ij}^e = & -p^e \iint_{\Omega^e} \nabla N_i^e(\mathbf{r}) \cdot \nabla N_j^e(\mathbf{r}) dx dy \\ & + k_o^2 q^e \iint_{\Omega^e} N_i^e(\mathbf{r}) N_j^e(\mathbf{r}) dx dy \quad i = 1, 2, 3 \quad j = 1, 2, 3 \end{aligned} \quad (3.69)$$

$$b_j^e = \iint_{\Omega^e} N_j^e(\mathbf{r}) f(\mathbf{r}) dx dy \quad j = 1, 2, 3 \quad (3.70)$$

where $p(\mathbf{r}) \approx p^e$ and $q(\mathbf{r}) \approx q^e$ are constant over each element. Since $N_i^e(\mathbf{r})$ are linear

functions, the evaluation of the $[A^e]$ matrix entries can be done in closed form,

$$[A^e] = [K_{\nabla}^e] + k_o^2 [K^e] \quad (3.71)$$

where

$$\begin{aligned} [K_{\nabla}^e] &= \left[-p^e \iint_{\Omega^e} \nabla N_i^e \cdot \nabla N_j^e dx dy \right] \\ &= -p^e \left[\iint_{\Omega^e} \left\{ \frac{\partial N_i^e}{\partial x} \right\} \left\{ \frac{\partial N_j^e}{\partial x} \right\}^T dx dy + \iint_{\Omega^e} \left\{ \frac{\partial N_i^e}{\partial y} \right\} \left\{ \frac{\partial N_j^e}{\partial y} \right\}^T dx dy \right] \end{aligned}$$

$$[K^e] = \left[q^e \iint_{\Omega^e} N_i^e N_j^e dx dy \right] = q^e \iint_{\Omega^e} \{N_i^e\} \{N_j^e\}^T dx dy$$

Evaluating the entries of the submatrices $[K_{\nabla}^e]$ and $[K^e]$ yields

$$\left[\iint_{\Omega^e} \nabla N_i^e \cdot \nabla N_j^e dx dy \right] = \frac{1}{4\Delta^e} \begin{bmatrix} (b_1^e)^2 + (c_1^e)^2 & b_1^e b_2^e + c_1^e c_2^e & b_1^e b_3^e + c_1^e c_3^e \\ b_2^e b_1^e + c_2^e c_1^e & (b_2^e)^2 + (c_2^e)^2 & b_2^e b_3^e + c_2^e c_3^e \\ b_3^e b_1^e + c_3^e c_1^e & b_3^e b_2^e + c_3^e c_2^e & (b_3^e)^2 + (c_3^e)^2 \end{bmatrix} \quad (3.72)$$

$$\left[\iint_{\Omega^e} N_i^e N_j^e dx dy \right] = \frac{\Delta^e}{12} \begin{bmatrix} 2 & 1 & 1 \\ 1 & 2 & 1 \\ 1 & 1 & 2 \end{bmatrix} \quad (3.73)$$

The latter is independent of the triangle coordinates and is referred to as a universal element matrix.⁴⁴ By making use of equations (3.73) and (3.76) in equation (3.72), the $[A^e]$ matrix entries can be more compactly written as

$$A_{ij}^e = K_{\nabla_{ij}}^e + k_o^2 K_{ij}^e = \left[\frac{-P^e}{4\Delta^e} (b_i^e b_j^e + c_i^e c_j^e) \right] + k_o^2 \left[\frac{q^e \Delta^e}{12} (1 + \delta_{ij}) \right] \quad (3.74)$$

where

$$\delta_{ij} = \begin{cases} 1 & i = j \\ 0 & \text{otherwise} \end{cases}$$

Thus, for the chosen linear triangular elements, the matrix entries are given in closed form and can be easily evaluated. The excitation column entries b_j^e may need to be computed numerically depending on the form of the function $f(x,y)$.

3.4.3.3 Assembly of Element Equations. The first step in the finite element procedure is the assembly of the element equation (3.68). This involves the procedure of carrying out the sum

$$\sum_{e=1}^{N_e} [A^e] \{U^e\} = \sum_{e=1}^{N_e} \{b^e\} \quad (3.75)$$

as implied by the original discrete form of the weak wave equation (3.66). Since several of the elements may share the same nodes, the sum of equation (3.75) consolidate the surrounding element to yield a single equation, which produces the equation

$$\left(\sum_{i=0}^4 A_{11}^{e'+i} \right) U_1^{e'} + \sum_{i=0}^4 \left(A_{12}^{e'+i} U_2^{e'+i} + A_{13}^{e'+i} U_3^{e'+i} \right) = \sum_{i=0}^4 b_1^{e'+i} \quad (3.76)$$

A key issue in performing the assembly as dictated by equation (3.75) is the transformation from local to global nodes. The issue of node numbering becomes apparent by looking at the assembled equation (3.76).

Since the unknowns U_i^e must be eventually put into a single column, it is necessary to have readily available mapping between the local and global nodes, which are associated with the e^{th} element. Thus, in addition to the node geometry data provided to the finite element program, the information about the local and global node numbering schemes are also provided. Four tables may be required before carrying out the matrix assembly routine, as in Appendix B.

3.4.3.4 Assembled Eigenvalue Matrix. Considered an 18-element rectangular waveguide cross section as shown in Figure 3.5 with the elements connectivity and nodes location tables given in Appendix B. Assume that $U = H_z$, then $\partial U / \partial n = \hat{n} \cdot \nabla U = 0$ at the boundary nodes of the rectangular waveguide. Thus, the boundary integral in equation (3.67) vanishes and the FEM system for the node fields is obtained by performing the assembly

$$\sum_{e=1}^{18} [A^e] \{U^e\} = [A] \{U\} = 0 \quad (3.77)$$

where the dimension of $\{U\}$ is 16 and $\{b^e\}$ was set to zero since no excitation is assumed.

A procedure for carrying out the assembly is as follow:

Note the correspondence between the local and global nodes, for example, $U_1^{e=10} = U_6$.

The single subscript refers to the global node 6, thus the element matrix for $e = 10$ is

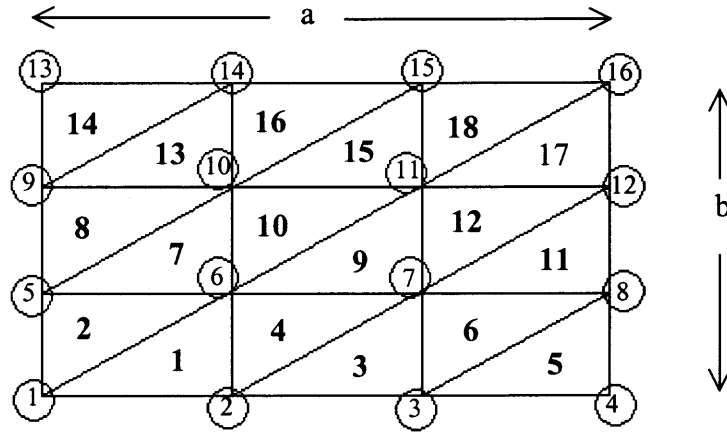


Figure 3.5 Element geometry for matrix assembly.

$$\begin{bmatrix} A_{11}^{10} & A_{12}^{10} & A_{13}^{10} \\ A_{21}^{10} & A_{22}^{10} & A_{23}^{10} \\ A_{31}^{10} & A_{32}^{10} & A_{33}^{10} \end{bmatrix} \begin{Bmatrix} U_6 \\ U_{11} \\ U_{10} \end{Bmatrix} = 0 \quad (3.78)$$

To obtain the assembled equation for global node 6, the element sharing this node must be considered as well. In addition to element 10, node 6 is shared by element 1, 2, 4, 9, and 7. The corresponding element matrix for element 1 is

$$\begin{bmatrix} A_{11}^2 & A_{12}^2 & A_{13}^2 \\ A_{21}^2 & A_{22}^2 & A_{23}^2 \\ A_{31}^2 & A_{32}^2 & A_{33}^2 \end{bmatrix} \begin{Bmatrix} U_1 \\ U_2 \\ U_6 \end{Bmatrix} = 0 \quad (3.79)$$

and similar matrixes applied to other shared elements with the same form of (3.78) and (3.79). Adding the two of the seven local elements contributions related to the global node number 6 yields the global system matrix

$$\begin{bmatrix}
A_{11}^1 & A_{12}^1 & \cdot & A_{13}^1 & \cdot & \cdot & \cdot \\
A_{21}^1 & A_{22}^1 & \cdot & A_{23}^1 & \cdot & \cdot & \cdot \\
\cdot & \cdot & \cdot & \cdot & \cdot & \cdot & \cdot \\
A_{31}^1 & A_{32}^1 & \cdot & A_{33}^1 + A_{11}^{10} & \cdot & A_{13}^{10} & A_{12}^{10} \\
\cdot & \cdot & \cdot & \cdot & \cdot & \cdot & \cdot \\
\cdot & \cdot & \cdot & A_{31}^{10} & \cdot & A_{33}^{10} & A_{32}^{10} \\
\cdot & \cdot & \cdot & A_{21}^{10} & \cdot & A_{23}^{10} & A_{22}^{10}
\end{bmatrix} \times \begin{Bmatrix} U_1 \\ U_2 \\ U_5 \\ U_6 \\ U_7 \\ U_{10} \\ U_{11} \end{Bmatrix} \quad (3.80)$$

The element matrixes can be assembled into the above system until all of the elements have been accounted for. The entries will be given by the sum

$$A_{n',m'} = \sum A_{ij}^{e_1}, \quad \text{for all } n(i, e_1) = n', \quad n(j, e_1) = m' \quad (3.81)$$

A computer program written in Matlab routine for performing the assembly is given in the Appendix D.

3.4.3.5 TE Modes (Neuman Boundary Conditions). A situation where both submatrices $[K_\nabla]$ and $[K]$, which obtained from the assembly of $[K_\nabla^e]$ and $[K^e]$ given in equation (3.74), are used is that of computing the waveguide cutoff wavenumbers. The cutoff wavenumbers are obtained by solving the generalized eigenvalue problem

$$-[K_\nabla]\{H_z\} = \gamma^2 [K]\{H_z\} \quad (3.82)$$

where γ^2 are the eigenvalues and γ refer to the cutoff wavenumbers. The Neumann boundary conditions (i.e. the natural boundary condition) is already embedded in the FEM matrix formulation, as discussed in Section 3.4.3.2. In the TE mode case, the H_z field is continuous across the boundary, i.e.

$$\hat{n} \cdot \nabla U = \frac{\partial U}{\partial n} = 0 \quad (3.83)$$

Table 3.2 Cutoff wavenumbers for a rectangular waveguide

TE	TM	Exact Analytical Solution γ	FEM 400 elements (IBM Mainframe)	FEM 200 elements (Intel Pent. II 650Mhz)
10		2.0946	2.0960	2.1030
20		4.1900	4.2053	4.2057
01		4.1900	4.2053	4.2573
11	11	4.6840	4.6848	4.7399
12	12	8.6386	8.8000	8.8463
21	21	5.9260	5.9953	6.1032

Consider the rectangular waveguide as depicted in Figure 3.5 with dimensions $a/b = 2$, the computed eigenvalues are given in Table 3.2 and the corresponding mode field distributions are shown in Figure 3.6 for the TE_{10} mode, using 400 triangular⁴⁵ elements over the waveguide cross section. From the table, they are within 0.4% of the exact eigenvalues⁴⁰ given by

$$\gamma = \sqrt{\left(\frac{m\pi}{a}\right)^2 + \left(\frac{n\pi}{b}\right)^2} \quad (3.84)$$

and also around 0.4% for 200 triangular elements computed using the FEM program listed in Appendix D, for the TE_{mn} ($m \neq 0$ or $n \neq 0$) and the TM_{mn} ($m \neq 0$ and $n \neq 0$) modes. The accuracy of the calculated eigenvalues deteriorates for the higher order modes since the latter require a finer meshing due to their more complex mode structure.

In the event that an analytic solution is not available to test the accuracy of the FEM results, an alternative is to use convergence studies. In this method, a parameter is calculated with increasing number of elements. If the calculated value of the parameter, such as γ above, approaches a constant value as the number of elements is increased, then FEM program code is functioning correctly assuming that the electromagnetic equations are correct.

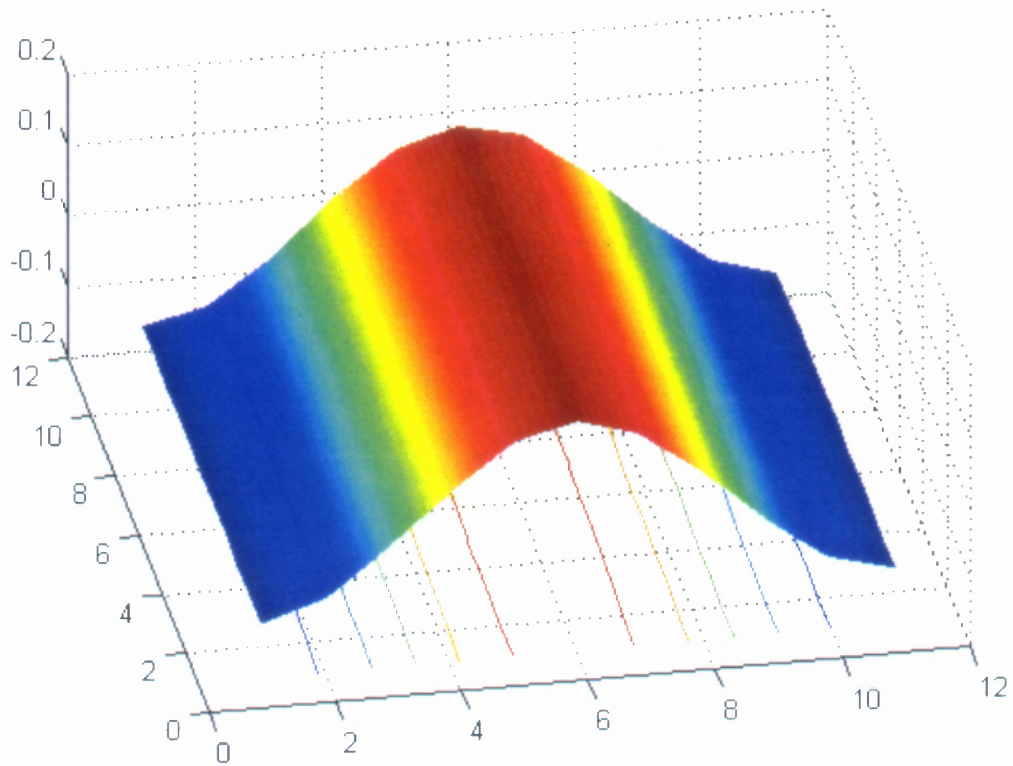


Figure 3.6 Calculated TE_{10} mode fields in a rectangular waveguide.

3.4.3.6 TM Modes (Dirichlet boundary Conditions). For the TM modes in a metallic rectangular waveguide, $U = E_z$ and $E_z = 0$ are set on the boundary. However,

$\frac{\partial U}{\partial n} = \hat{n} \cdot \nabla E_z = \frac{\partial E_z}{\partial n}$ is non-zero on the boundary and it is therefore necessary to

treat $\Psi = \partial E_z / \partial n$ as an additional unknown on the boundary. Since the field values at the boundary node are zero, it is not necessary to test at these nodes. Instead, the boundary nodes fields are set to zero whenever they appear in the system matrix. By avoiding testing at the boundary nodes or elements, the integrals over C_s do not enter in the construction of the final system and can be neglected altogether.

In this case, the eigenvalue problem becomes

$$-[K_{\nabla}']\{E_z\} = \gamma^2 [K']\{E_z\} \quad (3.85)$$

where $[K_{\nabla}']$ and $[K']$ are identical to those in solving the TE modes, except that only the entries associated with interior nodes are kept. Some values of the γ for the TM modes, obtained from solving equation (3.85) are given in Table 3.2 for the metallic rectangular waveguide. The FEM program is listed in Appendix D. Figure 3.7 displays the field of the lowest TM mode. The TM and TE modes fields calculated with FEM are compatible with the fields' solution shown in waveguide handbook.⁴⁶

3.5 Integrated MZI Single Waveguide Mode Solver

In this section, the integrated MZI waveguides TE and TM modes are solved by modifying the weak form of two-dimensional wave equation (3.71) into

$$\text{TE Mode:} \quad [K_{\nabla}] + \left(k_o^2 - \frac{\beta^2}{n_e^2} \right) [K] = 0 \quad (3.86)$$

$$\text{TM Mode:} \quad [K_{\nabla}] + (k_o^2 n_e^2 - \beta^2) [K] = 0 \quad (3.87)$$

where n_e refers to the refractive index of each element. The MZI waveguide profile consists of the refractive indices of the core, cladding, and the buffer layer. The refractive index of each element is proportional to ϵ_r , since $\mu_r = 1$ in most cases.

$$n_e^2 = \epsilon_r \mu_r = \epsilon_r \quad (3.88)$$

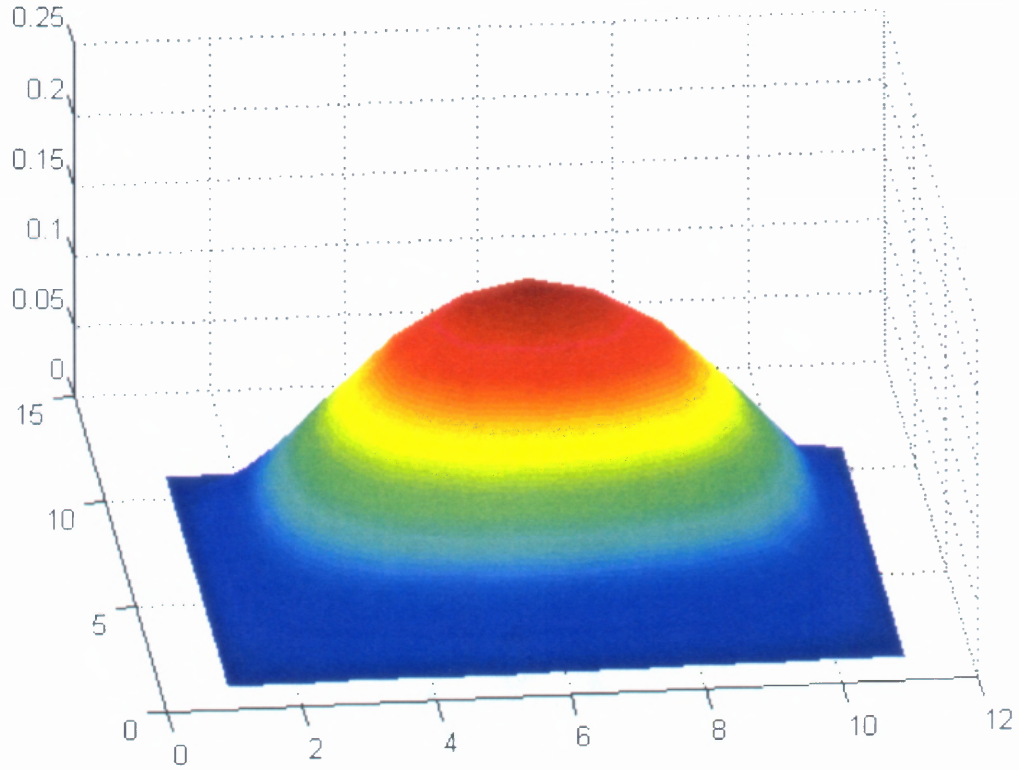


Figure 3.7 Calculated TM_{11} mode in a metallic rectangular waveguide.

By applying

$$v = k_o \sqrt{(n_{core}^2 - n_s^2)} \quad (3.89)$$

$$b = \frac{\left(\frac{\beta}{k}\right)^2 - n_s^2}{n_{core}^2 - n_s^2} \quad (3.90)$$

$$Q = \frac{n_e^2 - n_s^2}{n_{core}^2 - n_s^2} \quad (3.91)$$

where ν is the cutoff frequency, b refers to the normalized propagation constant, Q is the fictitious boundary profile, and n_s can be the cladding index or buffer layer index.

For TE mode, where

$$p_e = \frac{1}{\varepsilon_r}, \quad q_e = \mu_r$$

Equation (3.86) becomes

$$\begin{aligned} [K_{\nabla}] + \nu^2 \cdot \frac{1}{n_e^2} \cdot \left(\frac{n_e^2 - n_s^2}{n_{core}^2 - n_s^2} \right) \cdot [K] &= \frac{\nu^2}{n_e^2} \cdot b \cdot [K] \\ [K_{\nabla}] + \nu^2 \cdot p_e \cdot \left(\frac{1/p_e - n_s^2}{n_{core}^2 - n_s^2} \right) \cdot [K] &= \nu^2 \cdot p_e \cdot b \cdot [K] \end{aligned} \quad (3.92)$$

which simplified to

$$[A] = b[K'] \quad (3.93)$$

where $[A]$ is the sum of the two terms of the left hand side of equation (3.92) while

$[K'] = \nu^2 p_e [K]$ and b is the eigenvalue to be solved.

Similarly, for TM mode,

$$p_e = \frac{1}{\mu_r}, \quad q_e = \varepsilon_r$$

Equation (3.86) becomes

$$\begin{aligned} [K_{\nabla}] + \nu^2 \cdot \left(\frac{n_e^2 - n_s^2}{n_{core}^2 - n_s^2} \right) \cdot [K] &= \nu^2 \cdot b \cdot [K] \\ [K_{\nabla}] + \nu^2 \cdot \left(\frac{q_e - n_s^2}{n_{core}^2 - n_s^2} \right) \cdot [K] &= \nu^2 \cdot b \cdot [K] \end{aligned} \quad (3.94)$$

which simplified to

$$[A] = b[K'] \quad (3.95)$$

where $[A]$ is the sum of the two terms of the left hand side of equation (3.94) while

$[K'] = v^2[K]$ and b is the eigenvalue to be solved.

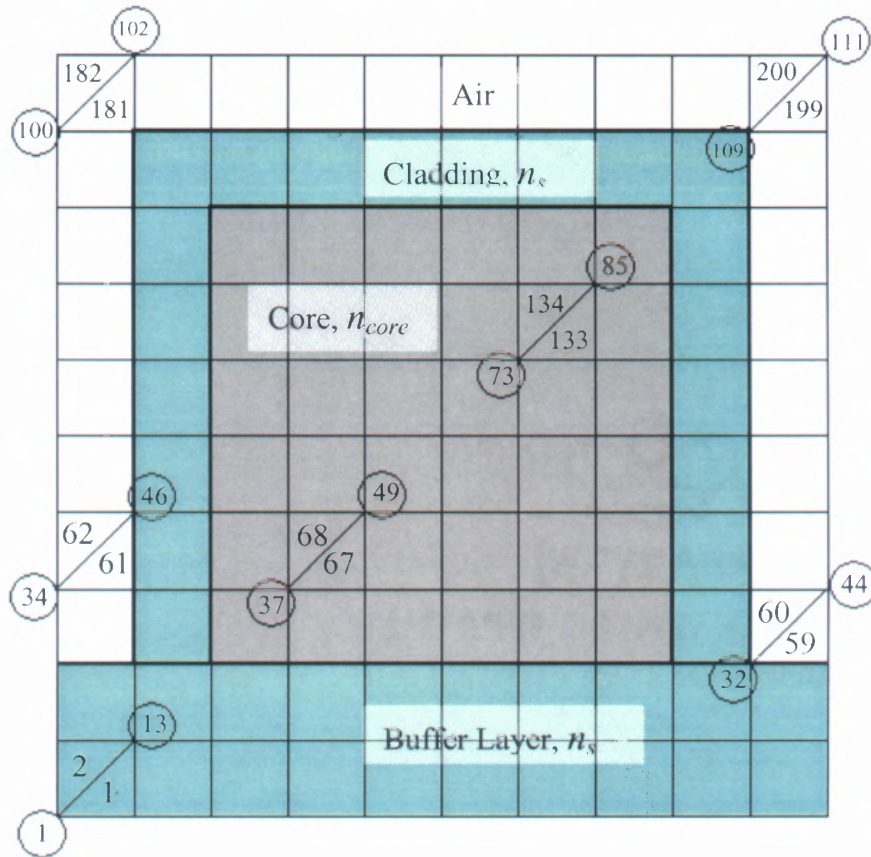


Figure 3.8 Refractive index profile of the MZI single waveguide with each element width of $1.0 \mu\text{m}$.

In order to simulate the waveguide modes for the integrated Mach-Zehnder Interferometer sensor; the finite element method required a mesh to be made to model the waveguide index of refraction profile. The 200 elements mesh profile of core, cladding

and the buffer layer is generated as shown in Figure 3.8. This FEM mesh profile generation program is listed in Appendix I, with user-defined number of elements. The mesh profile provides the fictitious boundary conditions of the step-index waveguide structure. The sampling arm mesh profile was generated by the same program listed in Appendix I, with the cladding index replaced by the air or chemical index of refraction. The refractive index profile of the sampling arm is as shown in Figure 3.9. The corresponding FEM programs to solved both the TM and TE modes are listed in Appendix E and Appendix F, respectively. The results are discussed in Chapter 5.

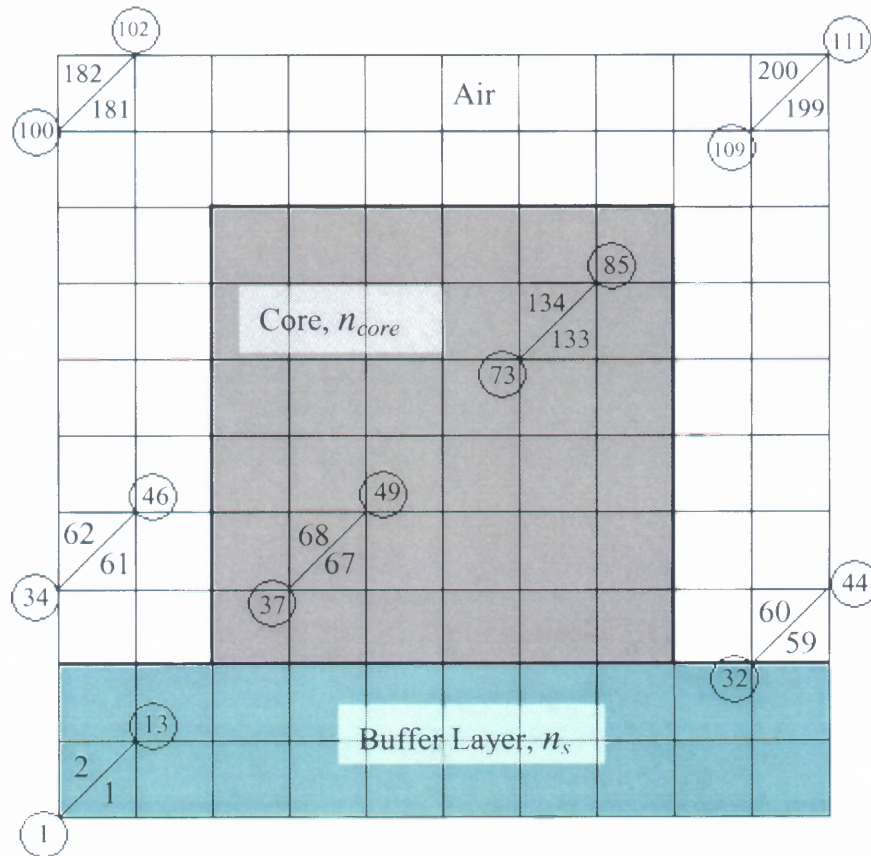


Figure 3.9 Refractive index profile of the MZI sampling arm (without cladding).

CHAPTER 4

INTEGRATED CHEMICAL SENSOR

Integrated optical waveguide sensors based on the principle of Mach-Zehnder Interferometry have been shown to be able to detect the changes in refractive index within the evanescent field of the waveguide. The advantages of this type of sensors include high sensitivity, immunity of electromagnetic field and external parameters (temperature, vibration, etc.), low cost production and compact size. Together with the innovative silicon technology, these devices are suitable for direct detection and for in-situ measurements. Because of this, these sensors are of interest in the chemical and biomedical fields, for bioprocessing industry and for environmental monitoring applications.

There are several different designs of the waveguide sensors and hence several experimental techniques of measurements reported in the literature. A Mach-Zehnder interferometer with a tapered output section^{29,47,48} has produced a different output phenomena compared to a 3 dB Y junction^{24,25}. The latter case produces a variation in the output intensity that results from a variation in the optical path difference between the two arms of the interferometer, which may also be a result of fluctuation of the light source intensity. This disadvantage has been overcome by the design of tapered section at the output end that enable one to observe an interference pattern at the output, and the observed displacement of the fringes is solely due to the optical path difference between the two arms, and is independent of source power fluctuation. Even though this is a popular design for chemical application⁴⁸, the technology used to create the tapered MZI

sensor is of the $\text{Na}^+ - \text{K}^+$ ion exchange in glass substrate. On the other hand, the Y junction MZI, which is generally used as immunosensor,⁵¹ utilizes the advanced silicon IC technology associated with material used for optical waveguides (silicon and its compounds). This technology has advantages such as: the possibility of obtaining efficient coupling between optical fibers and waveguides, and the possible integration of opto-electronics components on the same chip.^{49,50}

Most of the experimental techniques using integrated MZI sensor for sensing purposes uses a He-Ne laser or laser diode as the single wavelength source and photodiode^{51,28,26} or CCD array^{47,48} as detector. The limitation of using single wavelength source is that, it confines the application of the sensor only to single analyte detection. In this chapter, a new idea is presented by using multi-wavelength source³⁰ as the input light source instead of the single wavelength source. The choice of multi-wavelength source leads to the possibility of multiple chemical concentration detection, as different chemical species exhibits its own characteristic fingerprint. The results of interference spectrum at the near-infrared region recorded by a spectrum analyzer shows a shifting of the fringes corresponding to various concentrations of chemicals, which has been reported in Chapter 5.

Two different broadband sources were used in the experiments, namely, a white light source and a 1.5 μm broadband source. The experimental setup for the sensing measurements involved different chemical solutions. The experimental procedures and the data acquisition are explained in this chapter. The comparison of the power splitting between both the reference and sampling arms is discussed. Total power loss in a single straight waveguide is also measured and calculated.

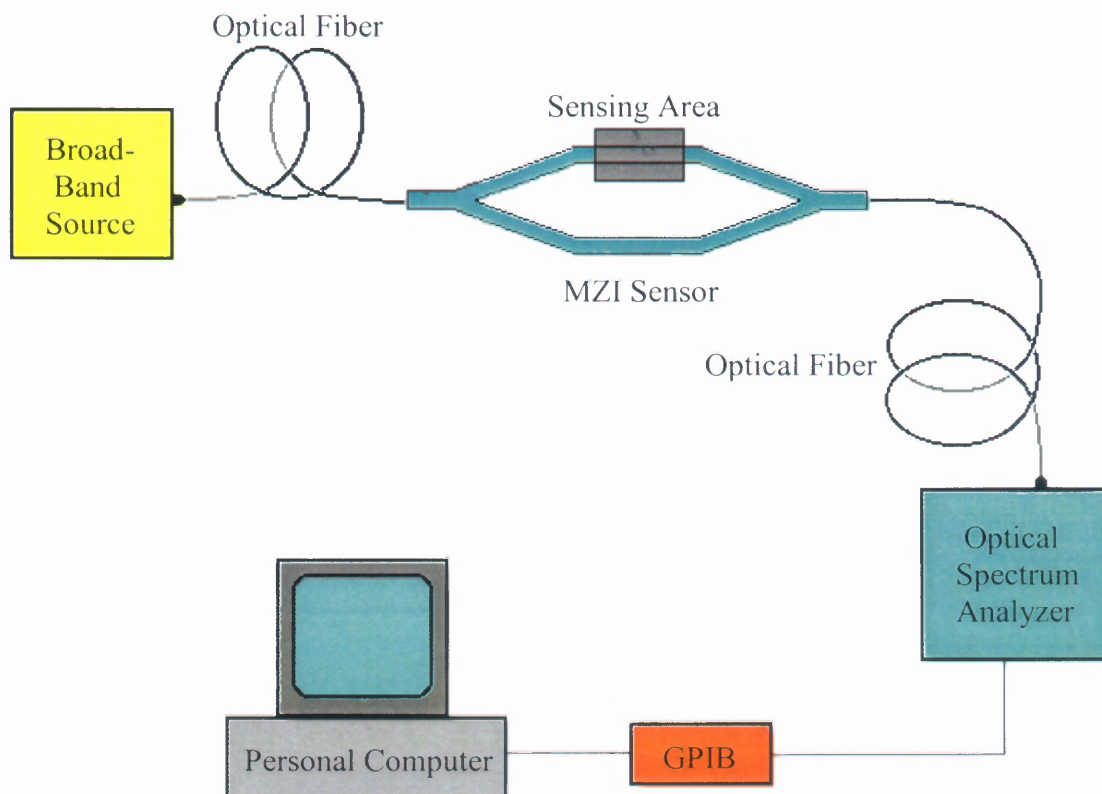


Figure 4.1 Schematic of the experimental setup for the MZI chemical sensor using broadband source.

4.1 Multi-Wavelength Experiment

The experimental setup for the Mach-Zehnder interferometry detection using broadband white light source is demonstrated in Figure 4.1. The light sources include (i) an Anritsu MG922A white light source, and (ii) a JDS 1.5 mm broadband source. The Advantest Q8381A Optical Spectrum Analyzer was used to measure the output results. The light is butt coupled directly into the waveguide through a single mode silicon optical fiber with $7.8\ \mu\text{m}$ core, and out-coupled to the spectrum analyzer by another similar optical fiber. The data of the output light spectrum measured by the optical spectrum analyzer was then

recorded by a Labview programming into the personal computer for data analysis via GPIB interface.

The specification of the two light sources are described as follow:

Anritsu MG922A White Light Source

The spectrum of the white light source in the near infrared region after transmitting through the optical fiber is shown in Figure 4.2. As seen in the figure, the light source exhibits a decreasing in intensity with respect to the wavelength from 1000 nm to 1200 nm. However, it is considered stable from 1200 nm to 1700 nm. This is important in the sense that the input light into the Integrated Mach-Zehnder Interferometer sensor must show no sign of any intensity modulation. Hence, evidence of interference occurred inside the sensor could be concluded to have taken place if any modulation is detected in the output intensity.

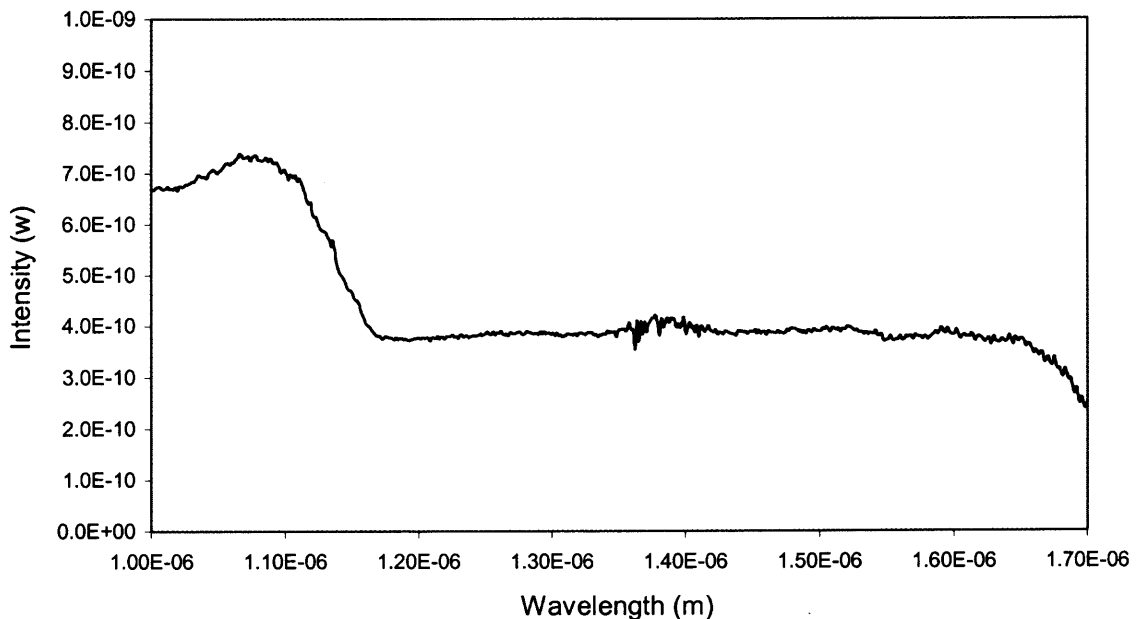


Figure 4.2 Spectrum of the Anritsu MG922A white light source.

JDS 1.5 μm Broad Band Source

The spectrum of the 1.5 μm broadband light source after transmitting through the optical fiber is shown in Figure 4.3. As can be seen in the figure, the light source does not exhibit a flat and stable spectrum after transmitting through the optical fiber. Nevertheless, the source is considered in this experiment because of the wavelength range is around the 1.55 μm , which is the absorption band of most of the hydrocarbon based chemicals.

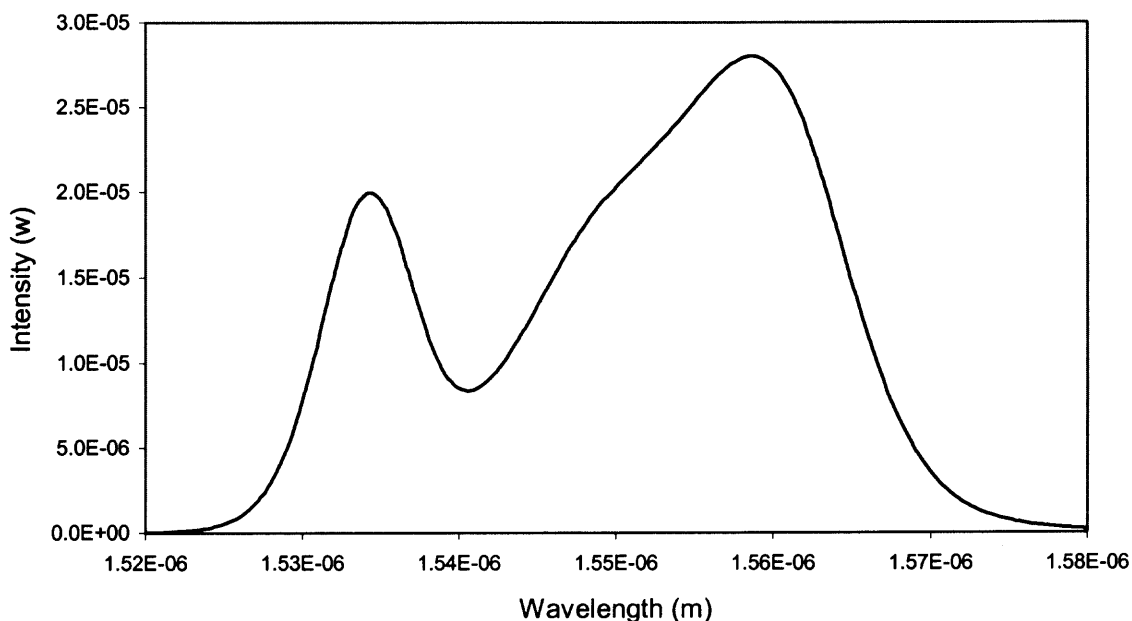


Figure 4.3 Spectrum of the JDS Uniphase 1.5 μm broadband source.

4.2 Experimental Procedures

The liquid chemicals used for the experiments are ethanol and methanol diluted in distilled water to different percentages of concentration. These alcohol based organic chemicals were specifically chosen for the experimental purpose because they have

absorption in the near infrared region. The preparation of the solutions in $w\%$ volume of the chemical in water is described as

$$w\% = \frac{w \text{ ml of chemical}}{100 \text{ ml of water}} \quad (4.1)$$

For example, a concentration of 20% of ethanol was prepared by dissolving 20 ml of ethanol into 100 ml of distilled water. Hence the chemical was prepared in 10% to 50% with 10% increment for used in the experiment.

The sample used for the experiment was cleaved from the wafer such that each sample contained two *dies* of the Integrated Mach-Zehnder Interferometer sensors. The experiments were performed with the solutions dropped on top of the sensor. After each measurement, the chemical solution was drained from the sensor and cleaned with distilled water to minimize the contamination of the chemical residue. Distilled water, represented 0% of concentration, was first to be measured, then followed by 10% of ethanol/methanol and the next increment of concentration, and so on. The reason in performing the experiments from the lower to higher concentrations is to avoid the cross-concentration contamination by the higher concentration solutions to the lower concentration solutions.

4.3 Data Acquisition

The output result of each measurement of different concentration was recorded into the personal computer for later analysis. This important task was performed by utilizing the GPIB (General Parallel Interface Bus) interface, and controlled by the Labview programming. Figure 4.4 demonstrates the Labview program flow-charts for the interfacing between the Advantec Optical Spectrum Analyzer and the personal computer.

The Labview control panel controlled the spanning range of wavelengths, i.e. setting the minimum and maximum wavelength for the spectrum scanned; average point of the scanning; and the data were saved automatically to the hard drive in text file format after completing the scanning.

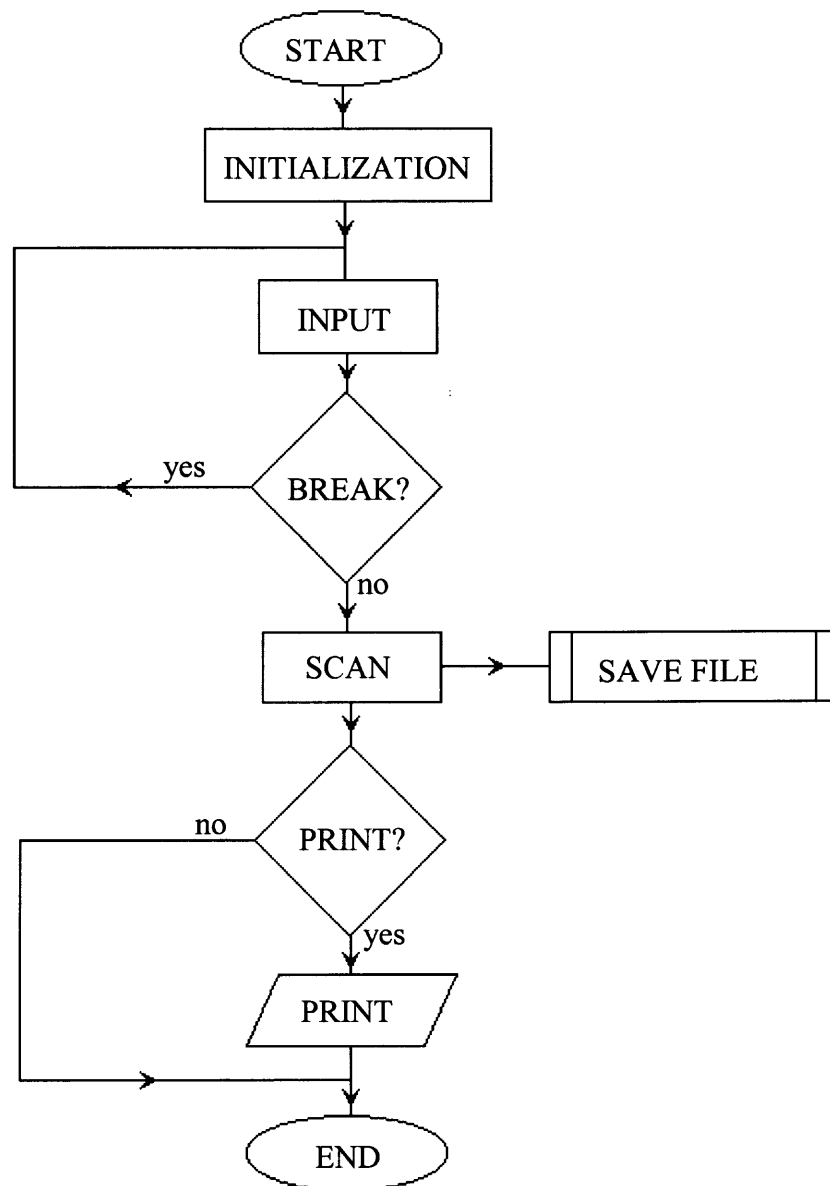


Figure 4.4 Labview program flow-chart for controlling the optical spectrum analyzer.

4.4 Power Loss

The total power loss due to waveguide loss mechanisms such as scattering loss, surface roughness, and leaky mode to substrate, are investigated for the second-batched of Integrated Mach-Zehnder Interferometer sensors. The procedures for the inspection has already been discuss with detail in Section 2.7.2 for the Y-junction. In this section, the output intensities from both the reference and sampling arms were compared. Two different arm lengths, i.e. 10 mm and 2 mm, were evaluated for comparison. Power attenuation of single waveguide was examined as well.

The second-batched integrated MZI sensors fabricated thereafter have been perfected to minimize the errors as explained in Section 2.7. The testing results for the new sensors are quite promising in the sense that there are no misalignments occurred in the new integrated MZI sensors. However, the problem of over-etching on the sampling arms still remained. Although it is not as serious as mentioned in Section 2.7.3, yet it is considered as an imperfection factor to the fabrication, and to the whole project as well. Hence, it is suitable to re-test the Y-junction for the power loss measurement between the two arms.

The setup for the testing purpose is depicted schematically in Figure 4.5. The 10 mm and 2 mm arm length sensors with 6- μm core width were investigated for comparison. In this experiment, the light source used was the Anritsu MG922A Broadband White Light source. The ratio of the normalized output intensity of the reference arm to that of the sampling arm is determined from Figure 4.6 and Figure 4.7 for 10 mm and 2 mm arm lengths, respectively.

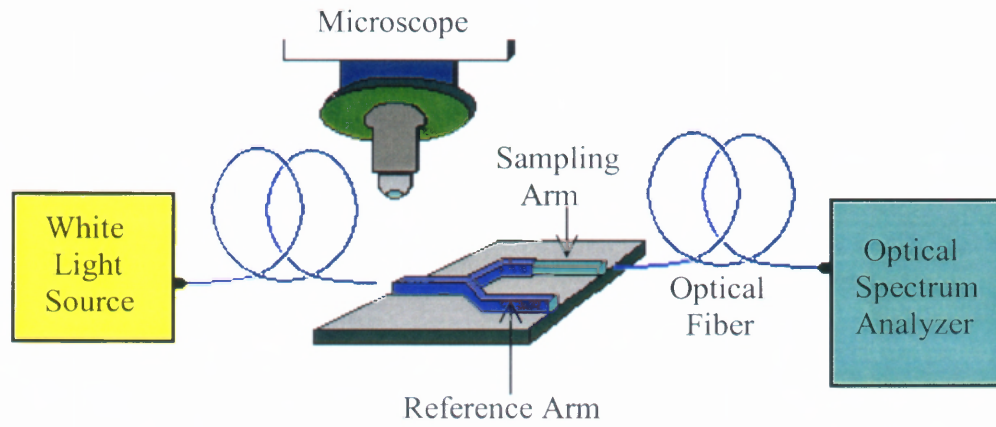


Figure 4.5 Experimental setup to measure the output power from both the sampling arm and the reference arm of a Y-junction.

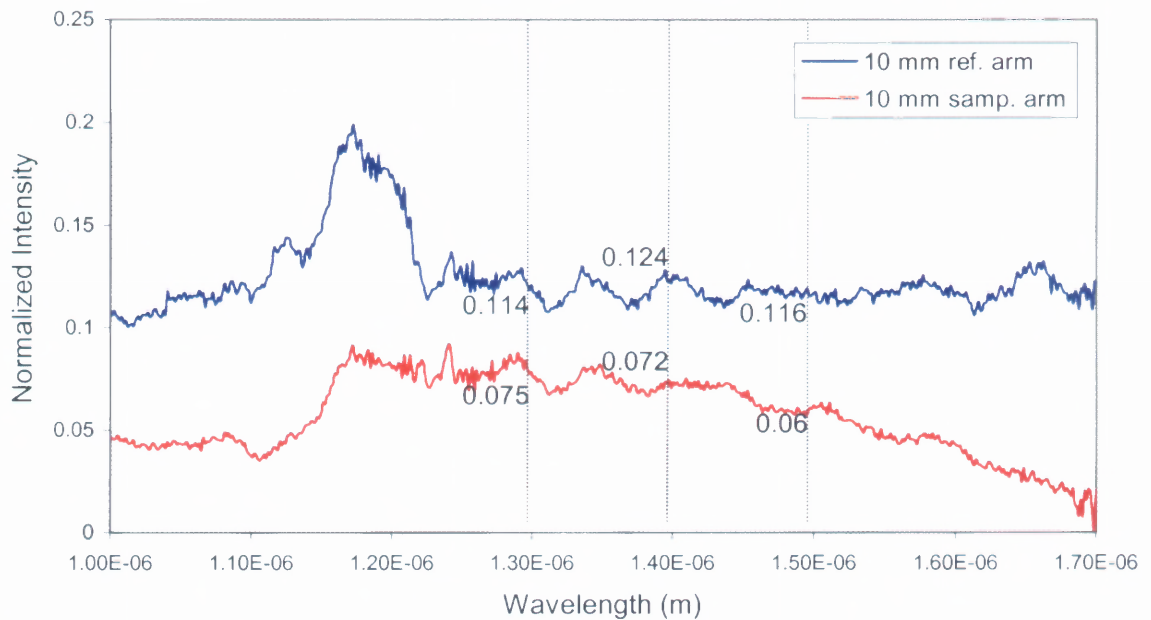


Figure 4.6 Output results of reference arm and sampling arm with 6 μm core width and 10 mm arm length.

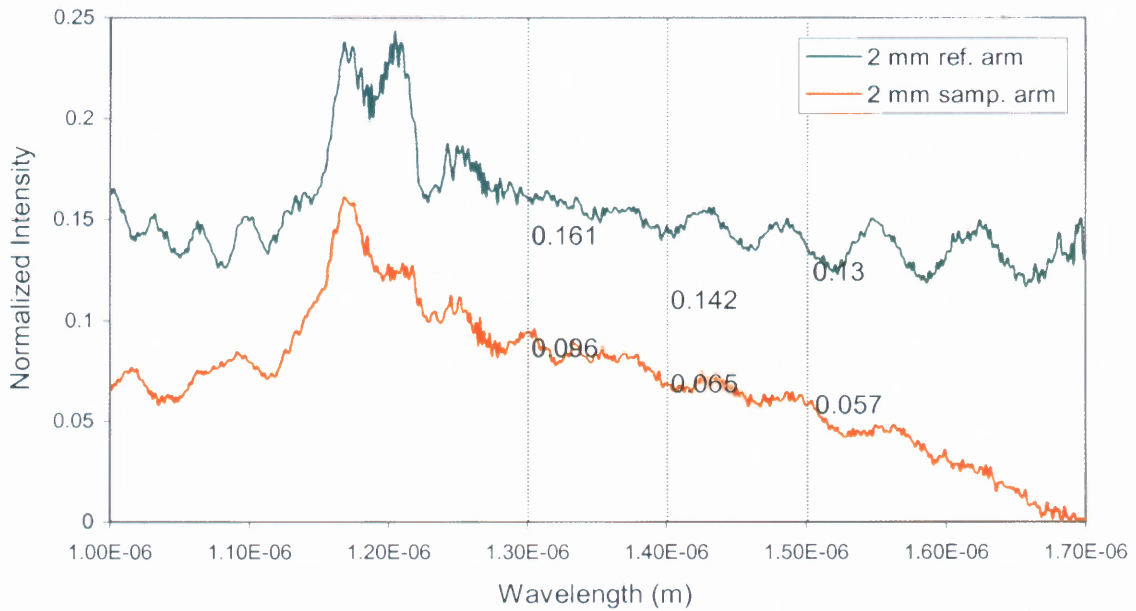


Figure 4.7 Output results of reference arm and sampling arm with 2 mm arm length.

The percentage of the output power, $\%P^i$, transmitting through the waveguide can be calculated from

$$\% P^i = \frac{P_{output}^i}{P_{total}} \times 100\% \quad (4.2)$$

where the superscript i represents the reference arm or the sampling arm respectively, and P_{total} is the total output power of the two arms.

Table 4.1 lists all of the output power splitting ratios of the two arms for 10 mm and 2 mm arm length sensors at three different wavelengths, namely, 1300 nm, 1400 nm, and 1500 nm. The table shows that the power loss in both arms increases with respect to the increase of wavelength in this region due to the absorption by silicon in the wavelength towards the mid-inferred range. In order to examine the losses caused by the window opening at the sampling arm, another set of measurement were made using the Hewlett Packard HP8152A Optical Average Power Meter instead of Optical Spectrum

Analyzer to really measure the total output power from the sensor arms. The results are listed in Table 4.2 for the Y-junction without window opening and the sampling arm with four different lengths. The results shows that the power splitting ratios of all the four sensors are quite similar with only around 7% different between the 4 mm length with the three longer arm length. The Y-junction alone has splitting ratio of 59:41. Also, the sampling arms show 1% to 3% losses. The output intensity of the reference arms are higher than that of sampling arms for all sensors showing that the problem is probably due to the window mask design with the taper section of the Y-junction slightly off to the sampling arm. Note that the power splitting ratios shown in Table 4.1 are different between the 10 mm and 2 mm arms. The reason that might cause the difference is due to the inefficient coupling between the fiber and the waveguide at both input and output ends of the two sensors when performing this experiment.

Table 4.1 Output power splitting ratio (reference arm: sampling arm) for 10 mm and 2 mm length at 1.3 μm , 1.4 μm , and 1.5 μm wavelengths

Wavelength (nm)	10 mm Arm Length	2 mm Arm Length
1300	60:40	63:37
1400	63:37	69:31
1500	66:34	70:30

The total power loss in a single straight waveguide is also measure in this section. Figure 4.8 shows the normalized output power of two different length straight waveguides with 6 μm core width measured with respect to wavelength. The power loss in a single straight waveguide can be determined by

$$P_{\text{output}} = P_{\text{input}} \exp(\alpha l_i) \quad (4.3)$$

where l is the length of the straight waveguide, and α is the power loss in the waveguide. Hence the power loss for a straight waveguide can be calculated using two similar waveguides in different lengths by eliminating the input power, P_{input} , assumed that it is constant for both cases. Therefore the total power loss is defined as

$$\alpha = \frac{1}{l_2 - l_1} \ln \left(\frac{P_{\text{output}}^1}{P_{\text{output}}^2} \right) \quad (4.4)$$

Table 4.2 Output power measured from reference arm and sampling arm of different sensors and the Y-junction

Arm length	% Output Power	
	Reference Arm	Sampling Arm
Y-junction	59	41
4 mm	63	37
6 mm	60	40
8 mm	60	40
10 mm	60	40

where the superscripts of 1 and 2 of P_{output} represent the output power of two straight waveguides with two different lengths, l_1 and l_2 , respectively. The results of the power loss in a straight waveguide with respect to three different wavelengths are tabulated in Table 4.3.

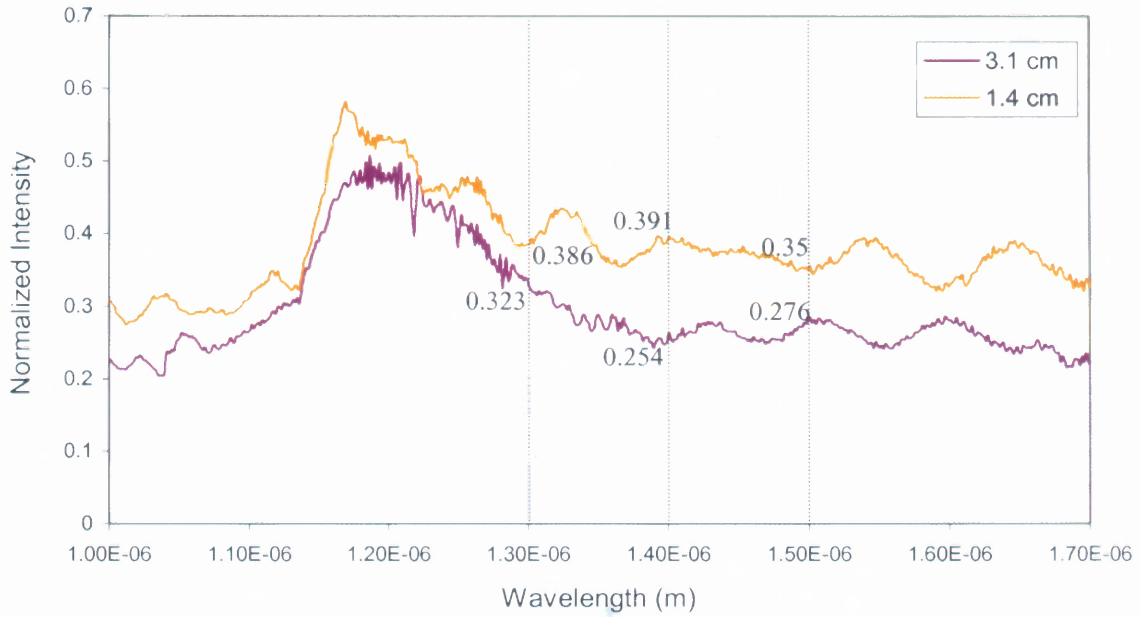


Figure 4.8 Output results of straight waveguides with 3.1 cm and 1.4 cm long.

The total power loss in a waveguide consists of the power loss inside the waveguide as scattering loss and power absorption; and power loss due to the inefficiency fiber-to-waveguide (and waveguide-to-fiber) coupling. This inefficiency of coupling is owing to several reasons, namely, (i) the optical fiber core diameter of $7.5\ \mu\text{m}$ is larger than the waveguide core diameter of $6\ \mu\text{m}$, (ii) the fiber end and the waveguide end were not polished, and as the result, rough surface scattered off part of the light inside and outside the waveguide, and (iii) energy feedback at every end surface of the

fibers and the waveguide in reverse direction to the transmission of light also accounted for the loss.

Table 4.3 Total power loss in a straight waveguide with respect to three different wavelengths

Wavelength (nm)	α (cm ⁻¹)
1300	0.105
1400	0.254
1500	0.140

CHAPTER 5

RESULTS AND DISCUSSION

The theoretical and experimental results of an integrated Mach-Zehnder Interferometer are presented in this final chapter with detailed discussion on each subject. The Marcatili solution is first discussed, and the cutoffs for the three lowest TM modes are displayed. The FEM solutions with the entire corresponding mode fields' distribution for the TM modes and TE modes are illustrated in three-dimensional graphics. Mode cutoffs are also calculated using this method.

The experimental results are shown for light sources, which are the white light source and the $1.5\ \mu\text{m}$ broadband source. Discussions are focused on the results obtained from the sensors with waveguide dimension of $5\ \mu\text{m} \times 8\ \text{mm}$, $5\ \mu\text{m} \times 10\ \text{mm}$, $6\ \mu\text{m} \times 8\ \text{mm}$, and $6\ \mu\text{m} \times 10\ \text{mm}$, where the latter number represents the arm length of the sensor in between the two Y-junctions. Finally, the comparison between the two methods and among the theoretical and experimental results is discussed.

5.1 Marcatili's Solution

The analytical solution for the waveguide modes cutoff using this Marcatili's approximation can be determined by first solving the k_x and k_y from dispersion equations (2.35) and (2.36), respectively, by making use of equations (2.37) and (2.38), as discussed in Section 2.3.2. The parameters used in the equations are

$$n_{core} = 1.466$$

$$n_{clad} = 1.458$$

$$k = \frac{2\pi}{\lambda}$$

and

$$a = 6 \mu\text{m}, \quad d = 6 \mu\text{m}$$

with $p = q = 1$ for TM_{11} mode, $p = 1$ and $q = 2$ for TM_{12} mode, $p = 2$ and $q = 1$ for TM_{21} mode. These parameter values are also used in the FEM computational solution. The k_x and k_y obtained were then substituted into equation (2.39) for the propagation constant β . This propagation constant can be related to the normalized propagation constant as in equation (3.93), which is

$$b = \frac{\left(\frac{\beta}{k}\right)^2 - n_{\text{clad}}^2}{n_{\text{core}}^2 - n_{\text{clad}}^2}$$

The conditions for the guided modes are stated, from equation (2.13), as

$$0 \leq b \leq 1 \quad (5.1)$$

and a plot of b versus wavelength λ for the three lowest TM modes determines the corresponding cutoffs where the cutoff condition is expressed as $b = 0$.

Since the dispersion equations are transcendental, hence it can only be solved by iteration methods such as bisection method or Newton-Raphson method. Therefore, a Mathematica program was written to solve this type of equation, utilizing the Newton-Raphson method. This Mathematica program code is listed in Appendix K, and the solution of the cutoff modes is depicted in Figure 5.1. The figure shows the three lowest transverse magnetic modes TM_{11} , TM_{12} , and TM_{21} with their cutoffs at $b = 0$. From the graph, the fundamental mode cutoff wavelength is $5 \mu\text{m}$, while the second mode cutoff wavelength is $2.5 \mu\text{m}$.

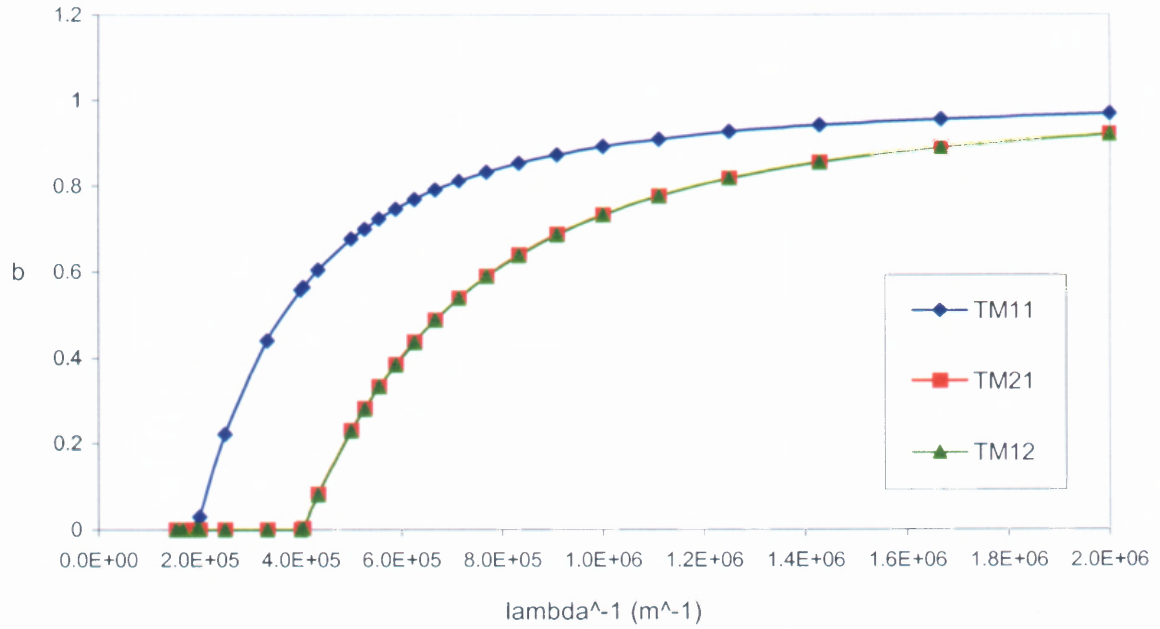


Figure 5.1 Cutoff values for the three lowest TM modes solved by using the Marcatali's approximation for the 6 μm core waveguide.

5.2 FEM Solutions

Finite element method is accurate in solving the electromagnetic modes fields in various waveguide geometries. As explained in Section 3.5, the TE and TM modes of the integrated MZI waveguides are solved by utilizing the FEM weak form of two-dimensional wave equations (3.95) and (3.97), respectively with the waveguide index profile, element geometry, and nodes location as described in Figure 3.8 and Figure 3.9. The Matlab programs written to solve the FEM equations are listed in Appendix E for TM modes, and Appendix F for TE modes.

The two-dimensional graphic of TM_{11} mode field at 1500 nm wavelength generated with 200 elements is illustrated in Figure 5.2, and the three-dimensional diagram is as shown in Figure 5.4. Figure 5.5 and Figure 5.6 show the modes fields for

TM_{11} and TM_{21} at 1100 nm wavelength while Figure 5.8, Figure 5.9 and Figure 5.10 depict the TM_{11} , TM_{21} , and TM_{12} at 1000 nm. Notice that there are two modes at 1100 nm, while there are three modes at 1000 nm. This means that 1100 nm is the second mode cutoff wavelength while 1000 nm is the third mode cutoff wavelength. The TE modes fields are quite similar to the TM modes fields and hence will not be shown in the dissertation. The TM modes fields of a 5 μm core waveguide at 1500 nm wavelength generated with 800 elements is also calculated and is depicted in Figure 5.3.

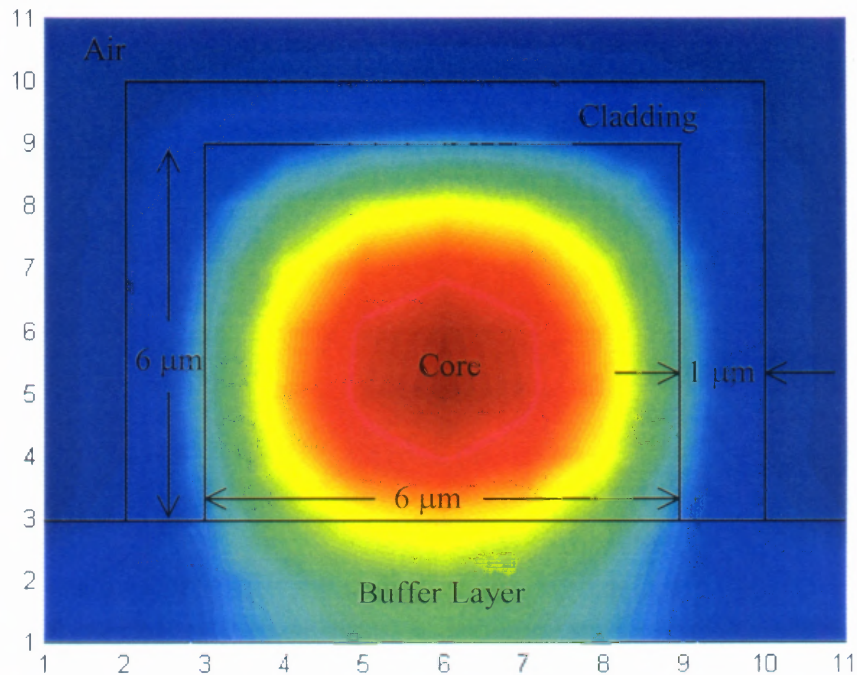


Figure 5.2 Two-dimensional graphic of TM_{11} at 1500 nm wavelength as simulated by FEM with 200 elements for the 6 μm core waveguide.

The cutoff values can be determined from the dispersion curve of b versus *inverse wavelength* calculated by the finite element method, which are shown in Figure 5.12 for the TM modes while TE modes are depicted in Figure 5.13. The cutoff wavelength for

TM_{11} and TE_{11} are around 1900 nm; for TM_{21} and TE_{21} are about 1100 nm; and for TM_{12} and TE_{12} are at 1000 nm. This means that the interferometer sensor is sensitive only in the wavelength range from 1100 nm to 1900 nm since multimode causes problem with interference. Figure 5.14 shows that the single mode cutoff is the same for TE and TM modes for square waveguide. The FEM Matlab codes are listed in Appendix G and Appendix H for TM and TE cutoffs calculation, respectively. The dispersion curve of the TM modes for the 5 μm core waveguide is shown in Figure 5.15. Note that the single mode cutoff wavelength for this case is in the range of 950 nm to 1700 nm. The cutoff wavelengths are shorter for smaller waveguide than the larger waveguide.

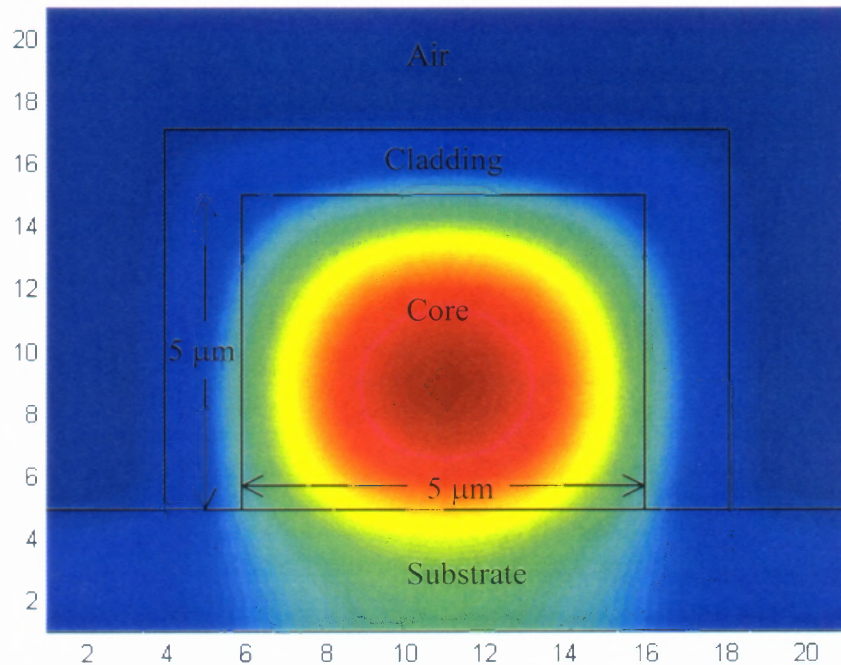


Figure 5.3 Two-dimensional graphic of TM_{11} at 1400 nm wavelength as simulated by FEM with 800 elements for the 5 μm core waveguide.

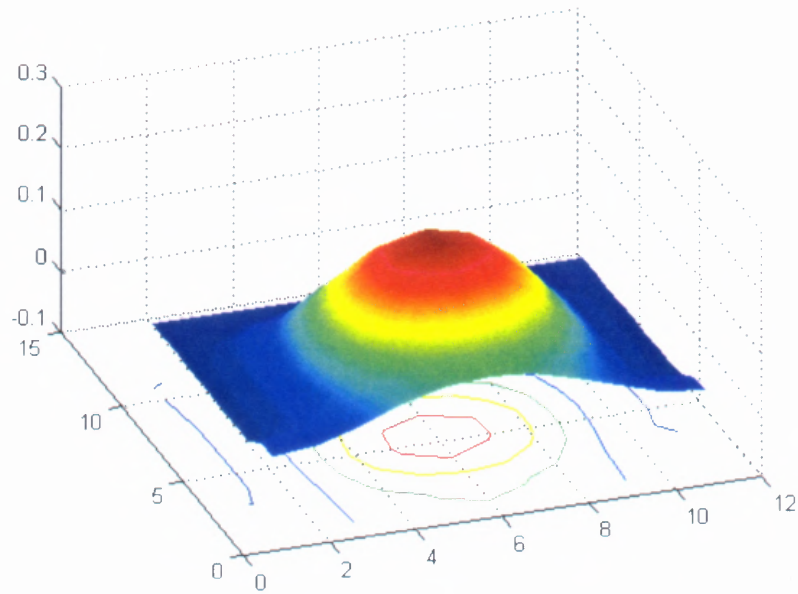


Figure 5.4 Three-dimensional graphic for TM_{11} mode at 1500 nm wavelength for 6 μm waveguide.

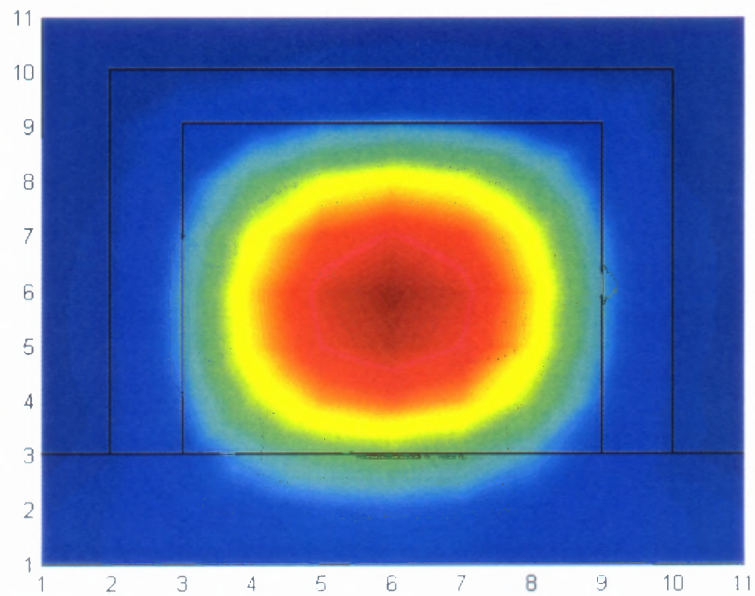


Figure 5.5 TM_{11} at 1100 nm wavelength for 6 μm waveguide.

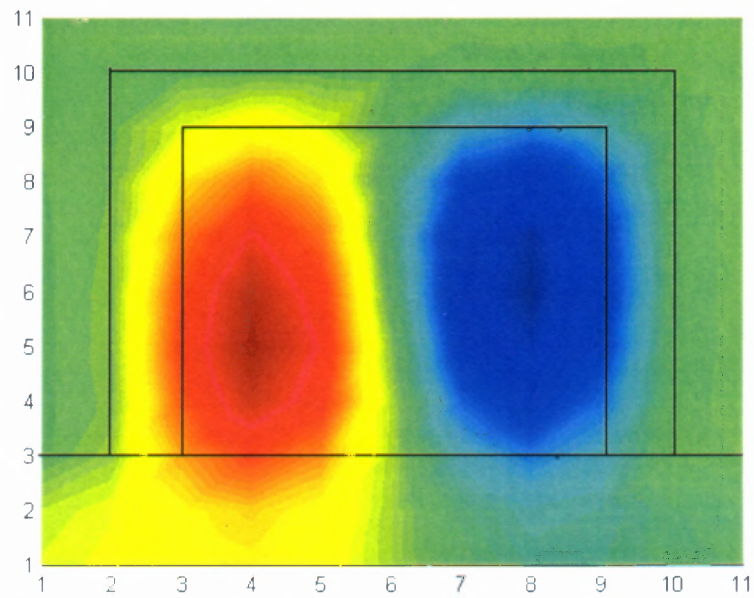


Figure 5.6 Two-dimensional graphic of TM₂₁ at 1100 nm wavelength for 6 μm waveguide.

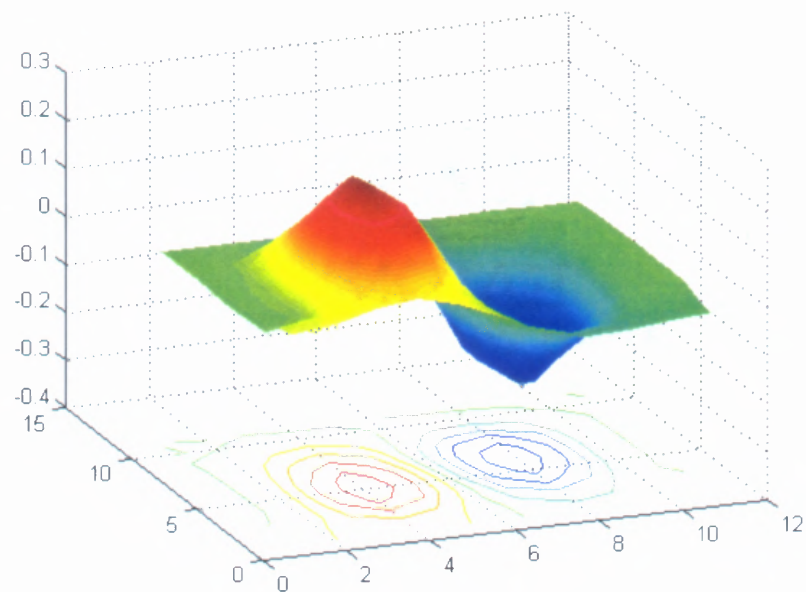


Figure 5.7 Three-dimensional graphic for TM₂₁ mode at 1500 nm wavelength for 6 μm waveguide.

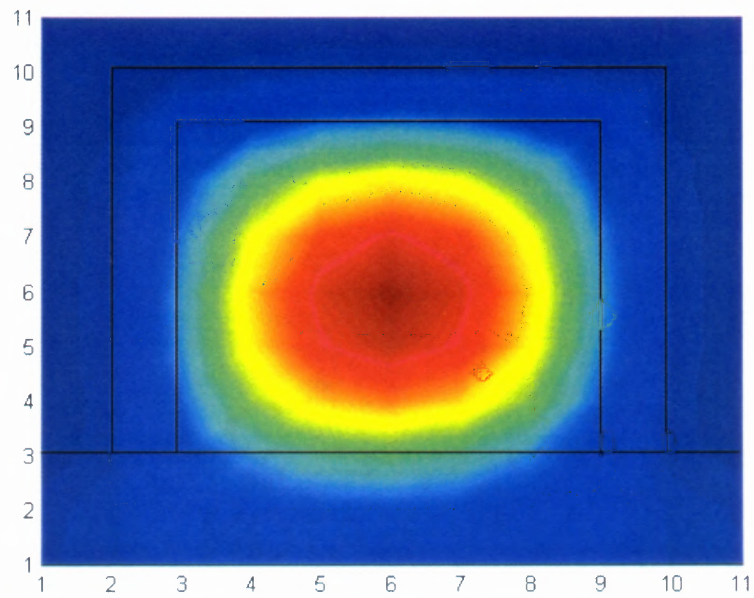


Figure 5.8 TM_{11} at 1000 nm wavelength for 6 μm waveguide.

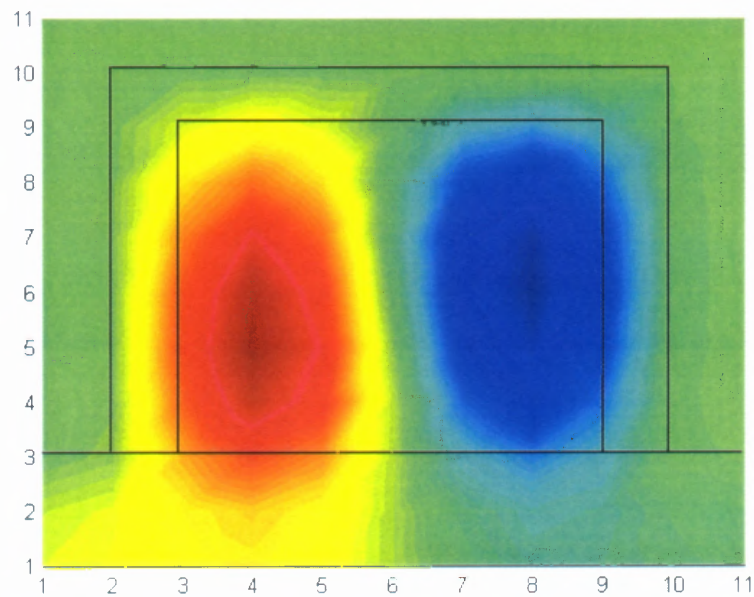


Figure 5.9 Two-dimensional graphic of TM_{21} at 1000 nm wavelength for 6 μm waveguide.

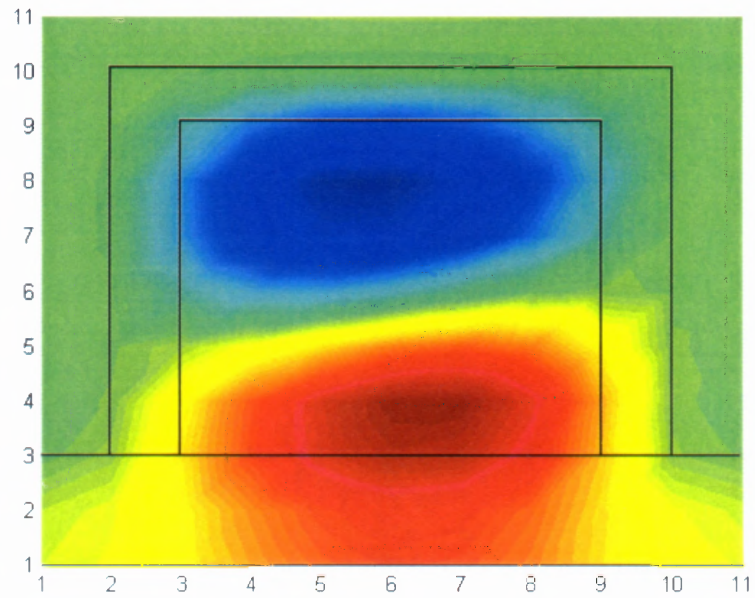


Figure 5.10 Two-dimensional graphic of TM_{12} at 1000 nm wavelength for 6 μm waveguide.

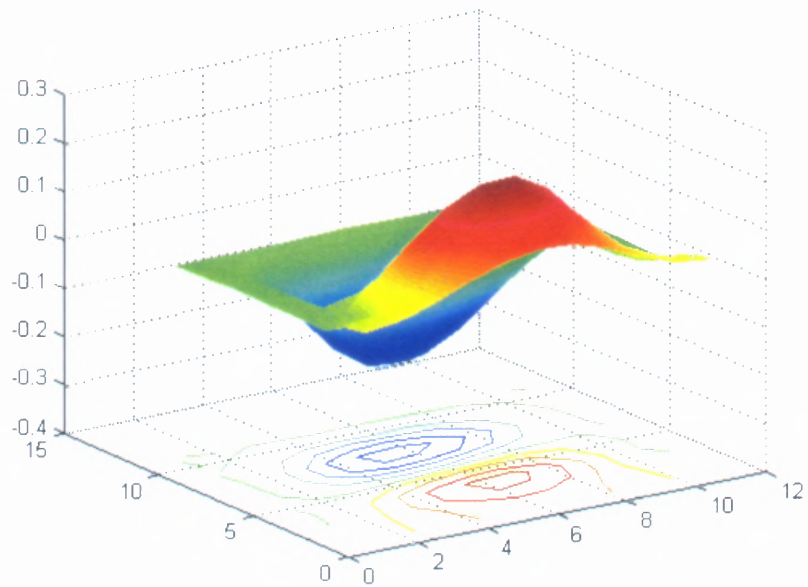


Figure 5.11 Three-dimensional graphic for TM_{12} mode at 1000 nm wavelength for 6 μm waveguide.

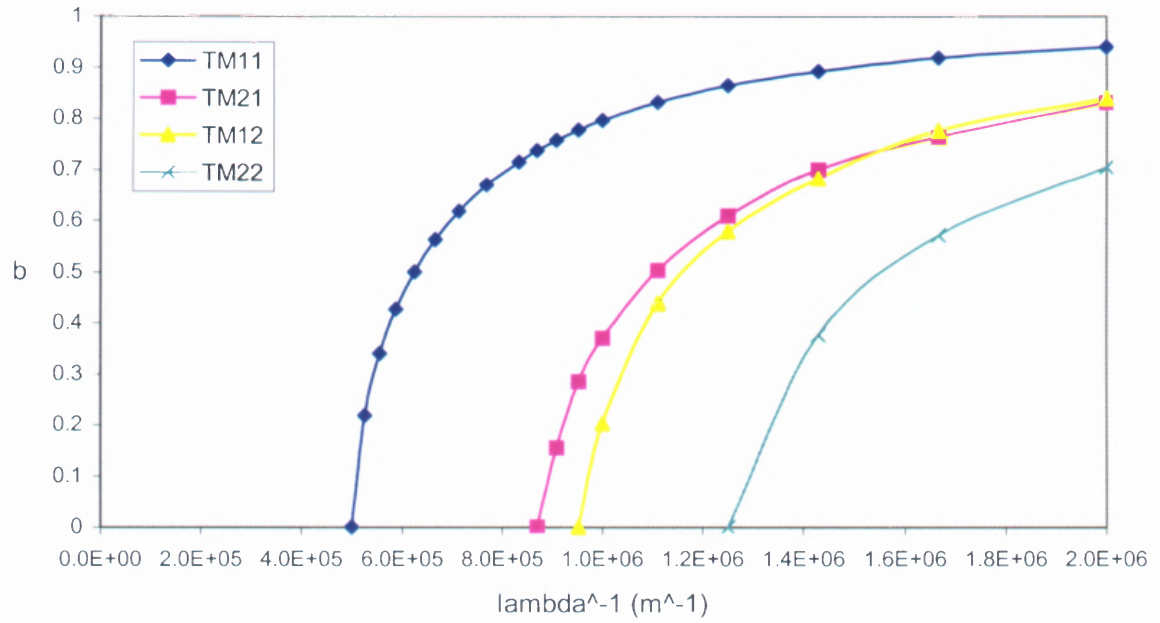


Figure 5.12 Dispersion curves for the lowest four TM modes as determined by FEM for $6\ \mu\text{m}$ core waveguide.

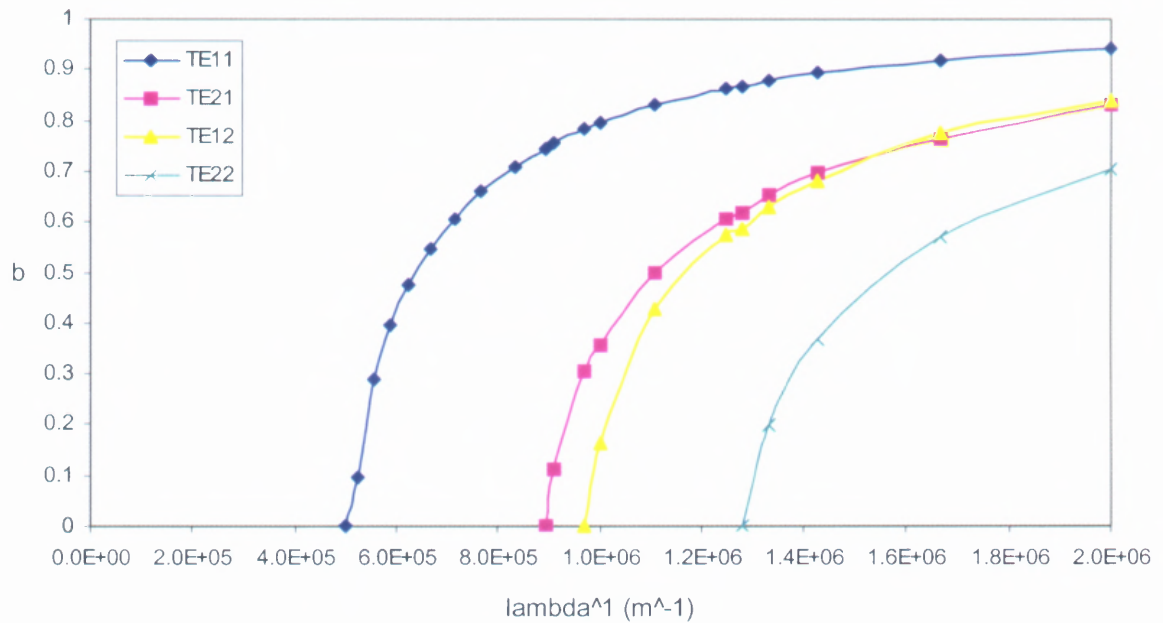


Figure 5.13 Dispersion curves for the lowest four TE modes as determined by FEM for $6\ \mu\text{m}$ core waveguide.

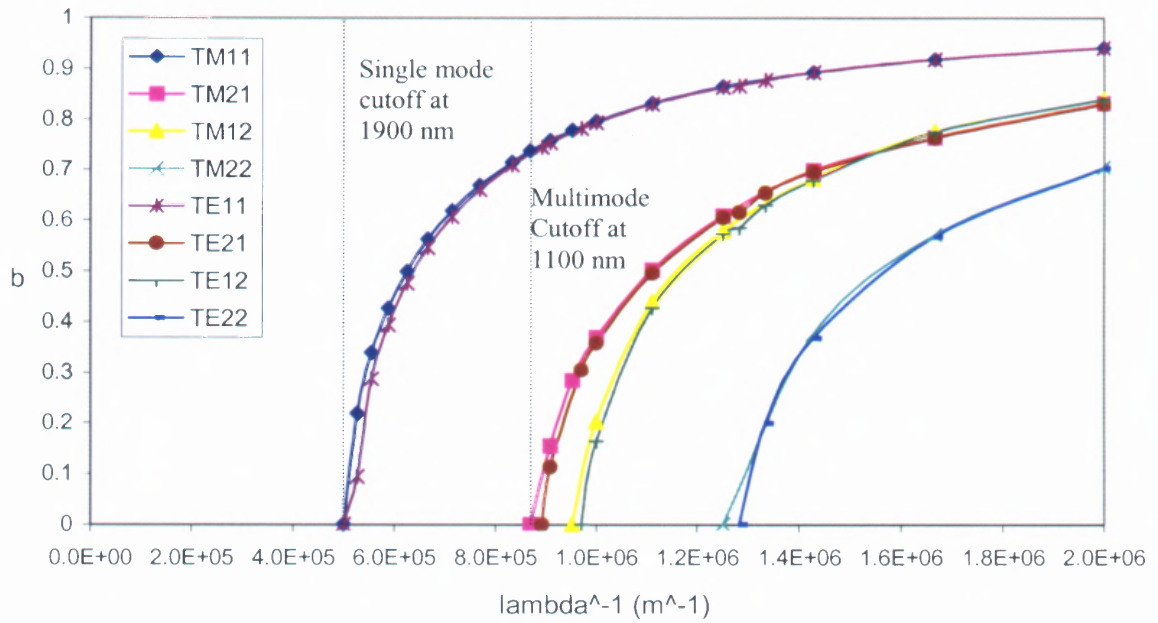


Figure 5.14 Comparison of the dispersion curves for TM and TE modes in the integrated MZI single waveguide for 6 μm waveguide.

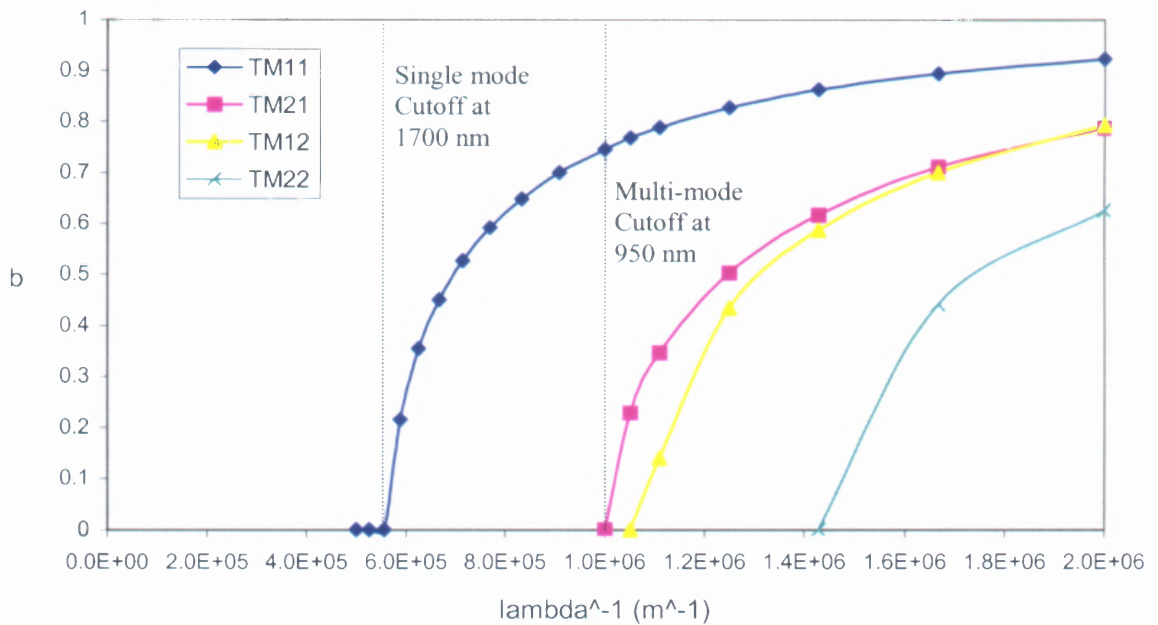


Figure 5.15 Dispersion curves for the lowest four TM modes as determined by FEM for 5 μm core waveguide.

The mode field simulation for the waveguide without cladding is illustrated in Figure 5.16 with comparison to the one with cladding. This is done by specified the refractive index of the cladding to 1.0, which is the refractive index of air, in the same FEM Matlab programs listed in Appendix E for TM modes. The corresponding dispersion curves for the four lowest TM modes are shown in Figure 5.17, which shows that the single mode cutoff for the sampling arm is between 900 nm and 1550 nm.

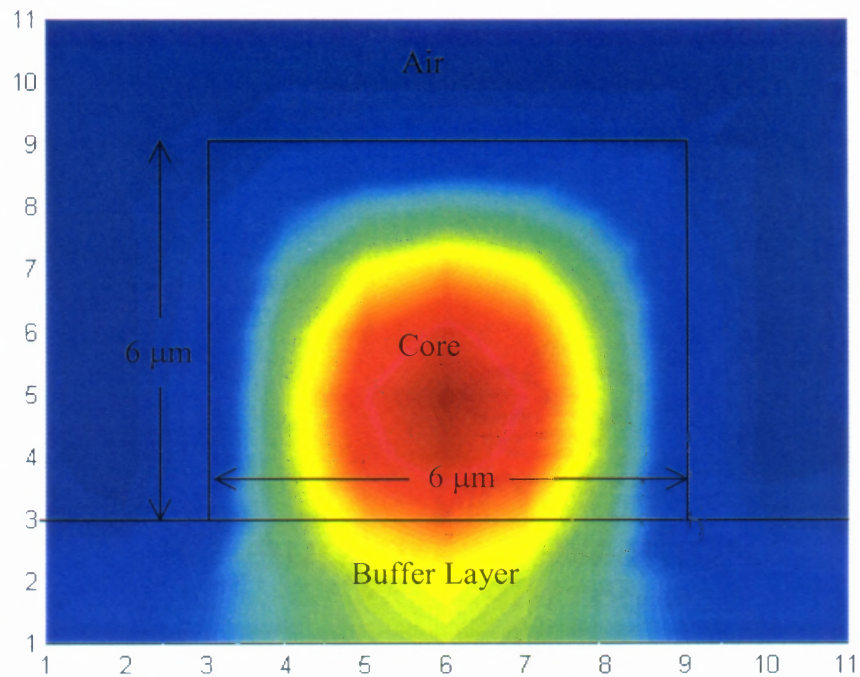


Figure 5.16 TM_{11} at 1500 nm wavelength as simulated by FEM with 200 elements for the 6 μm core waveguide without cladding.

To simulate the effect of the chemical on the mode field in the sampling arm, the refractive index of the air and the cladding are replaced by the refractive index of the chemical. For example, the refractive index of the cladding and the air are replaced by the refractive index of the 50% concentration of ethanol, which is 1.3616 from CRC

Handbook. The single mode cutoff wavelength for this case is at the range of 980 nm to 1670 nm as shown in Figure 5.18 for the four lowest TM modes on a 6 μm core waveguide. For water with refractive index of 1.333, the single mode cutoff wavelength is at 1640 nm. This means that if the chemical concentration is increase from 0% to 50%, the single mode cutoff wavelength range will be in between 1640 nm to 1670 nm. Compare to single mode cutoff wavelength range for the reference arm, which is in between 1100 nm and 1900 nm, it is clear that the input light source used for the experiments should be in the 1100 nm and 1640 nm range so that single mode propagation is maintained in both the reference and sampling arms.

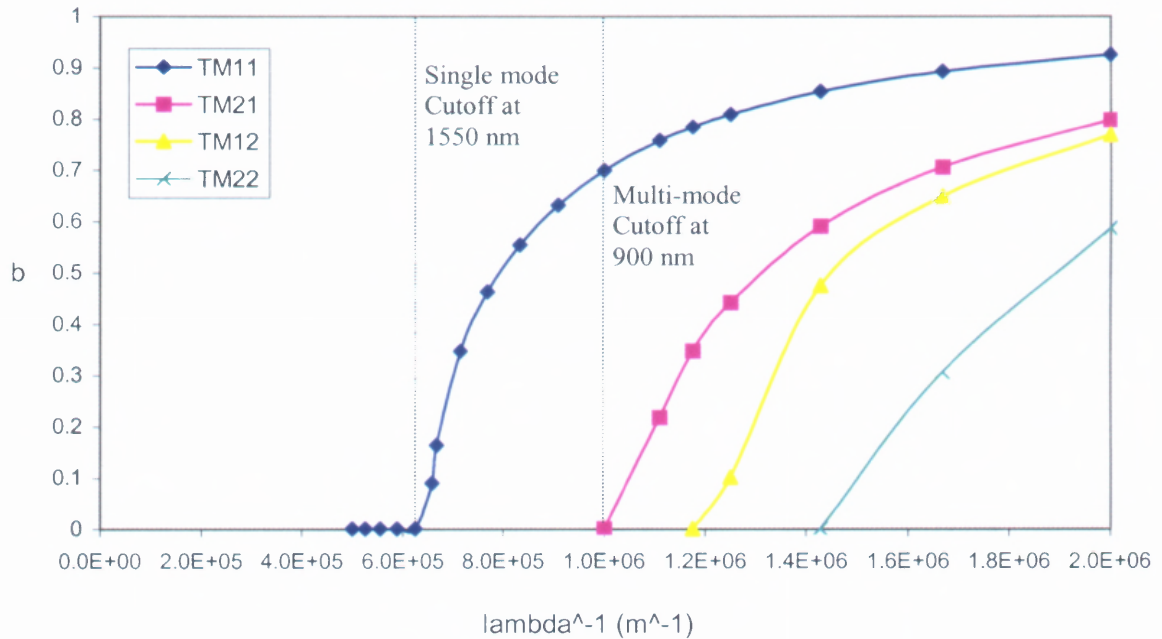


Figure 5.17 Dispersion curves for the lowest four TM modes as determined by FEM for 6 μm core waveguide without cladding.

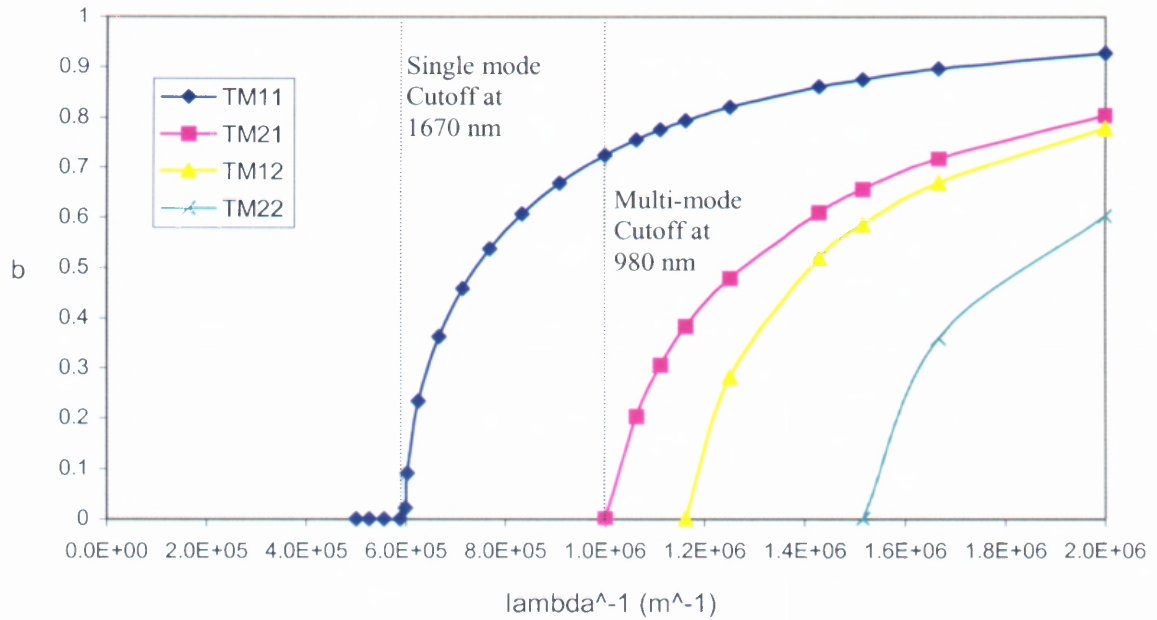


Figure 5.18 Dispersion curves for the lowest four TM modes as determined by FEM for 6 μm core sampling arm with 50% of ethanol.

5.3 Experimental Results

The results of the experiments performed as explained in Chapter 4 are discussed in the following sections. The experiments were carried out for different sensors, namely the 5 μm and 6 μm core waveguide sensors with 8 mm and 10 mm arm lengths. The chemical used for the experiments were ethanol and methanol diluted in 10% up to 50% with 10% increment. The output results using broadband white light and broadband around 1.5 μm wavelength are displayed in below.

5.3.1 White Light Source

A concern about whether the Integrated Mach-Zehnder Interferometer sensor would exhibit the interference property has to be clarified before performing the experiments with the different chemical concentrations to the interferometer sensors. Therefore,

experiments were first carried out to compare the output results of the MZI sensor, the single waveguide and the input light source. From Figure 4.2 in Section 4.1, it is clear that the input light source is constant through out the wavelength range from 1200 nm to 1700 nm. This state is to be expected in a straight single waveguide as well, however, a modulation on intensity is to be anticipated in the MZI sensor *if* interference occurs inside the interferometer. Hence, it is prudent to test on this matter before hand to avoid any misinterpretation of the experimental results later on.

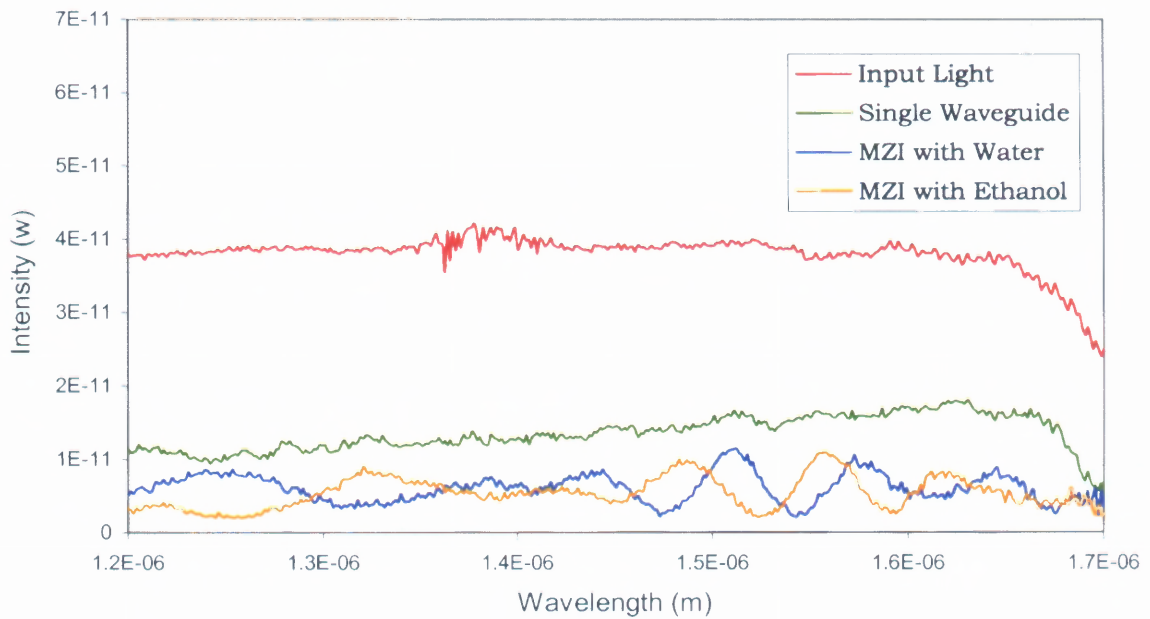


Figure 5.19 Comparison among the output profiles of the integrated MZI sensor, the single waveguide and input light profiles.

Figure 5.19 shows the experimental results of the comparison between the waveguides and the input light source. The graphs of the MZI sensors are vividly showing the modulation of intensities as predicted, while compare to the graphs of the output results from the straight single waveguide and the input light source. The figure

also displays the shifting of the spectrum of the MZI with pure ethanol from the MZI with distilled water, showing that the interferometer sensor is indeed sensitive to the change in the index of refraction on the exposed sampling arm.

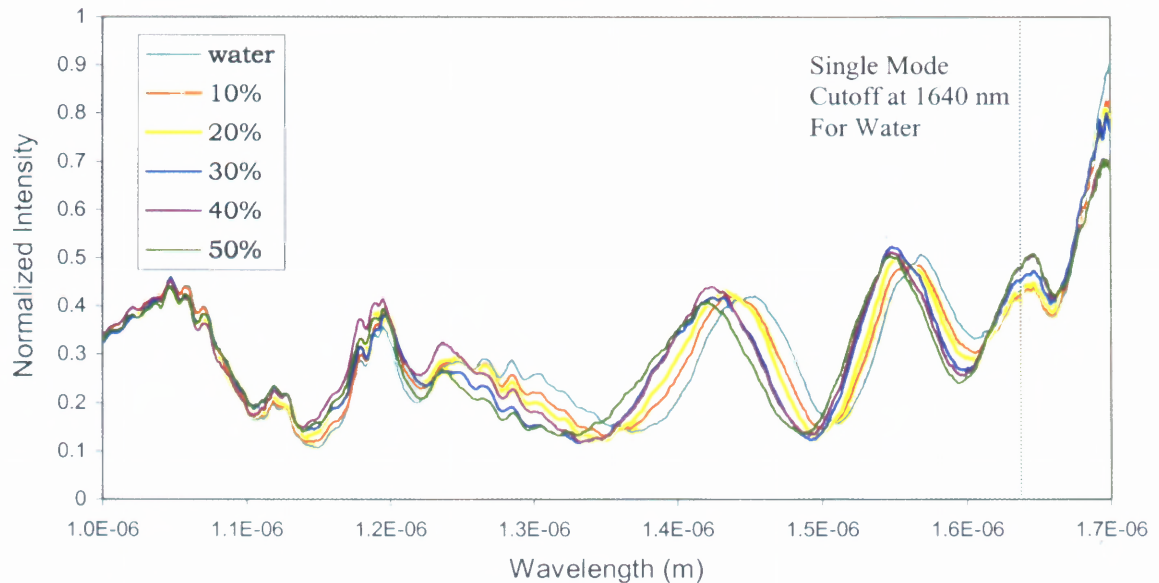


Figure 5.20 Experimental results showing the interference spectrums shifted corresponding to the various concentration of ethanol on a 5 μm MZI waveguide sensor with 8 mm arm length.

From the two output spectrums of MZI shown in Figure 5.19, the graph of ethanol is at the left hand side of the graph of water. This means that the phase shifting due to the increasing of the refractive index of ethanol on the sampling arm from that of water has shifted the output intensity of the ethanol to the left side of the water spectrum. Consequently, if several different concentration of ethanol were applied to the sensor, the output results would be shifting towards the left side gradually with the increasing of the concentration, by other mean, the increasing of the index of refraction. This logical interpretation has been proven and shown in Figure 5.20 for the 5 μm core width

waveguide sensor with 8 mm arm length. Note that the interval of each spectrum is not consistent for each 10% increment of ethanol concentration. This is because of the residue or contamination due to the previous solutions on the sampling arm, which is unpredictable even though the sensor has been thoroughly cleaned by flushing a large amount of distilled water through the sensor before the consecutive measurements.

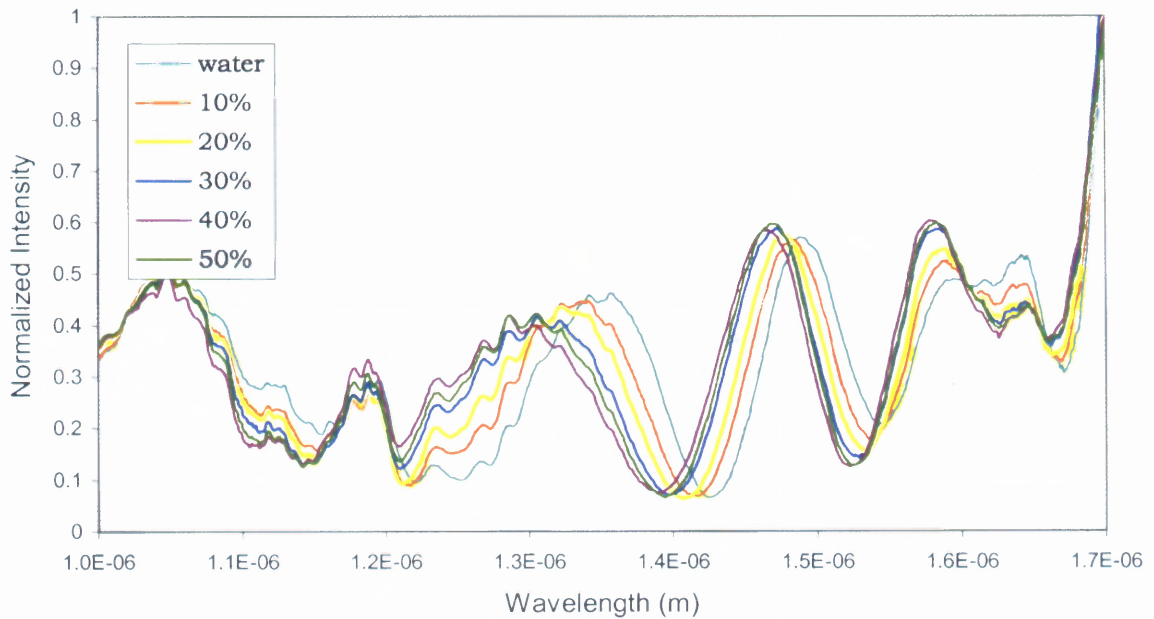


Figure 5.21 Experimental results showing the interference spectrums shifted corresponding to the various concentration of ethanol on a 6- μm MZI waveguide sensor with 8 mm arm length.

Similar experiments were performed using the 6- μm core width waveguide sensors with 8 mm and 10 mm arm lengths, and the results are depicted in Figure 5.21 and Figure 5.22, respectively. Notice that the modulation of intensity becomes more intense by means of a larger waveguide core width, which can sustain mode field with higher intensity through out the waveguide with less radiation/leakage to the cladding and the buffer layer. The 10 mm arm length waveguide sensor also shows a more sensitivity

to the refractive index changed, which is demonstrated by the wider separation of interval between each spectrum compare to the result of 8 mm arm length waveguide sensor.

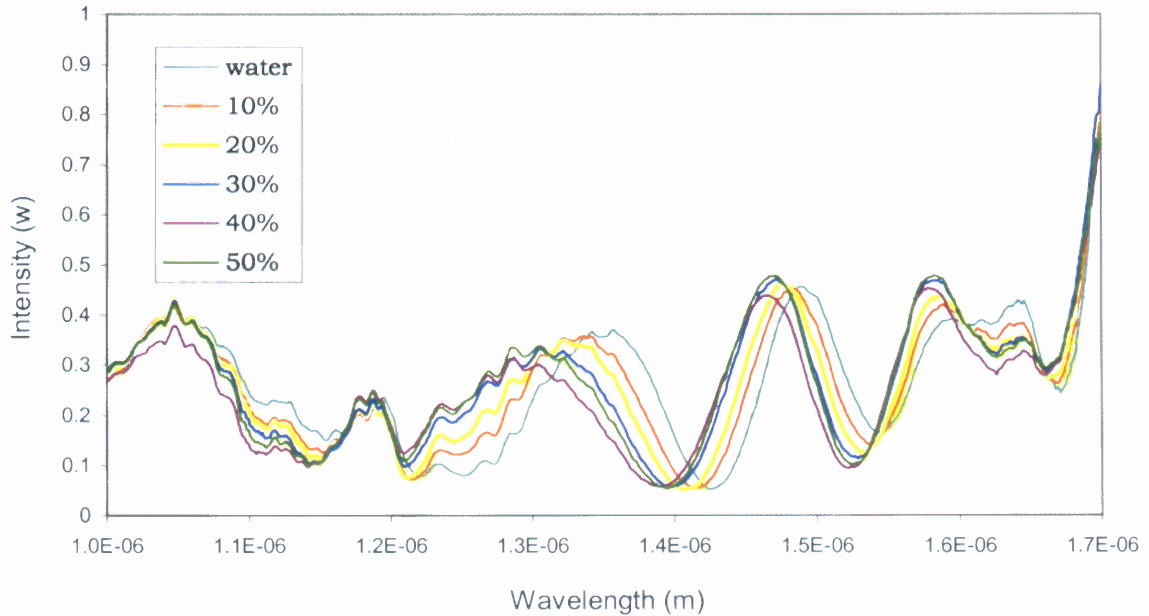


Figure 5.22 Experimental results showing the interference spectrums shifted corresponding to the various concentration of ethanol on a 6 μm MZI waveguide sensor with 10 mm arm length.

Similar experiments using methanol were also performed on the integrated MZI sensors with waveguide dimensions of 5 $\mu\text{m} \times 10$ mm, 6 $\mu\text{m} \times 8$ mm, and 6 $\mu\text{m} \times 10$ mm. The results too exhibit the same properties as mentioned above, which are shown in Figure 5.23, Figure 5.24, and Figure 5.25, correspondingly. A separate experiment was carried out for the comparison between the 50% concentration of ethanol and the 50% concentration of methanol, and the results is illustrated in Figure 5.26.

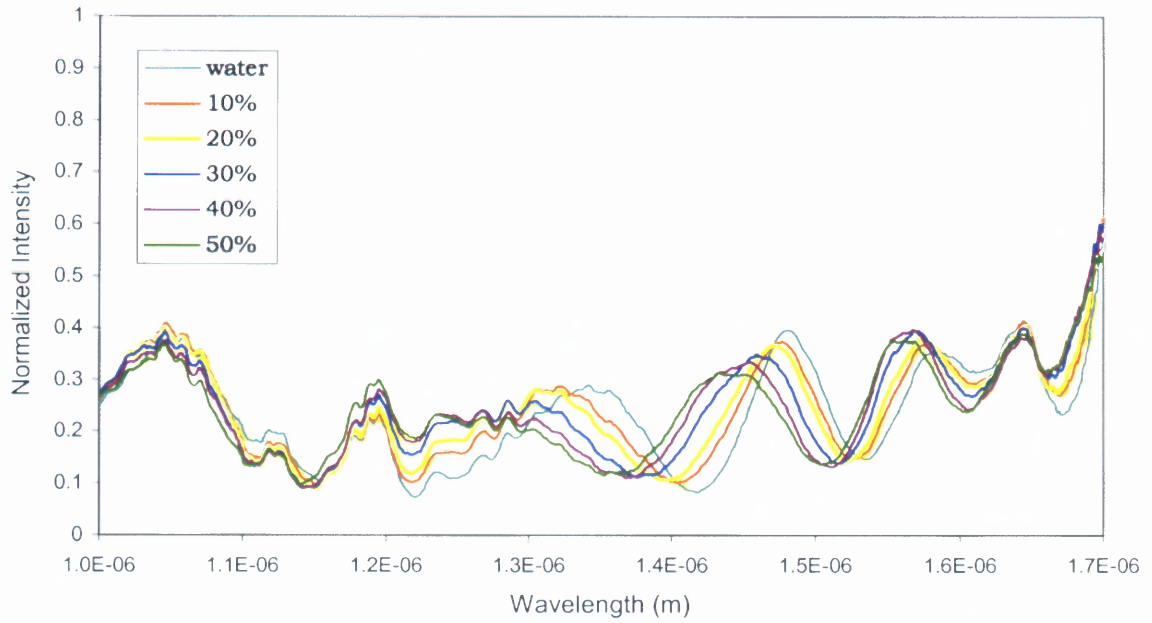


Figure 5.23 Experimental results showing the interference spectrums shifted corresponding to the various concentration of methanol on a 5 μm MZI waveguide sensor with 10 mm arm length.

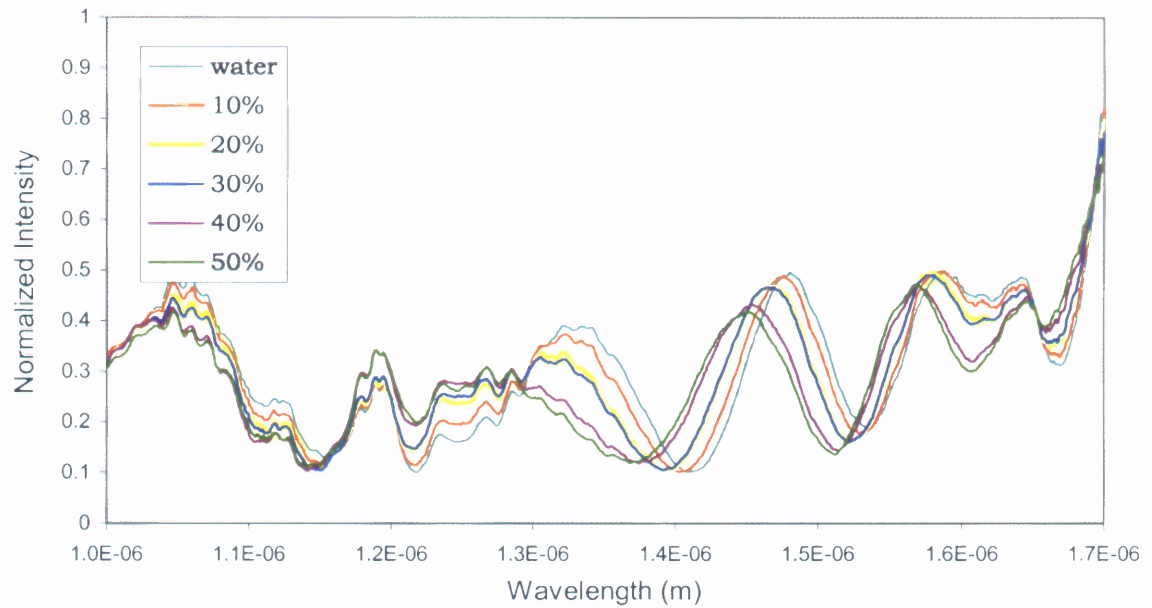


Figure 5.24 Experimental results of methanol on a 6 μm MZI waveguide sensor with 8 mm arm length.

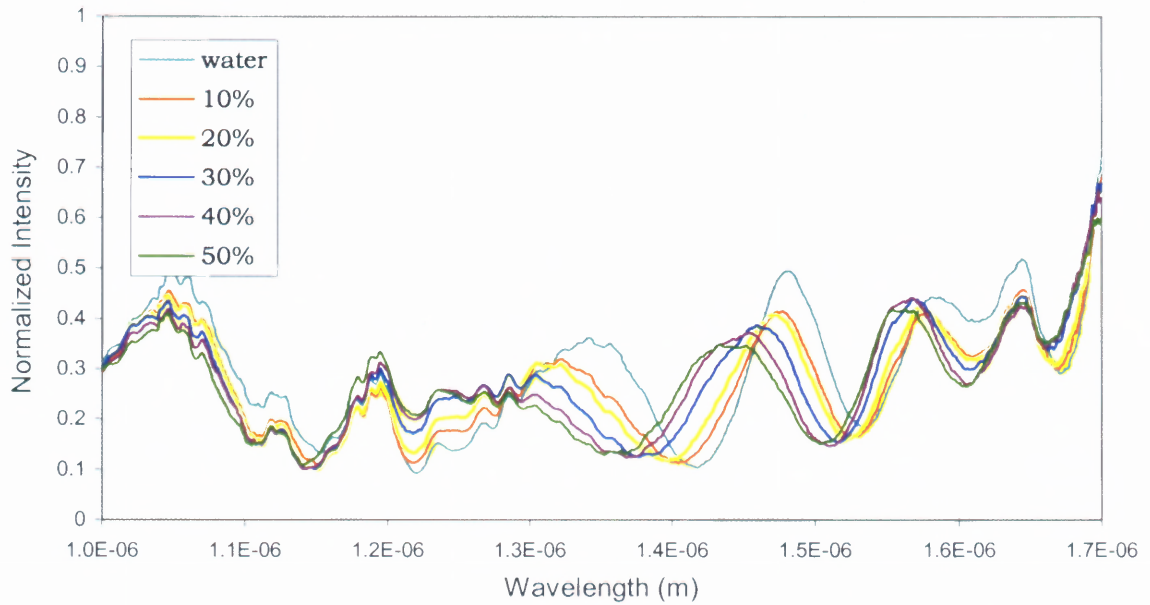


Figure 5.25 Experimental results of methanol on a 6- μm MZI waveguide sensor with 10 mm arm length.

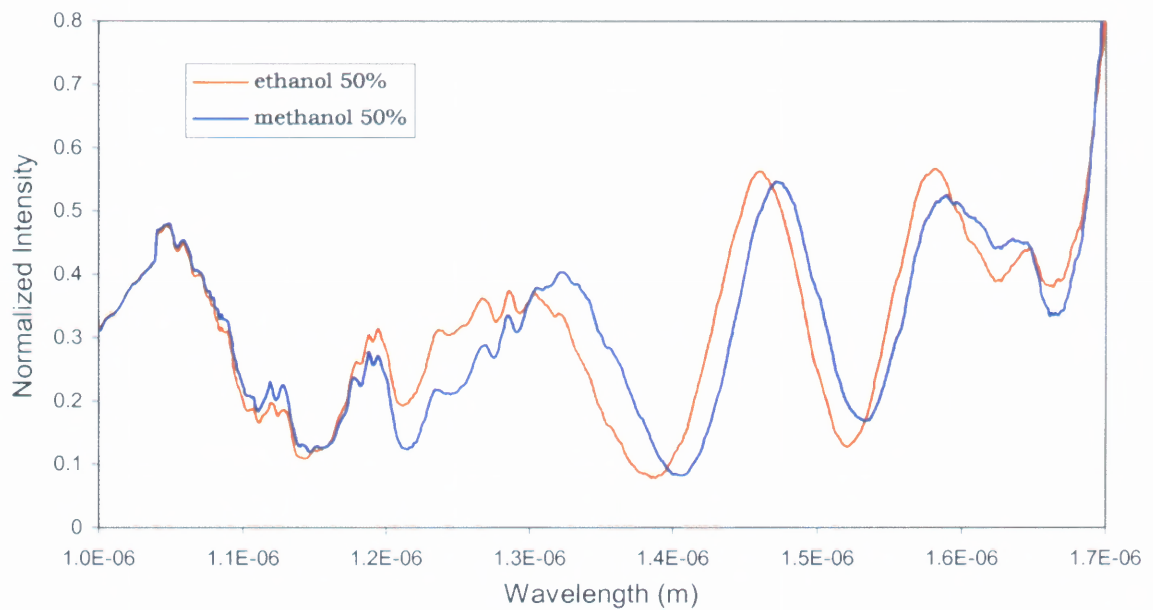


Figure 5.26 Comparison between the experimental results of 50% concentration of ethanol and 50% concentration of methanol on a 5 μm MZI waveguide sensor with 8 mm arm length.

Several measurements were made for an interval of 50 seconds with the water covered the sampling arm of the sensor. The output spectra of the measurements overlapped with each other showing that the results were repeatable, as shown in Figure 5.27. The results show that the wavelength peak does not shift over the time. This means that the sampling arm reached its equilibrium state in less than a minute, or the chemical interaction with the waveguide core is instantaneous, and the data is time independent in a short duration of time. The intensity, however, slightly decreased after several moments. This is because of the instability of the experiment apparatus used for the fiber-to-waveguide coupling.

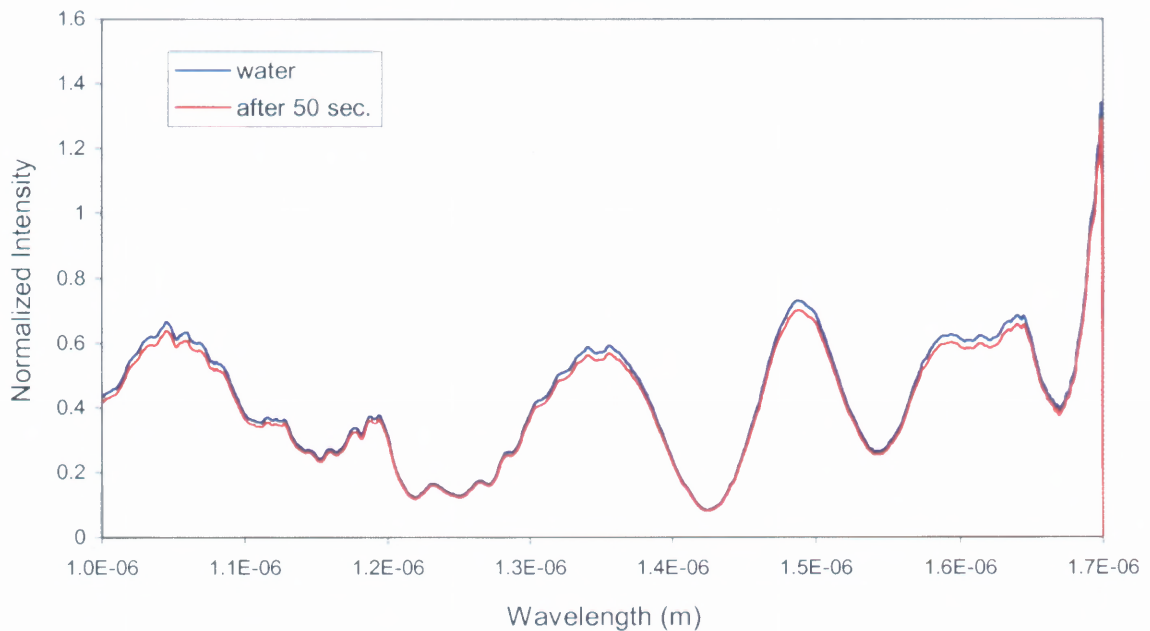


Figure 5.27 Output spectra of water before and after 50 seconds.

Several plots of normalized intensity vs. concentration of methanol based on the experimental data at 1420 nm, 1460 nm, and 1480 nm wavelengths from Figure 5.23 are shown in Figure 5.28. Notice that it is a positive slope at 1420 nm and a negative slope at

1480 nm, while it's fairly flat at 1460 nm. This means that the sensor is sensitive at 1420 nm and 1480 nm wavelengths but not at 1460 nm wavelength for this case. The sensitivity S_m can be determined by

$$S_m = \frac{\Delta\phi}{\Delta M} \approx \frac{\Delta I_N}{\Delta M} \quad (5.2)$$

since $\Delta I_N \approx \cos(\Delta\phi) \approx \sin(\Delta\phi) \approx \Delta\phi$ if λ is chosen so that $\Delta\phi = \pi/2$, where $\Delta\phi$ is the phase shift, ΔI_N is the normalized intensity difference and ΔM is the change in chemical concentration. The term $\Delta I_N / \Delta M$ is actually the slope of the normalized intensity versus concentration. Hence the sensitivity of this particular sensor at 1420 nm is around 0.0044 and at 1480 nm is around 0.0038. The minimum detectable concentration C_{\min} is then verified from

$$C_{\min} = \frac{\text{error}}{S_m} \quad (5.3)$$

From the error bar provided by the standard deviation shown in Figure 5.28, the error is 0.035 for the plot at 1420 nm. Thus, the minimum detectable concentration is 7.95%, while at 1480 nm with error = 0.03, the minimum concentration detectable is 7.89%. In other words, the sensor will not response to the ethanol with less than 8% of concentration of ethanol in water. The minimum detectable concentration can be improved as discussed in the discussion section since the integrated MZI is expected to be able to detect in low ppm range, while the 8% of ethanol is equivalent to 63,200 ppm.

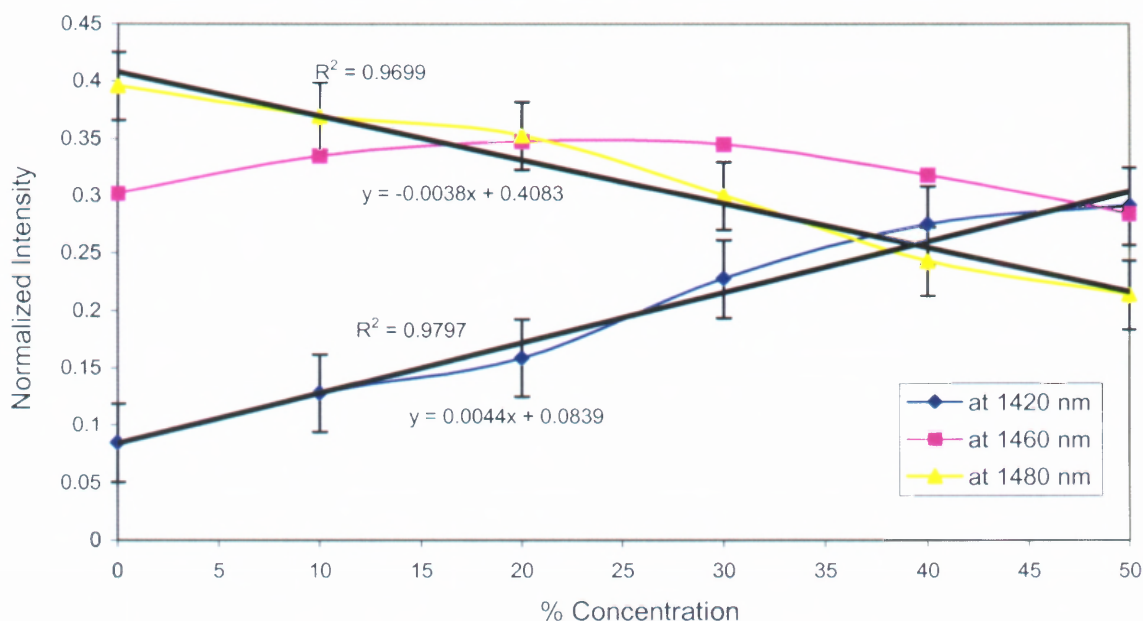


Figure 5.28 Normalized intensity vs. concentration of methanol based on the experimental data at 1420 nm, 1460 nm, and 1480 nm wavelengths from Figure 5.23.

5.3.2 1.5 μm Broadband Source

The experimental procedures were repeated using the 1.5 μm broadband source. The broadband source has wavelength ranging from 1520 nm to 1580 nm as depicted in Figure 4.3. It is expected that the sensor have higher sensitivity in this wavelength range since (from previous results shown in Figure 5.20 to Figure 5.26) the intensity spectra with respect to the corresponding concentration of chemical show more significant variations from the water compare to other wavelength regions. Thus, an experiment was performed on the 5 $\mu\text{m} \times 10$ mm sensor with different concentration of ethanol, and the results are shown in Figure 5.29.

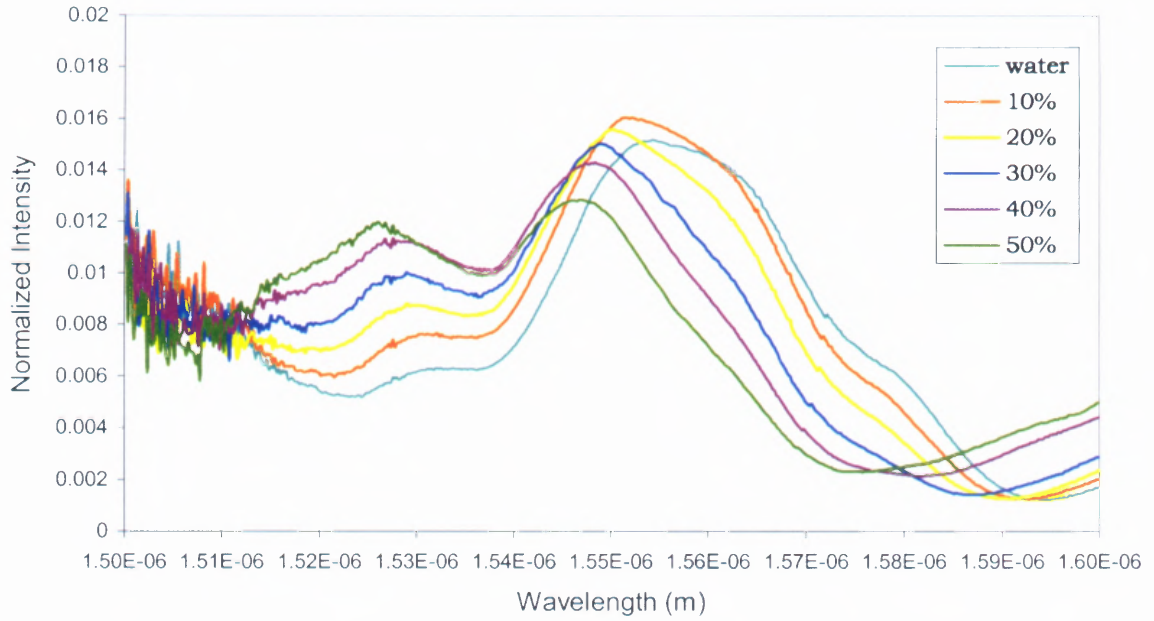


Figure 5.29 Experimental results showing the interference spectrums shifted corresponding to the various concentration of methanol on a 5 μm MZI waveguide sensor with 10 mm arm length using 1.5 μm broadband source.

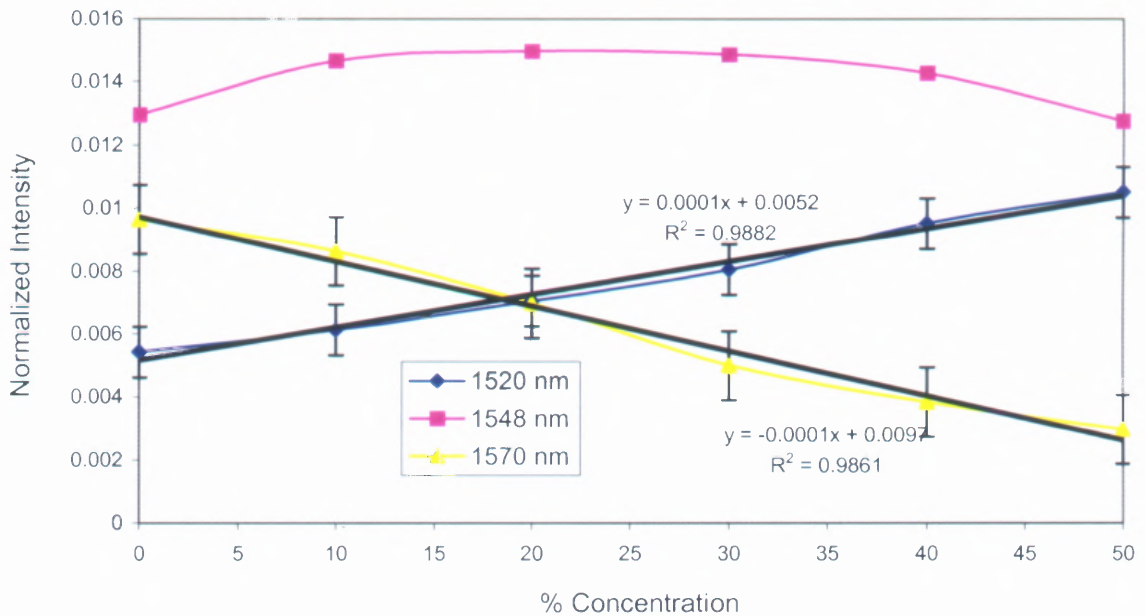


Figure 5.30 Normalized intensity vs. concentration of ethanol based on the experimental data at 1520 nm, 1548 nm, and 1570 nm wavelengths from Figure 5.28.

The intensity varies linearly with the concentration at wavelength around 1520 nm and 1570 nm as shown in Figure 5.30. This means that the sensor is sensitive at 1520 nm and 1570 nm but not at 1548 nm for this case. The sensitivity of this particular sensor is the slope of the plot, which is around 0.0001 at 1520 nm and at 1570 nm. From equation (5.3), the minimum concentration detectable for this case is $C_{\min} = 0.001 / 0.0001 = 10\%$, which means that this sensor becomes less sensitive to the chemical of 10% or lower concentration, when 1.5 μm broadband source is used.

5.4 Discussion

The ratio of the propagation constant β to the wavenumber k is called the *effective index*, n_{eff} , represented by

$$n_{\text{eff}} = \frac{\beta}{k} \quad (5.4)$$

Hence the normalized propagation constant of equation (3.93) can be expressed as

$$b = \frac{n_{\text{eff}}^2 - n_{\text{clad}}^2}{n_{\text{core}}^2 - n_{\text{clad}}^2} \quad (5.5)$$

When $n_{\text{eff}} < n_{\text{clad}}$, the electromagnetic field in the cladding becomes oscillatory along the transverse direction; i.e., the field is dissipated as the radiation mode into the buffer layer and top cladding, for which case, $b < 0$. In the case for $b > 1$, higher order modes occur. This means that for each mode field, they have their own set values of $0 \leq b \leq 1$, as shown in Figure 5.1 and Figure 5.14.

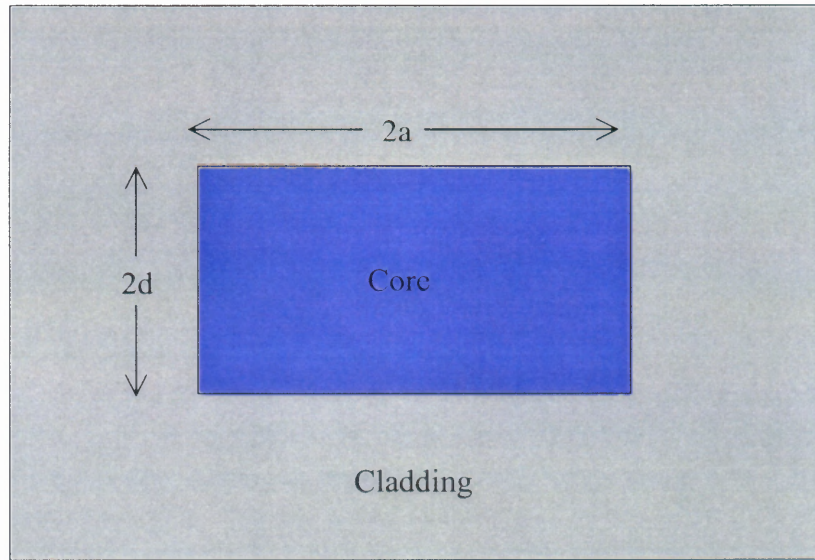


Figure 5.31 Schematic of a buried channel waveguide structure.

The calculated cutoffs for TM modes by the Marcattili's approximation are of big difference compare to that by finite element method. The analytical cutoff is $5\text{ }\mu\text{m}$ while the numerical is $1.9\text{ }\mu\text{m}$. The difference is due to the fact that the Marcattili's treatment is more accurate when deal with a waveguide configuration as shown in Figure 5.31, which is the buried channel waveguide with thick cladding surrounded the waveguide core, while for the integrated MZI sensor, the waveguide structure has much thinner cladding covers only the three sides of the waveguide. Such complicated waveguide will need a more sophisticated method, i.e. the finite element method, to solve the eigenvalues.

As for the ridge waveguide simulation using FEM or other numerical approaches, most of the publications^{52,53} were specified on the waveguide structure as shown in Figure 5.32, which is quite different from the waveguide designed for the integrated MZI

sensor. This type of ridge waveguide has less complexity compare to the waveguide designed for the integrated Mach-Zehnder Interferometer sensor in this dissertation. Thus, this unique and complicated waveguide structure has contributed to the big different between the analytical and numerical solutions.

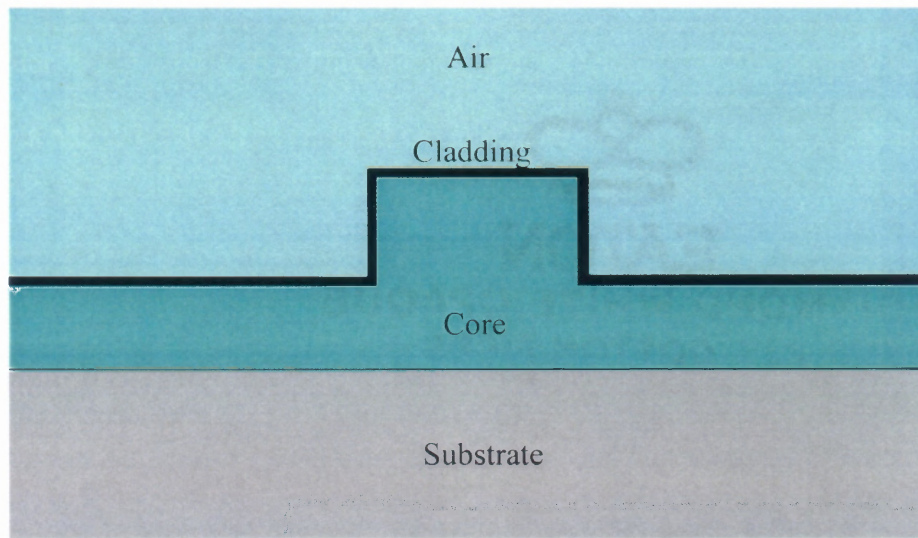


Figure 5.32 Schematic of a ridge waveguide structure.

The cutoff value of the fundamental mode calculated by the FEM shows agreement with the experimental results. For example, the cutoff wavelength of the first order mode from Figure 5.20 is 1640 nm, where the output intensity does not show interference beyond the cutoff. The agreement from the experimental value is also shown in Figure 5.33 where the interference occurs after 1100 nm wavelength, which is the second order mode cutoff. By other means, the wavelength of the source used for the experiments has to be in between 1100 nm and 1640 nm so that single mode propagation

can be maintained in the reference and sampling arms because interference happened during the superposition of two single modes.

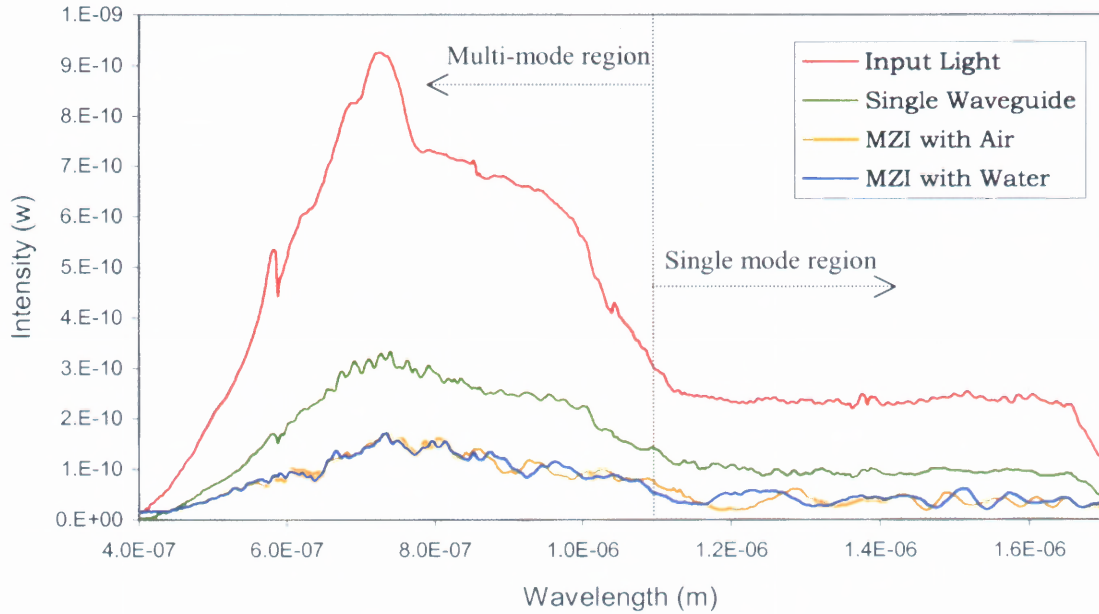


Figure 5.33 Comparison among the output profiles of the integrated MZI sensor, the single waveguide and input light profiles.

The sensitivity calculated from Section 5.3 shows that there is a factor of 40 difference between the cases with the white light source and the 1.5 μm broadband source. Since the sensor sensitivity is independent of the effect due to the total power loss in the waveguide, the compensated sensitivity to the error can be estimated as

$$S'_m = S_m / \delta I_N = 0.004 / 0.3 = 0.013 \text{ per \%ml}$$

for the sensor using white light source, where δI_N is the difference between the maximum and minimum normalized intensity obtained from Figure 5.23. The estimated sensitivity for the sensor using 1.5 μm broadband source is 0.007 with $S_m = 0.0001$ and

$\delta I_N = 0.014$ determined from Figure 5.29. The sensitivity of the two cases becomes a factor of 2 difference after eliminating the power losses from the calculation.

Another approach used to calculate the sensor sensitivity is to determine the wavelength at the peak of spectra as a function of the change of refractive index from water. The sensitivity is defined as

$$S_\lambda = \frac{\Delta\lambda_{peak}}{\Delta n} \quad (5.6)$$

where $\Delta\lambda_{peak}$ is the wavelength at the peak of the spectra and Δn is the difference of the refractive index of the concentration of ethanol from water. A plot of the peak wavelength versus the index difference is shown in Figure 5.34, with the data obtained from Figure 5.23.

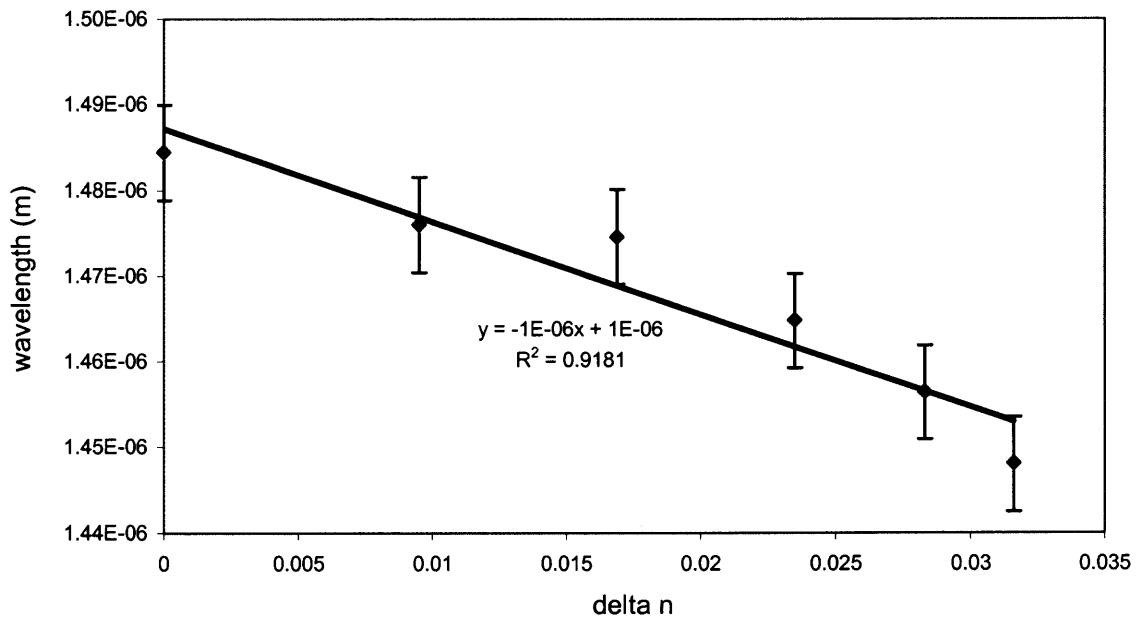


Figure 5.34 Peak wavelength versus refractive index difference of ethanol from water.

The sensitivity in terms of wavelength is the slope of the plot, which is $1 \mu\text{m}/\text{unit}$ index change for the $5 \mu\text{m} \times 10 \text{ mm}$ with white light source. The minimum detectable concentration is then defined by

$$C_{\min} = \frac{\text{error}}{S_{\lambda}} \quad (5.7)$$

with the error = $0.006 \mu\text{m}$ determined from the plot, the minimum detectable concentration is 0.6% of ethanol. This corresponds to about 4740 ppm. Note that this minimum detectable concentration is about a factor of 10 smaller than that obtained with intensity changes with concentration.

The experimental results using different concentration of chemical have proven that the sensor is sensitive to the refractive index changed on the sensing/sampling arm with respect to the wavelength variation. Notice that for all the intensity modulation results, the destructive interference is not at zero, which means that there is an offset value for the interference. This offset value is affected by the fringe visibility factor V ⁴⁹, which depend on the input and output Y-junctions spitting ratios and the losses in the sampling and reference arms of the integrated Mach-Zehnder Interferometer sensor. This factor can be related to the equation (2.4), and is expressed as

$$\frac{I_x}{I_o} = \frac{1}{2} \left[1 + V \cos \frac{2\pi L F}{\lambda} (n_{\text{chem}} - n_{\text{water}}) \right] \quad (5.8)$$

where n_{chem} and n_{water} are the refractive index of the chemical and water, respectively; L is the arm length and F is the waveguide index conversion factor,⁵⁴ which is also the curve fitting value of the phase shifting. The fringe visibility can be estimated by

$$V = \frac{I_{\text{ref}} - I_{\text{samp}}}{I_{\text{ref}} + I_{\text{samp}}} \quad (5.9)$$

where the I_{ref} and I_{samp} are the output intensities of the reference arm and sampling arm of the Y-junction, respectively. The fringe visibility is between 20% and 32% in the wavelength ranging from 1300 nm to 1500 nm, for the $6\ \mu\text{m} \times 10\ \text{mm}$ sensor. Note that the fringe visibility will have different value for different interferometers. The data of the fringe visibility as a function of wavelength calculated from experimental data of Figure 4.6 for $6\ \mu\text{m} \times 10\ \text{mm}$ waveguide sensor is shown in Figure 5.35.

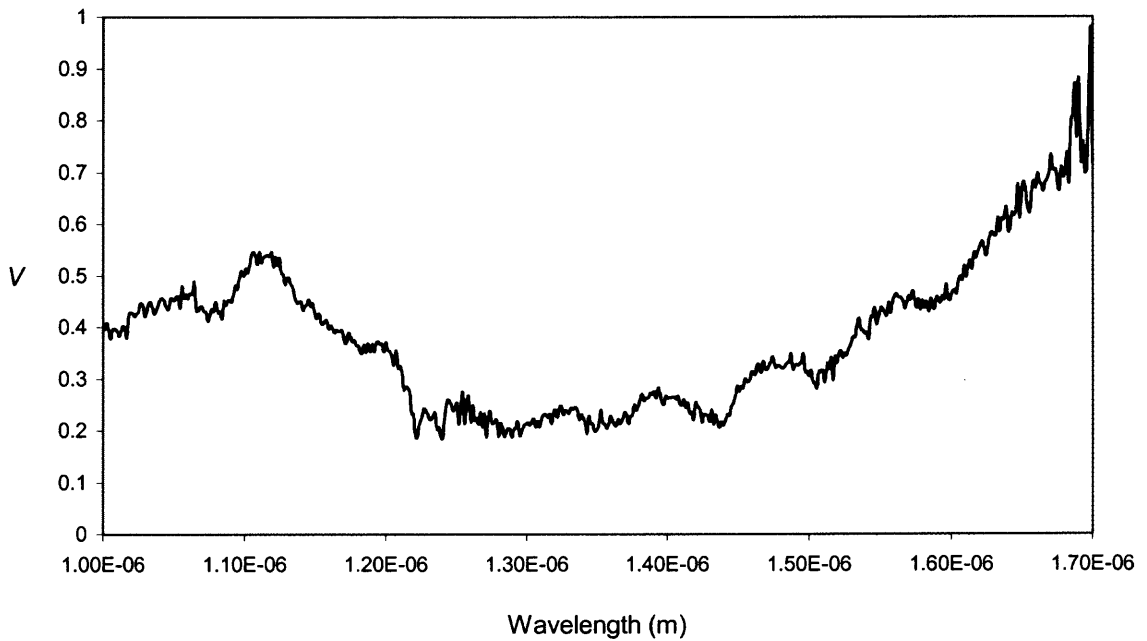


Figure 5.35 Fringe visibility as a function of wavelength.

The theoretical value of the normalized intensity calculated using equations (5.8) and (5.9) is shown in Figure 5.36, with the fringe visibility obtained from Figure 5.35, and $L = 10\ \text{mm}$. The n_{chem} for 50% of ethanol is 1.3616 and the refractive index of water can be obtained from the CRC Handbook, i.e.

$$n_{water} = \left(\frac{3.113 \times 10^3}{\lambda^2} \right) + 1.3246 - (1.8791 \times 10^{-6}) (T^2) \quad (5.10)$$

where T is the room temperature. The factor F is the estimated theoretical curve fitting value, which is also wavelength dependent. In this case, the factor F is estimated as

$$F = 0.096 - 2\lambda^4$$

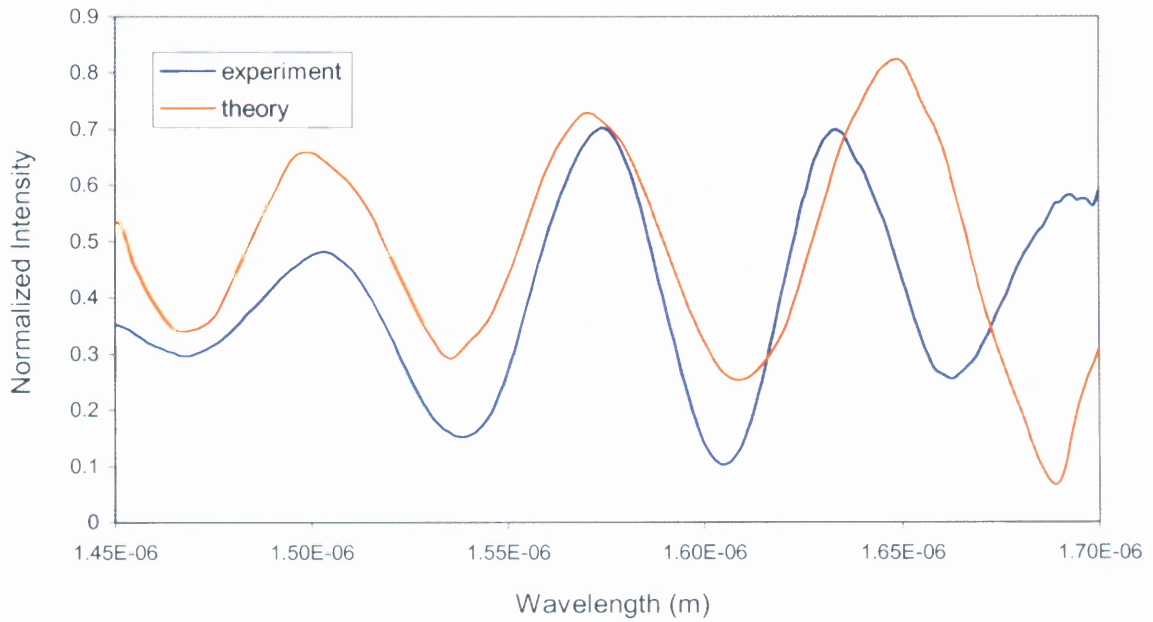


Figure 5.36 Comparison between the experimental result and theoretical data.

This factor will have different values for different waveguides. The offsets between the experimental result and the theoretical data are mainly due to the power loss in the Y-splitter; the possibility of mode leakage into the buffer layer; and scattering loss in the waveguides material.

The sensitivity obtained from the experimental results of Figure 5.28 and Figure 5.30 for the white light and 1.5 μm broadband sources varies from 8% to 10%. This means that the sensors will not response accurately to a 10% or less of concentration difference. This may explain why the experimental results listed in Section 5.3 for the white light source exhibit an inconsistent shifting for each 10% increment in concentration. The integrated Mach-Zehnder Interferometer sensor is expected to be

sensitive in ppm (parts per million) range of concentration difference. However, the experimental results show otherwise, and this is mainly due to the fiber-to-waveguide coupling inefficiency. The fiber, which is butt-coupled to the waveguide, is susceptible to movement from vibrations, air currents, or sagging/ creep of the positioning stages. This problem can be improved by stabilizing the whole fiber-waveguide system with the fiber set on a V-groove connected to the waveguide,⁵⁵ as depicted in Figure 5.37

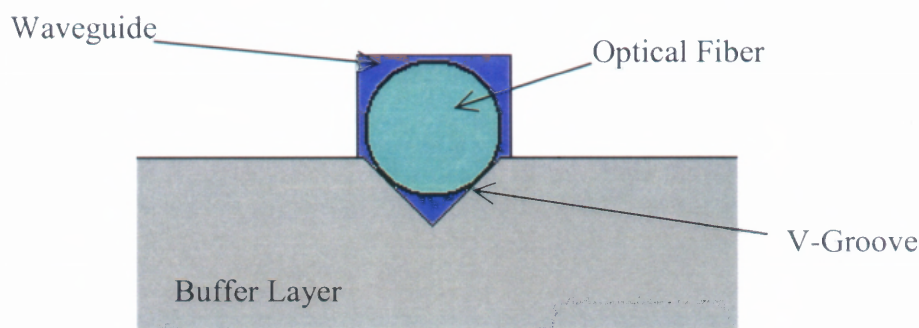


Figure 5.37 Schematic of a V-groove for stabilizing the optical fiber.

The setup system can be stabilized when the chemical is *flowing* constantly through the sensor. This can be achieved by adhered a flow cell on top of the sensor as depicted in Figure 5.38. By connecting the flow cell with piping and a mechanical pump, the chemical can be directed through the sensor in a steady flow to minimize vibration on the end coupling system. Together with a lock-in amplifier for output measurement, the minimum detectable concentration can be improved up to 1000X. For example, the minimum detectable concentration calculated from the experiment is 10% (intensity variation method) of ethanol, which is equivalent to 79,000 ppm. The estimated minimum detectable concentration after the improvement is 79 ppm.

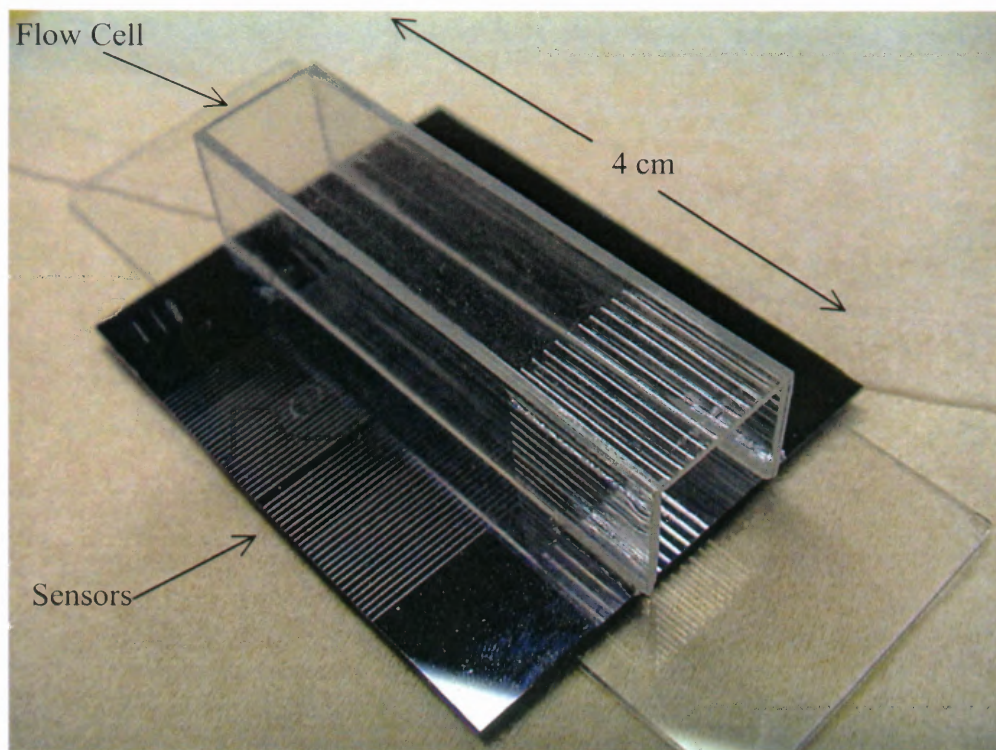


Figure 5.38 A 4 cm long flow cell adhered on top of a sample with two dies of integrated MZI sensors.

5.5 Anticipated Vision

Since the integrated MZI sensor exhibits the sensitivity to the different chemicals in the broadband wavelength range, it can be implemented into a chemical selective device if integrated with a wavelength tunable laser diode. Different chemical species have their individual *fingerprint* spectra, which depend on absorption of particular wavelengths. Therefore, by transmitting consecutive steps of single wavelength of a broadband source through the sensor, the output spectrum will be able to reveal which chemical species appears in the solution by matching the result to the *fingerprint* spectra.

From Figure 5.28 and Figure 5.30, which show the normalized intensity changes with the % of concentration difference, the sensor exhibits its sensitivity only at certain

wavelength range. In other words, the sensor will not respond to a chemical species that has absorption at the wavelength range where the sensor is not sensitive. Thus, for future implementation, a phase modulator⁵⁶ can be integrated on the reference arm so that the sensitivity range of the sensor can be tuned to coincide with the chemical absorption range.

Selectivity can also be achieved by having a micro-concentrator integrated with the Marc-Zehnder Interferometer as shown in Figure 5.39. The polymer layer inside the chamber attracts chemical in a very low concentration for duration of time and releases the chemical in a higher concentration for the sampling arm detection when the temperature of the micro-concentration is increased. With the idea of selectivity using different polymer for different chemical attraction, an array of the Mach-Zehnder Interferometer sensors can be fabricated to form a multi-channel chemical selectivity device as depicted in Figure 5.40. Each channel of the micro-concentrator will response to a certain chemical and the output spectra will act like the *fingerprint* for a particular chemical.

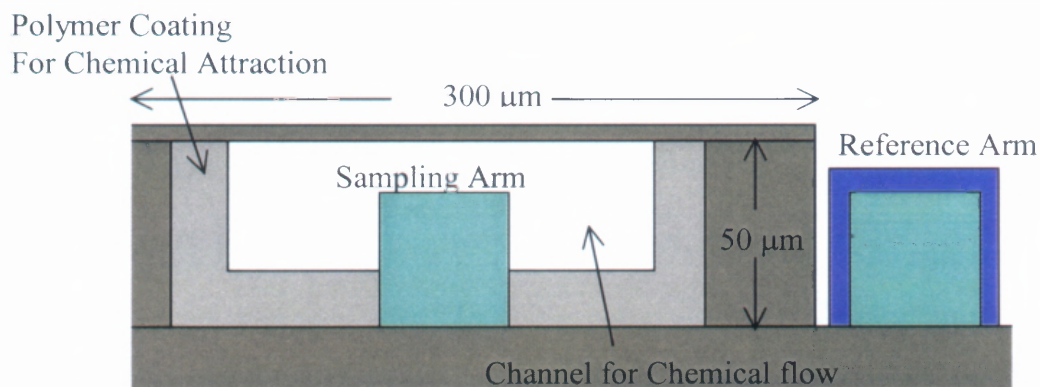


Figure 5.39 Schematic of a Micro-Concentration integrated with MZI.

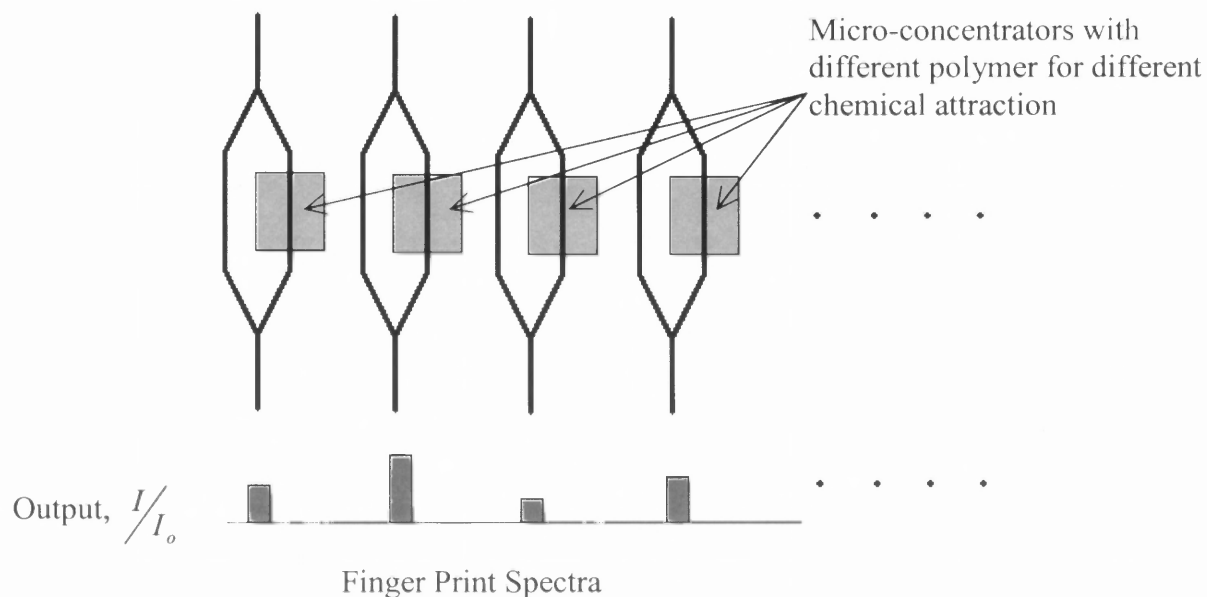


Figure 5.40 Schematic of a multi-channel chemical selectivity device.

In the future, the design of the integrated optical waveguides will be more straightforward and effortless with the computational method presented in this dissertation. The changing of the waveguide materials or doping materials can be simulated according to the specific applications such as lithium niobate waveguide used for sensing electric field,²³ or erbium doped waveguide used in waveguide amplifier.^{57,58} The numerical method is also efficient in calculating the power loss in the waveguides by updating the technique into three-dimensional method.

The computational design of the integrated optical waveguides can be implemented to waveguide laser or amplifier simulation using three-dimensional FEM. Further simulation can also be applied to the Y-junction using FE-BPM, i.e. finite

element beam propagation method, which integrates the two novel numerical/simulation methods to simulate the mode propagation along the variant z-axis (which is invariant in the two-dimensional case), and the power loss/gain as the light transmitting through the waveguide.

5.6 Summary

- A theoretical study on the integrated optical waveguide has been presented in both the analytical and numerical approaches. The analytical method used is the Marcatili's approximation while the numerical method employed is the finite element method (FEM). The Marcatili's approximation is the simplest among other analytical methods and hence is not accurate when applied to complicated waveguides as designed for this project. On the other hand, the FEM is the most complicated technique among the numerical methods, and thus the cutoff results calculated show agreement with the experimental results. Moreover, the numerical method has been proved to be able to simulate the electromagnetic fields propagating through the waveguides with various design parameters.
- Due to the failure of the first generation sensors, the re-fabricated second generation integrated MZI sensors were subjected to a series of testing processes to ensure the sensor functionality before further experiments were performed.
- Experiments were performed using white light and 1.5 μm broadband sources with different concentrations of ethanol and methanol. Results show that the output intensity varied with respect to wavelength and the spectrum shifted in accordance with different concentrations of the chemicals. The sensitivity of the sensor is also

determined from the plot of intensity versus concentration, which is around $0.013 (\% \text{ml})^{-1}$ and $0.007 (\% \text{ml})^{-1}$ for the white light source and the $1.5 \mu\text{m}$ broadband source, respectively. The lowest detectable concentration of ethanol for the sensor detection is 8%.

- The experimental results agree with the theoretical data with minor offset due to the unbalanced power split by the Y-splitter, and power loss due to scattering by the waveguide materials and mode leakage into the substrate.

APPENDIX A

FABRICATION PROCEDURES FOR THE INTEGRATED MZI

Wafer Preparation

1. Clean wafer (primary), M-Proyl, Temp: 95°C 10 min.
2. Clean wafer (secondary), M-Proyl, Temp: 95°C 10 min.
3. Cold DI Rinse 10 min.
4. Spin Dry.

Buffer Layer and PSG Deposition

1. LPCVD of SiO₂, Gas: O₂/Diethylsilane, Thickness: 15 μm, Temp: 775°C, Time: 20 hrs.
2. LPCVD of PSG, Gas: O₂/Trimethylphosphite/Diethylsilane, Thickness: 7 μm, Temp: 600°C, Time: 5 hrs.

PCG Etch-Back and First Sputter

1. RIE (Reactive Ion Etching) etch to ~ 5.5 μm, 25 sccm CF₄.
2. DC-Sputtering AL/0.5% Cu, Thickness: 2000Å

Photolithography (Waveguide Layer)

1. Photoresist Deposition, Thickness: 2 μm, Time: 20 sec.
2. Hot Plate, Temp: 110°C, Time: 1 min.
3. Cold Plate, Temp: 18°C, Time: 30 sec.
4. Exposure to UV, Time: 18 sec.
5. Apply Developer, Time: 30 sec.

6. Apply Developer, Time: 1 min.
7. DI Rinse.
8. Spin to remove water.
9. Hard Baking, Temp: 115°C, Time: 1 min.
10. Cold Plate, Time: 1 min.

Aluminum Etch Mask

1. Al Etch, Etchant: $\text{HNO}_3/\text{HOAC}/\text{H}_3\text{PO}_4$, Temp: 40°C, Time: ~20 sec., Etch Rate: ~2700 Å/min.
2. Cold DI Rinse, Time: 10 min.
3. Spin Dry.
4. Photoresist Strip (primary), M-Proyl, Temp: 95°C, Time: 10 min.
5. Photoresist Strip (secondary), M-Proyl, Temp: 95°C, Time: 10 min.
6. Cold DI Rinse, Time: 10 min.
7. Spin Dry.

Etch of PSG Waveguide Cores and Removal Al Etch Mask

1. RIE (Reactive Ion Etching), 25 sccm CF_4 , Temp: 25°C, 250 watts, 750 mTorr.
2. Al Etch, Temp: 40°C, Time: ~20 sec., Etch Rate: ~2275 Å/min.
3. Cold DI Rinse.
4. Spin Dry.

Waveguide Core Anneal and Cladding Deposition

1. Anneal Waveguide Cores, Temp: 1050°C, Gases: 7.5 slpm N_2 and 0.5 slpm O_2 .
Time: 1 hr.

2. PECVD of SiO₂, Gas: O₂/Diethylsilane, Thickness: 1 μm, Temp: 250°C, Time: 30 min.

Second Al Sputter

1. DC-Sputtering Al/0.5% Cu, Thickness: 2000 Å.

Repeat Steps

1. Photolithography for Window Layer
2. Aluminum Etch Mask

Etch of Windows in SiO₂ and Removal of Al Etch Mask

1. RIE (Reactive Ion Etching), 25 sccm CF₄, 25 sccm CHF₃, Temp: 25°C, 250 watts, 750 mTorr.
2. Al Etch, Temp: 40°C, Time: ~20 sec., Etch Rate: ~2275 Å/min.
3. Cold DI Rinse, Time: 10 min.
4. Spin Dry.

APPENDIX B

FEM GLOBAL MATRIX ASSEMBLY TABLES

Node Location Table

A listing of all meshes nodes using global numbers and their corresponding (x, y) coordinates. This table specifies the geometry of the input configuration, as shown in Table A.1.

Triangle Connectivity Table

This table gives the global nodes comprising each triangle. For example, by referring to Figure 3.5, element #3 ($e = 3$) is formed by nodes 2, 3, and 7, as given in line 3 of table A.2. The table defines three arrays, which provides the correspondence between local node number of e^{th} element and the global nodes.

Boundary Element Table

To impose the boundary conditions it is necessary to identify the surface edges on the outer boundary of the mesh and their associated nodes. This table can be generated using the data in the previous two tables. The data manipulations required to generate the surface node and element information is typically part of the data preprocessor and is an important step before assembling the final system. An example of such a boundary element table is given in Table A.3. The listed arrays provided the correspondence between the local surface element nodes and the global.

Table A.1 Node location table for matrix assembly

Global node #	x	y
1	0	0
2	3.33E-06	0
3	6.67E-06	0
4	1.00E-05	0
5	0	3.33E-06
6	3.33E-06	3.33E-06
7	6.67E-06	3.33E-06
8	1.00E-05	3.33E-06
9	0	6.67E-06
10	3.33E-06	6.67E-06
11	6.67E-06	6.67E-06
12	1.00E-05	6.67E-06
13	0	1.00E-05
14	3.33E-06	1.00E-05
15	6.67E-06	1.00E-05
16	1.00E-05	1.00E-05

Table A.2 8-element triangular connectivity data for matrix assembly

Element # e	Local Node arrays		
	n(1,e)	n(2,e)	n(3,e)
1	1	2	6
2	1	6	5
3	2	3	7
4	2	7	6
5	3	4	8
6	3	8	7
7	5	6	10
8	5	10	9
9	6	7	11
10	6	11	10
11	7	8	12
12	7	12	11
13	9	10	14
14	9	14	13
15	10	11	15
16	10	15	14
17	11	12	16
18	11	16	15

Table A.3 Boundary element connectivity table

Surface Edge Number s	Local Node Arrays	
	$n_s(1, s)$	$n_s(2, s)$
1	6	4
2	4	1
3	1	2
.	.	.
.	.	.
.	.	.

Material Group Table

In practice, the same material covers sections of the domain and it is not necessary to specify the material parameters for each individual element. Instead, one may choose to attach a material code column to the element connectivity table. That is, the material of each element is specified through the “code” which is in turn associated with specific values of ε_r and μ_r .

The first two of the above tables are always required but the latter two may or may not be needed depending on the application at hand.

APPENDIX C

ONE-DIMENSIONAL FEM CODE

Listing of one-dimensional FEM program for one-dimensional Sturm-Liouville second order differential equations.

```
%FEM program written in MATLAB code to solve one dimensional
differential equation
%xa=location of the left computational domain endpoint
%p=p coefficient appearing in the differential equation
%q=coefficient appearing in the differential equation
%N=number of nodes
%E_FEM=computed electric field
%E_exact=exact analytical solution

% Initialization
clear;
N=11;
p=1;
q=pi^2;
xa=1;

% Initialize global matrix and vector
for m=1:N,
    b(m,1)=0;
    E_exact(m,1)=0;
    for n=1:N,
        A(m,n)=0;
    end;
end;

% Compute element matrices and assemble global matrix
for n=1:N-1,
    xe1=(n-1)*xa/(N-1);
    xe2=n*xa/(N-1);

    Ael(1,1)=p/abs(xe2-xe1)+q*abs(xe2-xe1)/3;
    Ael(2,2)=Ael(1,1);
    Ael(1,2)=-p/abs(xe2-xe1)+q*abs(xe2-xe1)/6;
    Ael(2,1)=Ael(1,2);
    bel(1,1)=(abs(xe2-xe1)/6)*(2*hcurv(xe1)+hcurv(xe2));
    bel(2,1)=(abs(xe2-xe1)/6)*(2*hcurv(xe2)+hcurv(xe1));

    A(n,n)=A(n,n)+Ael(1,1);
    A(n,n+1)=A(n,n+1)+Ael(1,2);
    A(n+1,n)=A(n+1,n)+Ael(2,1);
    A(n+1,n+1)=A(n+1,n+1)+Ael(2,2);

    b(n,1)=b(n,1)+bel(1,1);
    b(n+1,1)=b(n+1,1)+bel(2,1);
end
```

```

% Enforce boundary conditions
A(1,1)=1;
for n=2:N,
    A(n,1)=0;
    A(1,n)=0;
end;

for n=1:N,
    A(n,N)=0;
    A(N,n)=0;
end;

A(N,N)=1;
b(1,1)=0;
b(N,1)=0;

% Solve the resulting NxN system
E_FEM=inv(A)*b;

% Compute exact solution
for n=1:N;
    E_exact(n,1)=sin(pi*(n-1)*0.1);
end;

% End of program

%subfunction for 1D FEM
function value = hcurv(x)
value = 2*(pi^2)*sin(pi*x);

%end of subfunction

```

APPENDIX D

FEM TM AND TE FIELDS FOR AIR

The following is the Finite Element Method for solving the Transverse Magnetic and Transverse Electric field modes written in Matlab codes for air or with the users' specified dielectrics filled waveguides, and the total number of element.

```
%This FEM MATLAB code can be used to solve for the TM and TE modes of
%the air or uniform dielectric filled square waveguides
%k0=free space propagation constant
%xa=location of the left computational domain endpoint
%p=p coefficient appearing in the differential equation
%q=coefficient appearing in the differential equation
%N=number of nodes (N-1=number of layers)
%E_FEM=computed electric field (to be plotted)
%E_exact=exact analytical solution across the squares waveguide

% Initialization
clear all;
clc;

%diary file1;
cut= input('# of Blocks?[integer only]: ');
N_elements=2*(cut*cut);
total_global_num=(cut+1)^2;
lambda=1; %cm

% Initialize global matrix and vector
for m=1:N_elements,
    gamma_TE_exact(m,1)=0;
    gamma_TM_exact(m,1)=0;
    error(m,1)=0;
end

% Compute element matrices and assemble global matrix
% Generation of the Node Connectivity Table:
% =====
str = int2str(cut);
filename=strcat('nodeconnectivitydata',str,'.txt');

fid = fopen(filename,'w');
if cut==1;
    sk=0;
end;

for skipnum=1:(cut-1);
    sk(1,skipnum)=(cut+1)*skipnum; % generating skip edges
end;
```



```

for aa=1:((cut^2)+(cut-1));
    if rem(aa,(cut+1)); % generating table without edges
        fprintf(fid,'%g \t %g \t %g\n',aa,aa+1,aa+cut+2);
        fprintf(fid,'%g \t %g \t %g\n',aa,aa+cut+2,aa+cut+1);
    else
        % skipped edges
    end
end;

status = fclose(fid);
fid = fopen(filename,'r');
n_a = fscanf(fid,'%g %g %g',[3 inf]); % It has rows now.
status = fclose(fid);

mu=ones(1,N_elements);
eps=ones(1,N_elements);
ko=2*pi/lambda;
a=1.5;
b=a/2;

for e=1:N_elements;
    n(1,e)=n_a(1,e);
    n(2,e)=n_a(2,e);
    n(3,e)=n_a(3,e);
end;

filename=strcat('nodelocationdata',str,'.txt');
fid = fopen(filename,'w');

if cut==1;
    cc=0;
    fprintf(fid,'%g \n',cc); % generating center node for TM
end;

for cc=sk;
    for i=1:cut-1
        cc=i+1;
        fprintf(fid,'%g \n',cc+i+1); % generating center node for TM
    end;
end;

status = fclose(fid);
fid = fopen(filename,'r');
TM_n = fscanf(fid,'%g' ,[1 inf]); % It has 1 row now.
status = fclose(fid);

non_cond=TM_n(1,:);

% Nodes locations table:
%=====
filename=strcat('nodelocationdata',str,'.txt');
fid = fopen(filename,'w');

for bb=0:b/(cut):b;
    for aa=0:a/(cut):a;
        fprintf(fid,'%g \t %g\n',aa,bb); % generating coords
    end;
end;

```

```

end;

status = fclose(fid);
fid = fopen(filename, 'r');
l_a = fscanf(fid, '%g %g' , [2 inf]); % It has 2 rows now.
status = fclose(fid);
xnodes=l_a(1,:);
ynodes=l_a(2,:);

%Initialization Process:
%=====
A=zeros(total_global_num);
Kdel=zeros(total_global_num);
K=zeros(total_global_num);
Kedel=zeros(3);

%Loop through all elements:
%=====
for e=1:N_elements;

%E_z/TM polarization :
%=====
    pe=1/mu((e));
    qe=eps((e));

% H_z/TE polarization :
% =====
    pe=1/eps((e));
    qe=mu((e));

% Coordinates of the Element nodes:
%=====
for i=1:3;
    x(1,i)= xnodes(1,n(i,e));
    y(1,i)= ynodes(1,n(i,e));
end;

% Compute the Element matrix entries:
%=====
Area=.5*abs((x(2)-x(1))*(y(3)-y(1)) - (x(3)-x(1))*(y(2)-y(1)));

for i=1:3;
    i1=0;
    if i==3;
        i1=3;
    end;
    ip1=(i+1)-i1;
    i2=0;
    if ip1==3;
        i2=3;
    end;
    ip2=ip1+1-i2;
    bi=y(ip1)-y(ip2);
    ci=x(ip2)-x(ip1);

for j=1:3;
    j1=0;

```

```

    if j==3;
    j1=3;
    end;
    jp1=(j+1)-j1;
    j2=0;
    if jp1==3;
    j2=3;
    end;
    jp2=(jp1+1)-j2;
    bj=y(jp1)-y(jp2);
    cj=x(jp2)-x(jp1);

Ae(i,j)=-(pe*(bi*bj+ci*cj))/(4*Area);
Kdel(i,j)=-Ae(i,j);

    if i==j;
        Ke(i,j)=qe*(Area/6);
        Ae(i,j)=Ae(i,j)+(ko^2)*qe*(Area/6);
    else;
        Ke(i,j)=qe*(Area/12);
        Ae(i,j)=Ae(i,j)+(ko^2)*qe*(Area/12);
    end;

% Assemble the Element matrices into the Global FEM System:
%=====
    A(n(i,e),n(j,e))=A(n(i,e),n(j,e))+Ae(i,j);
    Kdel(n(i,e),n(j,e))=Kdel(n(i,e),n(j,e))+Kdel(i,j);
    K(n(i,e),n(j,e))=K(n(i,e),n(j,e))+Ke(i,j);
    end;
end;

K_TE=K;
Kdel_TE=Kdel;
A_TE=A;
K_TM=K(non_cond,non_cond);
Kdel_TM=Kdel(non_cond,non_cond);
A_TM=A(non_cond,non_cond);
eig_squares_TE=eig(Kdel_TE,K_TE);
eig_values_indices_TE=find(eig_squares_TE >= 0.00001);
eig_values_TE=sqrt(eig_squares_TE(eig_values_indices_TE));
[eig_values_TE_sorted,index_sorted]=sort(eig_values_TE);

figure(1)
plot(eig_values_TE_sorted,'*');
xlabel('The Modes (TE case)')
ylabel('The eigen values');
title('Eigen values for TE modes in a rectangular waveguide');
grid;
legend('a=1.5 cm and b=.75 cm');

[eig_vectorte,eig_valuete]=eig(Kdel_TE,K_TE);
eig_vector_TE=eig_vectorte(:,eig_values_indices_TE);
eig_vector_TE=eig_vector_TE(:,index_sorted);

eig_vector_TE2=eig_vector_TE(:,1);

```

```

for ii=1:total_global_num;
    eig_vec_TE_matrix(1+fix((ii-1)/(cut+1)),rem(ii-1, (cut+1))+1)=(eig_vector_TE2(ii,1)^2);
end;

figure(10)
surfc(eig_vec_TE_matrix);
colormap jet
shading interp

eig_vector_TE2=eig_vector_TE(:,2);

for ii=1:total_global_num;
    eig_vec_TE_matrix(1+fix((ii-1)/(cut+1)),rem(ii-1, (cut+1))+1)=(eig_vector_TE2(ii,1)^2);
end;

figure(20)
surfc(eig_vec_TE_matrix);
colormap jet
shading interp

eig_vector_TE2=eig_vector_TE(:,3);

for ii=1:total_global_num;
    eig_vec_TE_matrix(1+fix((ii-1)/(cut+1)),rem(ii-1, (cut+1))+1)=(eig_vector_TE2(ii,1)^2);
end;

figure(30)
surfc(eig_vec_TE_matrix);
colormap jet
shading interp

eig_vector_TE2=eig_vector_TE(:,4);

for ii=1:total_global_num;
    eig_vec_TE_matrix(1+fix((ii-1)/(cut+1)),rem(ii-1, (cut+1))+1)=(eig_vector_TE2(ii,1)^2);
end;

figure(40)
surfc(eig_vec_TE_matrix);
colormap jet
shading interp

figure(4)
eig_squares_TM =eig(Kdel_TM,K_TM);
eig_values_indices_TM=find(eig_squares_TM >= 0);
eig_values_TM=sqrt(eig_squares_TM(eig_values_indices_TM));
[eig_values_TM_sorted,index_sorted]=sort(eig_values_TM);

plot(eig_values_TM_sorted,'o');
xlabel('The Modes (TM case)')
ylabel('The eigen values');
title('Eigen values for TM modes in a rectangular waveguide');
grid;

```

```

legend('a=1.5 cm and b=.75 cm');

[eig_vectortm,eig_valuetm]=eig(Kdel_TM,K_TM);
eig_vector_TM=eig_vectortm(:,eig_values_indices_TM);
eig_vector_TM=eig_vector_TM(:,index_sorted);

eig_vector_TM2=eig_vector_TM(:,1);

eig_vec_TM_matrix=zeros(cut+1);

[rowtm,coltm]=size(non_cond);

for ii=1:coltm;
    eig_vec_TM_matrix(2+fix((ii-1)/(cut-1)),rem(ii-1,(cut-1))+2)=(eig_vector_TM2(ii,1)^2);
end;

figure(100)
surfc(eig_vec_TM_matrix);
colormap jet
shading interp

e_no=1:total_global_num;
table=[e_no' xnodes' ynodes'];

filename=strcat('data',str,'.mat');
save filename;

% The General A matrix
A;
% The General K matrix
K;
% The General del matrix
Kdel;
%*****
% The TE A matrix
A_TE;
% The TE K matrix
K_TE;
% The TE Kdel matrix
Kdel_TE;
%*****
% The TM A matrix
A_TM;
% The TM K matrix
K_TM;
% The TM Kdel matrix
Kdel_TM;
%*****
% The next table indicates the node coordinates.
% First column ==> Node Numbers.
% Second column ==> x coord.
% Third column ==> y coord.
table;

mm=1;
nn=0;

```

```

gamma_TE_exact(1,1)=(sqrt((mm*pi)^2+(nn*pi/0.5)^2))/a;

mm=2;
nn=0;
gamma_TE_exact(2,1)=(sqrt((mm*pi)^2+(nn*pi/0.5)^2))/a;

mm=0;
nn=1;
gamma_TE_exact(3,1)=(sqrt((mm*pi)^2+(nn*pi/0.5)^2))/a;

mm=1;
nn=1;
gamma_TE_exact(4,1)=(sqrt((mm*pi)^2+(nn*pi/0.5)^2))/a;

mm=1;
nn=2;
gamma_TE_exact(5,1)=(sqrt((mm*pi)^2+(nn*pi/0.5)^2))/a;

mm=2;
nn=1;
gamma_TE_exact(6,1)=(sqrt((mm*pi)^2+(nn*pi/0.5)^2))/a;

if cut > 6 ;
    max= 6 ;
else
    max= 3+cut-1;
end;

for q=1:max;
    error(q,1)=abs(eig_values_TE_sorted(q,1)-gamma_TE_exact(q,1));
    errorpercent(q,1)=(error(q,1)/gamma_TE_exact(q,1))*100;
end;

%Plot gamma Coefficient
filename=strcat('TEfemresult',str,'.txt')

fid = fopen(filename,'w');

figure(5);
fprintf(fid,'element # \t Gamma_TE_fem \t Gamma_TE_exact \n\n');
for q=1:max;
    fprintf(fid,'%g\t %g\t %g\n',q,eig_values_TE_sorted(q,1),gamma_TE_exact(q,1));
    fprintf('%10.0f\t %10.4f\t %10.4f\t %10.4f\t %10.4f\n',q,eig_values_TE_sorted(q,1),gamma_TE_exact(q,1),error(q,1),errorpercent(q,1));
end;
status = fclose(fid);

num=1:max;
plot(num,eig_values_TE_sorted(num,1),num,gamma_TE_exact(num,1))
xlabel('modes #')
ylabel('gamma TE field data')
grid
title('fem solution')

mm=1;

```

```

nn=1;
gamma_TM_exact(1,1)=(sqrt((mm*pi)^2+(nn*pi/0.5)^2))/a;

mm=1;
nn=2;
gamma_TM_exact(2,1)=(sqrt((mm*pi)^2+(nn*pi/0.5)^2))/a;

mm=2;
nn=1;
gamma_TM_exact(3,1)=(sqrt((mm*pi)^2+(nn*pi/0.5)^2))/a;

if cut > 3 ;
    max= 3 ;
else
    max= cut-1;
end;

for q=1:max;
    error(q,1)=abs(eig_values_TM_sorted(q,1)-gamma_TM_exact(q,1));
    errorpercent(q,1)=(error(q,1)/gamma_TM_exact(q,1))*100;
end;

%Plot gamma Coefficient
fprintf('\n');
figure(6);
filename=strcat('TMfemresult',str,'.txt')

fid = fopen(filename,'w');

fprintf(fid,'element # \t Gamma_TM_fem \t Gamma_TM_exact \n\n');
for q=1:max;
    fprintf(fid,'%g \t %g \t %g\n', q, eig_values_TM_sorted(q,1),
gamma_TM_exact(q,1));
    fprintf('%10.0f \t %10.4f \t %10.4f \t %10.4f \t %10.4f \n', q,
eig_values_TM_sorted(q,1), gamma_TM_exact(q,1), error(q,1),
errorpercent(q,1));
end;
status = fclose(fid);

num=1:max;
plot(num,eig_values_TM_sorted(num,1),num,gamma_TM_exact(num,1))
xlabel('modes #')
ylabel('gamma TM field data')
grid
title('fem solution')
disp('done')

% End of program

```

APPENDIX E

FEM TM MODE FOR DIELECTRIC

The following is the Finite Element Method for solving the Transverse Magnetic field modes written in Matlab codes with the users' modification of the waveguides index of refraction profile, which is also defined as the fictitious boundary condition of the waveguides, and the total number of element.

```
%This FEM MATLAB code can be used to solve for the TM modes of the
%homogeneous uniform dielectric filled square waveguides, with cladding
%and core
%k0=free space propagation constant
%xa=location of the left computational domain endpoint
%p=p coefficient appearing in the differential equation
%q=coeffient appearing in the differential equation
%N=number of nodes (N-1=number of layers)
%E_FEM=computed electric field (to be plotted)
%E_exact=exact analytical solution across the squares waveguide
```

```
% Initialization
%=====
clear all;
clc;

%cut= input('# of Blocks?[integer only]: ');
cut=10;
N_elements=2*(cut*cut);
total_global_num=(cut+1)^2;
lambda=1.5*10^-6; %m
ko=2*pi/lambda;
a=10*10^-6;
b=a;

aa=6*10^-6;
bb=6*10^-6;

%constants
%=====
%eps_o=8.854*10^-12;
%mu_o=(4*10^-7)*pi;
mu_r=1;
%n_index=input('enter index of refraction : ');
mu=ones(1,N_elements)*mu_r;
n_indexclad=1.458;
n_indexcore=1.466;
n_indexsubstrate=1.458;

eps_rsubstrate=(n_indexsubstrate^2);
```



```

eps_rcore=n_indexcore^2;
eps_rclad=(n_indexclad^2);

%Important definition
%=====
%disp('1 unit cell is 1 micron);
%10=>h_substrate:W_lad_thickness:w_core
%2:1:{2,4,6}
%1:1:{2,4,6,8}
%1:2:{2,4,6}

%20=>h_substrate:W_lad_thickness:w_core
%2:1:{1->8}
%1:1:{1->9}
%1:2:{1->7}

h_substrate=2;

w_clad_thickness=1;

w_core=6;
middle=cut;

%insert core n_index
%=====

eps=ones(1,N_elements);    %insert air index into system
rowcell=2*cut;
offset=0;

for tt=1:h_substrate*rowcell+offset;
    eps(1,tt)=eps_rsubstrate;
end;

for rr=0:(fix(cut/10)*(w_core+2*w_clad_thickness))-fix(cut/10)-1;
    for tt=(rr+h_substrate)*rowcell+offset+middle-
        (fix(cut/10)*(w_core+2*w_clad_thickness))+1:...
        (rr+h_substrate)*rowcell+offset+middle+(fix(cut/10)*(w_core+2*w_clad_th
        ickness));
        eps(1,tt)=eps_rclad;
    end;
end;

for rr=0:(fix(cut/10)*w_core)-1;
    for tt=(rr+h_substrate)*rowcell+offset+middle-
        (fix(cut/10)*w_core)+1:...
        (rr+h_substrate)*rowcell+offset+middle+(fix(cut/10)*w_core);
        eps(1,tt)=eps_rcore;
    end;
end;

% Initialize global matrix and vector
%=====

% Compute element matrices and assemble global matrix
% Generation of the Node Connectivity Table:

```

```

% =====

str = int2str(cut);
filename=strcat('nodeconnectivitydata',str,'.txt');

fid = fopen(filename,'w');
if cut==1;
    sk=0;
end;

for skipnum=1:(cut-1);
    sk(1,skipnum)=(cut+1)*skipnum;    % generating skip edges
end;

for aa=1:((cut^2)+(cut-1));
    if rem(aa,(cut+1));    % generating table without edges
        fprintf(fid,'%g \t %g \t %g\n',aa,aa+1,aa+cut+2);
        fprintf(fid,'%g \t %g \t %g\n',aa,aa+cut+2,aa+cut+1);
    else
        % skipped edges
    end
end;

status = fclose(fid);

fid = fopen(filename,'r');
n_a = fscanf(fid,'%g %g %g',[3 inf]); % It has rows now.
status = fclose(fid);

for e=1:N_elements;
    n(1,e)=n_a(1,e);
    n(2,e)=n_a(2,e);
    n(3,e)=n_a(3,e);
end;

% Nodes locations table:
%=====

filename=strcat('odelocationdata',str,'.txt');

fid = fopen(filename,'w');

for bb=0:b/(cut):b;
    for aa=0:a/(cut):a;
        fprintf(fid,'%g \t %g\n',aa,bb); % generating coords
    end;
end;

status = fclose(fid);

fid = fopen(filename,'r');
l_a = fscanf(fid,'%g %g',[2 inf]); % It has 2 rows now.
status = fclose(fid);

xnodes=l_a(1,:);

```

```

ynodes=l_a(2,:);

%Initialization Process:
%=====

A=zeros(total_global_num);
Kdel=zeros(total_global_num);
K=zeros(total_global_num);
Kedel=zeros(3);

%Loop through all elements:
%=====

for e=1:N_elements;

% E_z/TM polarization :
% =====

    pe=1/mu((e));
    qe=eps((e));

% Coordinates of the Element nodes:
%=====

    for i=1:3;
        x(1,i)= xnodes(1,n(i,e));
        y(1,i)= ynodes(1,n(i,e));
    end;

% Compute the Element matrix entries:
%=====

    Area=.5*abs((x(2)-x(1))*(y(3)-y(1)) - (x(3)-x(1))*(y(2)-y(1)));

    % A(n(i,e),n(i,j))=0;
    % Kdel(n(i,e),n(i,j))=0;
    % K(n(i,e),n(i,j))=0;

    for i=1:3;
        i1=0;
        if i==3;
            i1=3;
        end;
        ip1=(i+1)-i1;
        i2=0;
        if ip1==3;
            i2=3;
        end;
        ip2=ip1+1-i2;
        bi=y(ip1)-y(ip2);
        ci=x(ip2)-x(ip1);

    for j=1:3;
        j1=0;
        if j==3;
            j1=3;

```

```

end;
jp1=(j+1)-j1;
j2=0;
if jp1==3;
    j2=3;
end;
jp2=(jp1+1)-j2;
bj=y(jp1)-y(jp2);
cj=x(jp2)-x(jp1);

if i==j;
    Ae(i,j)=-(pe*(bi*bj+ci*cj))/(4*Area)+(ko^2)*((n_indexcore^2)-
        (n_indexsubstrate^2))*((qe-n_indexsubstrate^2)/(n_indexcore^2-
        n_indexsubstrate^2))*(Area/6);

    Kdel(i,j)=Ae(i,j);

else;
    Ae(i,j)=-(pe*(bi*bj+ci*cj))/(4*Area)+(ko^2)*((n_indexcore^2)-
        (n_indexsubstrate^2))*((qe-n_indexsubstrate^2)/(n_indexcore^2-
        n_indexsubstrate^2))*(Area/12);

    Kdel(i,j)=Ae(i,j);

end;

if i==j;
    Ke(i,j)=(ko^2)*(n_indexcore^2-n_indexsubstrate^2)*(Area/6);

    Ae(i,j)=Ae(i,j)+(ko^2)*(n_indexcore^2-
        n_indexsubstrate^2)*(Area/6);
else;
    Ke(i,j)=(ko^2)*(n_indexcore^2-n_indexsubstrate^2)*(Area/12);
    Ae(i,j)=Ae(i,j)+(ko^2)*(n_indexcore^2-
        n_indexsubstrate^2)*(Area/12);
end;

% Assemble the Element matrices into the Global FEM System:
%=====

A(n(i,e),n(j,e))=A(n(i,e),n(j,e))+Ae(i,j);
Kdel(n(i,e),n(j,e))=Kdel(n(i,e),n(j,e))+Kdel(i,j);
K(n(i,e),n(j,e))=K(n(i,e),n(j,e))+Ke(i,j);
end;
end;

end;

%Solving the assembled FEM matrix with secular eigenvalues equation
%=====
K_TM=K;
Kdel_TM=Kdel;
A_TM=A;

eig_squares_TM=eig(Kdel_TM,K_TM);
eig_values_indices_TM=find(eig_squares_TM >= 0);

```

```

eig_values_TM=sqrt(eig_squares_TM(eig_values_indices_TM));
[eig_values_TM_sorted,index_sorted]=sort(eig_values_TM);

if isempty(eig_values_TM_sorted)
    fprintf(' \n NO PROPAGATION MODE! \n\n');
end;

%Plot all the sorted TM modes that exists in the waveguides
%=====
figure(1)
plot( eig_values_TM_sorted,'*');
xlabel('The Modes (TM case)')
ylabel('The eigen values');
title('Eigen values for TM modes in a rectangular waveguide');
grid;
legend('a = b');

[eig_vectortm,eig_valuetm]=eig(Kdel_TM,K_TM);
eig_vector_TM=eig_vectortm(:,eig_values_indices_TM);
eig_vector_TM=eig_vector_TM(:,index_sorted);

eig_vector_TM2=eig_vector_TM(:,1);

for ii=1:total_global_num;
    eig_vec_TM_matrix(1+fix((ii-1)/(cut+1)),rem(ii-1,(cut+1))+1)=(eig_vector_TM2(ii,1));
end;

%3D surface plot the TM modes that exists in the waveguides in order
%=====
figure(11)
surfc(eig_vec_TM_matrix)
drawnow
colormap jet
shading interp
eig_values_TM_sorted
beta_over_k=sqrt(eig_values_TM_sorted*(n_indexcore^2-
n_indexsubstrate^2)+n_indexsubstrate^2)

end;

%Plot gamma Coefficient
%=====

figure(5)
num=1:max;
plot(num,eig_values_TM_sorted(num,1),'-r*')
xlabel('modes #')
ylabel('gamma TM field data')
grid
title('fem solution')

% End of program

```

APPENDIX F

FEM TE MODE FOR DIELECTRIC

Matlab Finite Element Method codes for solving the Transverse Electric field modes in the users' modifiable waveguides index of refraction profile, and the total number of element.

```
%MATLAB FEM code for TE modes of the homogeneous uniform dielectric
%filled square waveguides, with cladding and core profile
%k0=free space propagation constant
%xa=location of the left computational domain endpoint
%p=p coefficient appearing in the differential equation
%q=coefficient appearing in the differential equation
%N=number of nodes (N-1=number of layers)
%E_FEM=computed electric field (to be plotted)
%E_exact=exact analytical solution across the squares waveguide

%Initialization
%=====

clear all;
clc;
%cut= input('# of Blocks?[integer only]: ');
cut=20;
N_elements=2*(cut*cut);
total_global_num=(cut+1)^2;
lambda=1.3*10^-6; %cm
ko=2*pi/lambda;
a=10*10^-6;
b=a;

%eps_o=8.854*10^-12;
%mu_o=(4*10^-7)*pi;
mu_r=1;
%n_index=input('enter index of refraction : ');
mu=ones(1,N_elements)*mu_r;
n_indexclad=1.46;
n_indexcore=1.5;
n_indexsubstrate=3;

eps_rsubstrate=(n_indexsubstrate^2);
eps_rcore=n_indexcore^2;
eps_rclad=(n_indexclad^2);

%disp('1 unit cell is 1 micron);
%10=>h_substrate:w_lad_thickness:w_core
%2:1:{2,4,6}
%1:1:{2,4,6,8}
%1:2:{2,4,6}
```

```

%20=>h_substrate:w_lad_thickness:w_core
%2:1:{1->8}
%1:1:{1->9}
%1:2:{1->7}

h_substrate=2;

w_clad_thickness=1;

w_core=6;
middle=cut;
tophat=w_clad-w_core;

%Insert cladding and core n_index
%=====

eps=ones(1,N_elements);    %insert air index into system
rowcell=2*cut;
offset=0;

for tt=1:h_substrate*rowcell+offset;
    eps(1,tt)=eps_rsubstrate;
end;

for rr=0:(fix(cut/10)*(w_core+2*w_clad_thickness))-fix(cut/10)-1;
    for tt=(rr+h_substrate)*rowcell+offset+middle-
        (fix(cut/10)*(w_core+2*w_clad_thickness))+1:(rr+h_substrate)*rowcell
        +offset+middle+(fix(cut/10)*(w_core+2*w_clad_thickness));
        eps(1,tt)=eps_rclad;
    end;
end;

for rr=0:(fix(cut/10)*w_core)-1;
    for tt=(rr+h_substrate)*rowcell+offset+middle-
        (fix(cut/10)*w_core)+1:(rr+h_substrate)*rowcell+offset+middle+(fix(c
        ut/10)*w_core);
        eps(1,tt)=eps_rcore;
    end;
end;

% Initialize global matrix and vector
%=====

% Compute element matrices and assemble global matrix

% Generation of the Node Connectivity Table:
% =====

str = int2str(cut);
filename=strcat('nodeconnectivitydata',str,'.txt');

fid = fopen(filename,'w');
if cut==1;
    sk=0;
end;

```

```

for skipnum=1:(cut-1);
    sk(1,skipnum)=(cut+1)*skipnum;    % generating skip edges
end;
for aa=1:((cut^2)+(cut-1));
    if rem(aa,(cut+1));    % generating table without edges
        fprintf(fid,'%g \t %g \t %g\n',aa,aa+1,aa+cut+2);
        fprintf(fid,'%g \t %g \t %g\n',aa,aa+cut+2,aa+cut+1);
    else
        % skipped edges
    end
end;

status = fclose(fid);

fid = fopen(filename,'r');
n_a = fscanf(fid,'%g %g %g',[3 inf]); % It has rows now.
status = fclose(fid);

for e=1:N_elements;
    n(1,e)=n_a(1,e);
    n(2,e)=n_a(2,e);
    n(3,e)=n_a(3,e);
end;

% Nodes locations table:
%=====

filename=strcat('nodelocationdata',str,'.txt');

fid = fopen(filename,'w');

for bb=0:b/(cut):b;
    for aa=0:a/(cut):a;
        fprintf(fid,'%g \t %g\n',aa,bb); % generating coords
    end;
end;

status = fclose(fid);

fid = fopen(filename,'r');
l_a = fscanf(fid,'%g %g' ,[2 inf]); % It has 2 rows now.
status = fclose(fid);

xnodes=l_a(1,:);
ynodes=l_a(2,:);

%Initialization Process:
%=====

A=zeros(total_global_num);
Kdel=zeros(total_global_num);
K=zeros(total_global_num);
Kedel=zeros(3);

```



```

%Loop through all elements:
%=====

for e=1:N_elements;

% H_z/TE polarization :
% =====

    pe=1/eps((e));
    qe=mu((e));

% Coordinates of the Element nodes:
%=====

    for i=1:3;
        x(1,i)= xnodes(1,n(i,e));
        y(1,i)= ynodes(1,n(i,e));
    end;

% Compute the Element matrix entries:
%=====

    Area=.5*abs((x(2)-x(1))*(y(3)-y(1)) - (x(3)-x(1))*(y(2)-y(1)));

    for i=1:3;
        i1=0;
        if i==3;
            i1=3;
        end;
        ip1=(i+1)-i1;
        i2=0;
        if ip1==3;
            i2=3;
        end;
        ip2=ip1+1-i2;
        bi=y(ip1)-y(ip2);
        ci=x(ip2)-x(ip1);

    for j=1:3;
        j1=0;
        if j==3;
            j1=3;
        end;
        jp1=(j+1)-j1;
        j2=0;
        if jp1==3;
            j2=3;
        end;
        jp2=(jp1+1)-j2;
        bj=y(jp1)-y(jp2);
        cj=x(jp2)-x(jp1);

    if i==j;
        Ae(i,j)=- (pe*(bi*bj+ci*cj))/(4*Area) + (ko^2)*((n_indexcore^2) -
            (n_indexsubstrate^2)*(pe)*((1/pe-
            n_indexsubstrate^2)/(n_indexcore^2-n_indexsubstrate^2))*(Area/6);

```

```

    Kedel(i,j)=Ae(i,j);

else;

    Ae(i,j)=-(pe*(bi*bj+ci*cj))/(4*Area)+(ko^2)*((n_indexcore^2)-
    (n_indexsubstrate^2)*(pe)*((1/pe-
    n_indexsubstrate^2)/(n_indexcore^2-
    n_indexsubstrate^2))*(Area/12);
    Kedel(i,j)=Ae(i,j);
end;

if i==j;
    Ke(i,j)=(ko^2)*(n_indexcore^2-n_indexsubstrate^2)*(pe)*(Area/6);
    Ae(i,j)=Ae(i,j)+(ko^2)*(n_indexcore^2-
    n_indexsubstrate^2)*(pe)*(Area/6);

else;

    Ke(i,j)=(ko^2)*(n_indexcore^2-n_indexsubstrate^2)*(pe)*(Area/12);
    Ae(i,j)=Ae(i,j)+(ko^2)*(n_indexcore^2-
    n_indexsubstrate^2)*(pe)*(Area/12);
end;

% Assemble the Element matrices into the Global FEM System:
%=====

    A(n(i,e),n(j,e))=A(n(i,e),n(j,e))+Ae(i,j);
    Kdel(n(i,e),n(j,e))=Kdel(n(i,e),n(j,e))+Kedel(i,j);
    K(n(i,e),n(j,e))=K(n(i,e),n(j,e))+Ke(i,j);
end;
end;
end;

%Solving eigenvalues equation
%=====
K_TE=K;
Kdel_TE=Kdel;
A_TE=A;

eig_squares_TE=eig(Kdel_TE,K_TE);
eig_values_indices_TE=find(eig_squares_TE >= 0.1);
eig_values_TE=sqrt(eig_squares_TE(eig_values_indices_TE));
[eig_values_TE_sorted,index_sorted]=sort(eig_values_TE);

figure(1)
plot(eig_values_TE_sorted,'*');
xlabel('The Modes (TE case)')
ylabel('The eigen values');
title('Eigen values for TE modes in a rectangular waveguide');
grid;
legend('a=1.5 cm and b=.75 cm');

[eig_vectorte,eig_valuete]=eig(Kdel_TE,K_TE);
eig_vector_TE=eig_vectorte(:,eig_values_indices_TE);

```

```

eig_vector_TE=eig_vector_TE(:,index_sorted);

eig_vector_TE2=eig_vector_TE(:,1);

for ii=1:total_global_num;
    eig_vec_TE_matrix(1+fix((ii-1)/(cut+1)),rem(ii-1,(cut+1))+1)=(eig_vector_TE2(ii,1));
end;

figure(100)
surf(eig_vec_TE_matrix);
colormap jet
shading interp

filename=strcat('data',str,'.mat');

save filename;

%*****
% The TE A matrix
A_TE;
% The TE K matrix
K_TE;
% The TE Kdel matrix
Kdel_TE;
%*****
% The next table indicates the node coordinates.
% First column ==> Node Numbers.
% Second column ==> x coord.
% Third column ==> y coord.
table;

%Plot gamma Coefficient
%=====
figure(5);

num=1:max;
plot(num,eig_values_TE_sorted(num,1))
xlabel('modes #')
ylabel('gamma TE field data')
grid
title('fem solution')

% End of program

```

APPENDIX G

FEM TM MODES CUTOFF

The FEM Matlab codes for computing the TM modes cutoff wavelength, and propagation constant. The first one is for all possible modes that exist and the latter is for the single mode cutoff wavelength.

```
%This MATLAB code can be used to find TM modes cutoff wavelength for
index profiled square waveguides
%k0=free space propagation constant
%xa=location of the left computational domain endpoint
%p=p coefficient appearing in the differential equation
%q=coefficient appearing in the differential equation
%total_global_num=number of nodes (N-1=number of layers)
%E_FEM=computed electric field (to be plotted)

%Initialization
%=====
clear all;
clc;

lambdastart=2*10^-6;
lambdastop=.5*10^-6;
lambdastep=0.1*10^-6;

%cut= input('# of Blocks?[integer only]: ');
cut=10;
N_elements=2*(cut*cut);
total_global_num=(cut+1)^2;
%System boundary
%=====
a=10*10^-6;
b=a;
bmode=zeros(N_elements,3);

%eps_o=8.854*10^-12;
%mu_o=(4*10^-7)*pi;
mu_r=1;
%n_index=input('enter index of refraction : ');
mu=ones(1,N_elements)*mu_r;
n_indexclad=1.458;
n_indexcore=1.466;
n_indexsubstrate=1.458;

eps_rsubstrate=(n_indexsubstrate^2);
eps_rcore=(n_indexcore^2);
eps_rclad=(n_indexclad^2);

%waveguide dimension
%disp('1 unit cell is 1 micron);
```

```

%10=>h_substrate:W_lad_thickness:w_core
%2:1:{2,4,6}
%1:1:{2,4,6,8}
%1:2:{2,4,6}

%20=>h_substrate:W_lad_thickness:w_core
%2:1:{1->8}
%1:1:{1->9}
%1:2:{1->7}

h_substrate=2;
w_clad_thickness=1;
w_core=6;
middle=cut;

%insert clad, core n_index
%=====

eps=ones(1,N_elements); %insert air index into system
rowcell=2*cut;
offset=0;

for tt=1:h_substrate*rowcell+offset;
    eps(1,tt)=eps_rsubstrate;
end;

for rr=0:(fix(cut/10)*(w_core+2*w_clad_thickness))-fix(cut/10)-1;
    for tt=(rr+h_substrate)*rowcell+offset+middle-
        (fix(cut/10)*(w_core+2*w_clad_thickness))+1:
        (rr+h_substrate)*rowcell+offset+middle+(fix(cut/10)*(w_core+2*w_clad
        _thickness));
        eps(1,tt)=eps_rclad;
    end;
end;

for rr=0:(fix(cut/10)*w_core)-1;
    for tt=(rr+h_substrate)*rowcell+offset+middle-
        (fix(cut/10)*w_core)+1:
        (rr+h_substrate)*rowcell+offset+middle+(fix(cut/10)*w_core);
        eps(1,tt)=eps_rcore;
    end;
end;

% Initialize global matrix and vector
%=====

for m=1:N_elements,
    gamma_TE_exact(m,1)=0;
    gamma_TM_exact(m,1)=0;
    error(m,1)=0;
end

% Compute element matrices and assemble global matrix

% Generation of the Node Connectivity Table:
% =====

```

```

str = int2str(cut);
filename=strcat('nodeconnectivitydata',str,'.txt');

fid = fopen(filename,'w');
if cut==1;
    sk=0;
end;

for skipnum=1:(cut-1);
    sk(1,skipnum)=(cut+1)*skipnum;    % generating skip edges
end;
sk;

for aa=1:((cut^2)+(cut-1));
    if rem(aa,(cut+1));    % generating table without edges
        fprintf(fid,'%g \t %g \t %g\n',aa,aa+1,aa+cut+2);
        fprintf(fid,'%g \t %g \t %g\n',aa,aa+cut+2,aa+cut+1);
    else
        % skipped edges
    end
end;

status = fclose(fid);

fid = fopen(filename,'r');
n_a = fscanf(fid,'%g %g %g',[3 inf]); % It has rows now.
status = fclose(fid);

for e=1:N_elements;
    n(1,e)=n_a(1,e);
    n(2,e)=n_a(2,e);
    n(3,e)=n_a(3,e);
end;

% Nodes locations table:
%=====

filename=strcat('nodelocationdata',str,'.txt');

fid = fopen(filename,'w');

for bb=0:b/(cut):b;
    for aa=0:a/(cut):a;
        fprintf(fid,'%g \t %g\n',aa,bb); % generating coords
    end;
end;

status = fclose(fid);

fid = fopen(filename,'r');
l_a = fscanf(fid,'%g %g',[2 inf]); % It has 2 rows now.
status = fclose(fid);

xnodes=l_a(1,:);
ynodes=l_a(2,:);

```

```

filename=strcat('TMfemresult',str,date,'.txt')

fid = fopen(filename,'a');
fprintf(fid,'lambda^-1 \t\t Normalized propagation constant(b) for mode
1, 2 and 3 \n\n');
fprintf('mode # \t normalized propagation constant(b) \t effective
index \t lambdacutoff \n\n');

for lambda=lambdastart:-lambdastep:lambdastop;
ko=2*pi/lambda;

%Initialization Process:
%=====

A=zeros(total_global_num);
Kdel=zeros(total_global_num);
K=zeros(total_global_num);
Kedel=zeros(3);

%Loop through all elements:
%=====

for e=1:N_elements;

% E_z/TM polarization :
% =====

    pe=1/mu((e));
    qe=eps((e));

% Coordinates of the Element nodes:
%=====

    for i=1:3;
        x(1,i)= xnodes(1,n(i,e));
        y(1,i)= ynodes(1,n(i,e));
    end;

% Compute the Element matrix entries:
%=====

    Area=.5*abs((x(2)-x(1))*(y(3)-y(1)) - (x(3)-x(1))*(y(2)-y(1)));

    for i=1:3;
        i1=0;
        if i==3;
            i1=3;
        end;
        ip1=(i+1)-i1;
        i2=0;
        if ip1==3;
            i2=3;
        end;
        ip2=ip1+1-i2;
        bi=y(ip1)-y(ip2);
        ci=x(ip2)-x(ip1);
    end;
end;

```

```

for j=1:3;
    j1=0;
    if j==3;
        j1=3;
    end;
    jp1=(j+1)-j1;
    j2=0;
    if jp1==3;
        j2=3;
    end;
    jp2=(jp1+1)-j2;
    bj=y(jp1)-y(jp2);
    cj=x(jp2)-x(jp1);

    if i==j;
        Ae(i,j)=- (pe*(bi*bj+ci*cj))/(4*Area)+(ko^2)*((n_indexcore^2)-
            (n_indexsubstrate)^2)*((qe-n_indexsubstrate^2)/(n_indexcore^2-
            n_indexsubstrate^2))*(Area/6);
        Kdel(i,j)=Ae(i,j);

    else;
        Ae(i,j)=- (pe*(bi*bj+ci*cj))/(4*Area)+(ko^2)*((n_indexcore^2)-
            (n_indexsubstrate)^2)*((qe-n_indexsubstrate^2)/(n_indexcore^2-
            n_indexsubstrate^2))*(Area/12);
        Kdel(i,j)=Ae(i,j);

    end;

    if i==j;
        Ke(i,j)=(ko^2)*(n_indexcore^2-n_indexsubstrate^2)*(Area/6);
        Ae(i,j)=Ae(i,j)+(ko^2)*(n_indexcore^2-
            n_indexsubstrate^2)*(Area/6);
    else;
        Ke(i,j)=(ko^2)*(n_indexcore^2-n_indexsubstrate^2)*(Area/12);
        Ae(i,j)=Ae(i,j)+(ko^2)*(n_indexcore^2-
            n_indexsubstrate^2)*(Area/12);
    end;

% Assemble the Element matrices into the Global FEM System:
%=====

    A(n(i,e),n(j,e))=A(n(i,e),n(j,e))+Ae(i,j);
    Kdel(n(i,e),n(j,e))=Kdel(n(i,e),n(j,e))+Kdel(i,j);
    K(n(i,e),n(j,e))=K(n(i,e),n(j,e))+Ke(i,j);
    end;
end;
end;

%Solving eigenvalues equation
%=====

K_TM=K;
Kdel_TM=Kdel;
A_TM=A;

```



```

eig_squares_TM=eig(Kdel_TM,K_TM);
eig_values_indices_TM=find(eig_squares_TM >= 0);
eig_values_TM=sqrt(eig_squares_TM(eig_values_indices_TM));
[eig_values_TM_sorted,index_sorted]=sort(eig_values_TM);

[max,h]=max(index_sorted);

beta_over_k=sqrt(eig_values_TM*(n_indexcore^2-
n_indexsubstrate^2)+n_indexsubstrate^2);

%Checking for cutoff wavelength
%=====
if isempty(eig_values_TM_sorted)
    fprintf('\n NO PROPAGATION MODE! for wavelength %g\n\n', lambda);
    fprintf(fid, '%g\t',1/lambda);
    fprintf(' %g\t',1/lambda);
    fprintf(fid, '%14.8f\n',0);
    fprintf(' %14.8f\n',0);
else
    figure(1)
    plot( eig_values_TM_sorted, '*');
    xlabel('The Modes (TM case)')
    ylabel('The eigen values');
    title('Eigen values for TM modes in a rectangular waveguide');
    grid;
    legend('a = b');

    fprintf(fid, '%g\t',1/lambda);
    fprintf(' %g\t',1/lambda);

    %Save Coefficient
    %=====
    for q=1:max;
        bmode(1,q)=eig_values_TM(q,1);
        fprintf(fid, '%14.8f\t',bmode(1,q));
        fprintf(' %14.8f\t',bmode(1,q));
    end;

    fprintf(fid, '\n');
    fprintf('\n');

    for q=1:max;
        bmode(1,q)=eig_values_TM(q,1);
        fprintf('%g\t %14.8f\t\t\t\t\t %14.8f\t\t\t\t\t %g\n',q,eig_values_TM(q,1),beta_over_k(q,1),lambda);
    end;
end;

end;

status = fclose(fid);

% End of program

```

```

%This MATLAB code can be used to find lambda1 and lambda2 cutoff from
%TM single mode
%k0=free space propagation constant
%xa=location of the left computational domain endpoint
%p=p coefficient appearing in the differential equation
%q=coefficient appearing in the differential equation
%N=number of nodes (N-1=number of layers)
%E_FEM=computed electric field (to be plotted)

% Initialization
%=====
clear all;
clc;

lambdastart=1.02*10^-6;
lambdastop=0.6*10^-6;
lambdastep=0.01*10^-6;

%cut= input('# of Blocks?[integer only]: ');
cut=10;
N_elements=2*(cut*cut);
total_global_num=(cut+1)^2;
a=10*10^-6;
b=a;

%eps_o=8.854*10^-12;
%mu_o=(4*10^-7)*pi;
mu_r=1;
%n_index=input('enter index of refraction : ');
mu=ones(1,N_elements)*mu_r;
n_indexclad=1.458;
n_indexcore=1.466;
n_indexsubstrate=1.458;

eps_rsubstrate=(n_indexsubstrate^2);
eps_rcore=(n_indexcore^2);
eps_rclad=(n_indexclad^2);

%disp('1 unit cell is 1 micron);
%10=>h_substrate:W_lad_thickness:w_core
%2:1:{2,4,6}
%1:1:{2,4,6,8}
%1:2:{2,4,6}

%20=>h_substrate:W_lad_thickness:w_core
%2:1:{1->8}
%1:1:{1->9}
%1:2:{1->7}

h_substrate=2;

w_clad_thickness=1;

w_core=6;
middle=cut;

```

```

%insert clad, core n_index
%=====

eps=ones(1,N_elements); %insert air index into system
rowcell=2*cut;
offset=0;

for tt=1:h_substrate*rowcell+offset;
    eps(1,tt)=eps_rsubstrate;
end;

for rr=0:(fix(cut/10)*(w_core+2*w_clad_thickness))-fix(cut/10)-1;
    for tt=(rr+h_substrate)*rowcell+offset+middle-
        (fix(cut/10)*(w_core+2*w_clad_thickness))+1:
        (rr+h_substrate)*rowcell+offset+middle+(fix(cut/10)*(w_core+2*w_clad
        _thickness));
        eps(1,tt)=eps_rclad;
    end;
end;

for rr=0:(fix(cut/10)*w_core)-1;
    for tt=(rr+h_substrate)*rowcell+offset+middle-
        (fix(cut/10)*w_core)+1:
        (rr+h_substrate)*rowcell+offset+middle+(fix(cut/10)*w_core);
        eps(1,tt)=eps_rcore;
    end;
end;

% Initialize global matrix and vector
%=====

for m=1:N_elements,
    gamma_TE_exact(m,1)=0;
    gamma_TM_exact(m,1)=0;
    error(m,1)=0;
end

% Compute element matrices and assemble global matrix

% Generation of the Node Connectivity Table:
% =====

str = int2str(cut);
filename=strcat('nodeconnectivitydata',str,'.txt');

fid = fopen(filename,'w');
if cut==1;
    sk=0;
end;

for skipnum=1:(cut-1);
    sk(1,skipnum)=(cut+1)*skipnum; % generating skip edges
end;
sk;

for aa=1:((cut^2)+(cut-1));
    if rem(aa,(cut+1)); % generating table without edges

```

```

        fprintf(fid,'%g \t %g \t %g\n',aa,aa+1,aa+cut+2);
        fprintf(fid,'%g \t %g \t %g\n',aa,aa+cut+2,aa+cut+1);
    else
        % skipped edges
    end
end;

status = fclose(fid);

fid = fopen(filename,'r');
n_a = fscanf(fid,'%g %g %g',[3 inf]); % It has rows now.
status = fclose(fid);

for e=1:N_elements;
    n(1,e)=n_a(1,e);
    n(2,e)=n_a(2,e);
    n(3,e)=n_a(3,e);
end;

% Nodes locations table:
%=====

filename=strcat('nodelocationdata',str,'.txt');

fid = fopen(filename,'w');

for bb=0:b/(cut):b;
    for aa=0:a/(cut):a;
        fprintf(fid,'%g \t %g\n',aa,bb); % generating coords
    end;
end;

status = fclose(fid);

fid = fopen(filename,'r');
l_a = fscanf(fid,'%g %g',[2 inf]); % It has 2 rows now.
status = fclose(fid);

xnodes=l_a(1,:);
ynodes=l_a(2,:);

filename=strcat('TMfemresult',str,date,'3.txt')

fid = fopen(filename,'w');
fprintf(fid,'mode # \t normalized propagation constant(b) \t effective
index \t lambdacutoff \n\n');
fprintf('mode # \t normalized propagation constant(b) \t effective
index \t lambdacutoff \n\n');

for lambda=lambdastart:-lambdastep:lambdastop;
    ko=2*pi/lambda;

%Initialization Process:
%=====

```

```

A=zeros(total_global_num);
Kdel=zeros(total_global_num);
K=zeros(total_global_num);
Kedel=zeros(3);

%Loop through all elements:
%=====

for e=1:N_elements;

% E_z/TM polarization :
% =====

    pe=1/mu((e));
    qe=eps((e));

% Coordinates of the Element nodes:
%=====

    for i=1:3;
        x(1,i)= xnodes(1,n(i,e));
        y(1,i)= ynodes(1,n(i,e));
    end;

% Compute the Element matrix entries:
%=====

    Area=.5*abs((x(2)-x(1))*(y(3)-y(1)) - (x(3)-x(1))*(y(2)-y(1)));

    for i=1:3;
        i1=0;
        if i==3;
            i1=3;
        end;
        ip1=(i+1)-i1;
        i2=0;
        if ip1==3;
            i2=3;
        end;
        ip2=ip1+1-i2;
        bi=y(ip1)-y(ip2);
        ci=x(ip2)-x(ip1);

    for j=1:3;
        j1=0;
        if j==3;
            j1=3;
        end;
        jp1=(j+1)-j1;
        j2=0;
        if jp1==3;
            j2=3;
        end;
        jp2=(jp1+1)-j2;
        bj=y(jp1)-y(jp2);
        cj=x(jp2)-x(jp1);
    end;
end;

```

```

if i==j;
    Ae(i,j)=-(pe*(bi*bj+ci*cj))/(4*Area)+(ko^2)*((n_indexcore^2)-(n_indexsubstrate^2))*((qe-n_indexsubstrate^2)/(n_indexcore^2-n_indexsubstrate^2))*(Area/6);
    Kdel(i,j)=Ae(i,j);

else;
    Ae(i,j)=-(pe*(bi*bj+ci*cj))/(4*Area)+(ko^2)*((n_indexcore^2)-(n_indexsubstrate^2))*((qe-n_indexsubstrate^2)/(n_indexcore^2-n_indexsubstrate^2))*(Area/12);
    Kdel(i,j)=Ae(i,j);

end;

if i==j;
    Ke(i,j)=(ko^2)*(n_indexcore^2-n_indexsubstrate^2)*(Area/6);
    Ae(i,j)=Ae(i,j)+(ko^2)*(n_indexcore^2-n_indexsubstrate^2)*(Area/6);
else;
    Ke(i,j)=(ko^2)*(n_indexcore^2-n_indexsubstrate^2)*(Area/12);
    Ae(i,j)=Ae(i,j)+(ko^2)*(n_indexcore^2-n_indexsubstrate^2)*(Area/12);
end;

% Assemble the Element matrices into the Global FEM System:
%=====

A(n(i,e),n(j,e))=A(n(i,e),n(j,e))+Ae(i,j);
Kdel(n(i,e),n(j,e))=Kdel(n(i,e),n(j,e))+Kdel(i,j);
K(n(i,e),n(j,e))=K(n(i,e),n(j,e))+Ke(i,j);
end;
end;
end;

%Solving eigenvalues equations
%=====
K_TM=K;
Kdel_TM=Kdel;
A_TM=A;

eig_squares_TM=eig(Kdel_TM,K_TM);
eig_values_indices_TM=find(eig_squares_TM >= 0);
eig_values_TM=sqrt(eig_squares_TM(eig_values_indices_TM));
[eig_values_TM_sorted,index_sorted]=sort(eig_values_TM);

if isempty(eig_values_TM_sorted)
    fprintf(' \n NO PROPAGATION MODE! \n\n');
else
    figure(1)
    plot(eig_values_TM_sorted,'*');
    xlabel('The Modes (TM case)')
    ylabel('The eigen values');
    title('Eigen values for TM modes in a rectangular waveguide');
    grid;
    legend('a = b');
end;

```

```

[max,h]=max(index_sorted);

beta_over_k=sqrt(eig_values_TM*(n_indexcore^2-
n_indexsubstrate^2)+n_indexsubstrate^2);

if max==1;
    fprintf(fid,'%g\t %g\t %14.8f\t\t\t
%g\n',max,eig_values_TM(max,1),beta_over_k(max,1),lambda);
    fprintf('%g\t %g\t\t\t\t\t %14.8f\t\t\t
%g\n',max,eig_values_TM(max,1),beta_over_k(max,1),lambda);

elseif max==2;
    %save Coefficient
    for q=1:max;
        fprintf(fid,'\n %g\t %g\t %14.8f\t\t\t
%g\n',q,eig_values_TM(q,1),beta_over_k(q,1),lambda);
        fprintf('\n %g\t %g\t\t\t\t\t %14.8f\t\t\t
%g\n',q,eig_values_TM(q,1),beta_over_k(q,1),lambda);
    end;

    status = fclose(fid);

    break;
end;

end;

% End of program

```

APPENDIX H

FEM TE MODES CUTOFF

The FEM Matlab codes for computing the TE modes cutoff wavelength, and propagation constant for all possible modes that exist in the waveguide.

```
%This MATLAB code is used to find all the TE mode cutoff wavelength for
%dielectrics filled square waveguides profile
%k0=free space propagation constant
%xa=location of the left computational domain endpoint
%p=p coefficient appearing in the differential equation
%q=coefficient appearing in the differential equation
%N=number of nodes (N-1=number of layers)
%E_FEM=computed electric field (to be plotted)

%Initialization
%=====
clear all;
clc;

lambdastart=2*10^-6;
lambdastop=1*10^-6;
lambdastep=0.1*10^-6;

%cut= input('# of Blocks?[integer only]: ');
cut=10;
N_elements=2*(cut*cut);
total_global_num=(cut+1)^2;

%System boundary
%=====
a=10*10^-6;
b=a;
bmode=zeros(N_elements,3);

%eps_o=8.854*10^-12;
%mu_o=(4*10^-7)*pi;
mu_r=1;
%n_index=input('enter index of refraction : ');
mu=ones(1,N_elements)*mu_r;
n_indexclad=1.458;
n_indexcore=1.466;
n_indexsubstrate=1.458;

eps_rsubstrate=(n_indexsubstrate^2);
eps_rcore=(n_indexcore^2);
eps_rclad=(n_indexclad^2);

%waveguide dimension
%disp('1 unit cell is 1 micron);
%10=>h_substrate:W_lad_thickness:w_core
%2:1:{2,4,6}
```



```

%1:1:{2,4,6,8}
%1:2:{2,4,6}

%20=>h_substrate:W_lad_thickness:w_core
%2:1:{1->8}
%1:1:{1->9}
%1:2:{1->7}

h_substrate=2;

w_clad_thickness=1;

w_core=6;
middle=cut;

%insert core n_index
%=====

eps=ones(1,N_elements); %insert air index into system
rowcell=2*cut;
offset=0;

for tt=1:h_substrate*rowcell+offset;
    eps(1,tt)=eps_rsubstrate;
end;

for rr=0:(fix(cut/10)*(w_core+2*w_clad_thickness))-fix(cut/10)-1;
    for tt=(rr+h_substrate)*rowcell+offset+middle-
        (fix(cut/10)*(w_core+2*w_clad_thickness))+1:(rr+h_substrate)*rowcell
        +offset+middle+(fix(cut/10)*(w_core+2*w_clad_thickness));
        eps(1,tt)=eps_rclad;
    end;
end;

for rr=0:(fix(cut/10)*w_core)-1;
    for tt=(rr+h_substrate)*rowcell+offset+middle-
        (fix(cut/10)*w_core)+1:(rr+h_substrate)*rowcell+offset+middle+(fix(c
        ut/10)*w_core);
        eps(1,tt)=eps_rcore;
    end;
end;

% Initialize global matrix and vector
%=====

for m=1:N_elements,
    gamma_TE_exact(m,1)=0;
    error(m,1)=0;
end

% Compute element matrices and assemble global matrix

% Generation of the Node Connectivity Table:
% =====

str = int2str(cut);
filename=strcat('nodeconnectivitydata',str,'.txt');

```

```

fid = fopen(filename,'w');
if cut==1;
    sk=0;
end;

for skipnum=1:(cut-1);
    sk(1,skipnum)=(cut+1)*skipnum;    % generating skip edges
end;

for aa=1:((cut^2)+(cut-1));
    if rem(aa,(cut+1));    % generating table without edges
        fprintf(fid,'%g \t %g \t %g\n',aa,aa+1,aa+cut+2);
        fprintf(fid,'%g \t %g \t %g\n',aa,aa+cut+2,aa+cut+1);
    else
        % skipped edges
    end
end;

status = fclose(fid);

fid = fopen(filename,'r');
n_a = fscanf(fid,'%g %g %g',[3 inf]); % It has rows now.
status = fclose(fid);

for e=1:N_elements;
    n(1,e)=n_a(1,e);
    n(2,e)=n_a(2,e);
    n(3,e)=n_a(3,e);
end;

% Nodes locations table:
%=====

filename=strcat('nodelocationdata',str,'.txt');

fid = fopen(filename,'w');

for bb=0:b/(cut):b;
    for aa=0:a/(cut):a;
        fprintf(fid,'%g \t %g\n',aa,bb); % generating coords
    end;
end;

status = fclose(fid);

fid = fopen(filename,'r');
l_a = fscanf(fid,'%g %g',[2 inf]); % It has 2 rows now.
status = fclose(fid);

xnodes=l_a(1,:);
ynodes=l_a(2,:);

filename=strcat('TEfemresult',str,date,'.txt')

```

```

fid = fopen(filename,'a');
fprintf(fid,'lambda^-1 \t\t Normalized propagation constant(b) for mode
1, 2 and 3 \n\n');
fprintf('mode # \t normalized propagation constant(b) \t effective
index \t lambdacutoff \n\n');

for lambda=lambdastart:-lambdastep:lambdastop;
ko=2*pi/lambda;

%Initialization Process:
%=====

A=zeros(total_global_num);
Kdel=zeros(total_global_num);
K=zeros(total_global_num);
Kedl=zeros(3);

%Loop through all elements:
%=====

for e=1:N_elements;

% H_z/TE polarization :
% =====

    pe=1/eps((e));
    qe=mu((e));

% Coordinates of the Element nodes:
%=====

    for i=1:3;
        x(1,i)= xnodes(1,n(i,e));
        y(1,i)= ynodes(1,n(i,e));
    end;

% Compute the Element matrix entries:
%=====

    Area=.5*abs((x(2)-x(1))*(y(3)-y(1)) - (x(3)-x(1))*(y(2)-y(1)));

    for i=1:3;
        i1=0;
        if i==3;
            i1=3;
        end;
        ip1=(i+1)-i1;
        i2=0;
        if ip1==3;
            i2=3;
        end;
        ip2=ip1+1-i2;
        bi=y(ip1)-y(ip2);
        ci=x(ip2)-x(ip1);

    for j=1:3;
        j1=0;

```

```

    if j==3;
        j1=3;
    end;
    jp1=(j+1)-j1;
    j2=0;
    if jp1==3;
        j2=3;
    end;
    jp2=(jp1+1)-j2;
    bj=y(jp1)-y(jp2);
    cj=x(jp2)-x(jp1);

    if i==j;
        Ae(i,j)=-(pe*(bi*bj+ci*cj))/(4*Area)+(ko^2)*((n_indexcore^2)-(n_indexsubstrate^2)*(pe)*((1/pe-n_indexsubstrate^2)/(n_indexcore^2-n_indexsubstrate^2)))*(Area/6);
        Kdel(i,j)=Ae(i,j);
    else;
        Ae(i,j)=-(pe*(bi*bj+ci*cj))/(4*Area)+(ko^2)*((n_indexcore^2)-(n_indexsubstrate^2)*(pe)*((1/pe-n_indexsubstrate^2)/(n_indexcore^2-n_indexsubstrate^2)))*(Area/12);
        Kdel(i,j)=Ae(i,j);
    end;

    if i==j;
        Ke(i,j)=(ko^2)*(n_indexcore^2-n_indexsubstrate^2)*(pe)*(Area/6);
        Ae(i,j)=Ae(i,j)+(ko^2)*(n_indexcore^2-n_indexsubstrate^2)*(pe)*(Area/6);
    else;
        Ke(i,j)=(ko^2)*(n_indexcore^2-n_indexsubstrate^2)*(pe)*(Area/12);
        Ae(i,j)=Ae(i,j)+(ko^2)*(n_indexcore^2-n_indexsubstrate^2)*(pe)*(Area/12);
    end;

% Assemble the Element matrices into the Global FEM System:
%=====

    A(n(i,e),n(j,e))=A(n(i,e),n(j,e))+Ae(i,j);
    Kdel(n(i,e),n(j,e))=Kdel(n(i,e),n(j,e))+Kdel(i,j);
    K(n(i,e),n(j,e))=K(n(i,e),n(j,e))+Ke(i,j);
    end;
end;
end;

%Solving eigenvalues equation
%=====
K_TE=K;
Kdel_TE=Kdel;
A_TE=A;

```


APPENDIX I

WAVEGUIDE PROFILE GENERATION CODE

Listed is the FEM code for waveguides profile, or fictitious boundary condition matrix.

```
%Mesh generation code for the waveguides profile with cladding, core
and substrates
%=====
cut=10;
N_elements=2*(cut*cut);
eps_rclad=10;
eps_rcore=50;
eps_rsubstrate=10;
%disp('1 unit cell is 1 micron);
%10=>h_substrate:W_lad_thickness:w_core
%2:1:{2,4,6}
%1:1:{2,4,6,8}
%1:2:{2,4,6}
%20=>h_substrate:W_lad_thickness:w_core
%2:1:{1->8}
%1:1:{1->9}
%1:2:{1->7}

h_substrate=2;
w_clad_thickness=1;
w_core=6;
middle=cut;
tophat=w_clad-w_core;

%insert cladding, core n_index
%=====
eps=ones(1,N_elements); %insert air index into system
rowcell=2*cut;
offset=0;

for tt=1:h_substrate*rowcell+offset;
    eps(1,tt)=eps_rsubstrate;
end;

for rr=0:(fix(cut/10)*(w_core+2*w_clad_thickness))-fix(cut/10)-1;
    for tt=(rr+h_substrate)*rowcell+offset+middle-
        (fix(cut/10)*w_clad)+1:...
        (rr+h_substrate)*rowcell+offset+middle+(fix(cut/10)*w_clad);
        eps(1,tt)=eps_rclad;
    end;
end;

for rr=0:(fix(cut/10)*w_core)-1;
    for tt=(rr+h_substrate)*rowcell+offset+middle-
        (fix(cut/10)*w_core)+1:...
        (rr+h_substrate)*rowcell+offset+middle+(fix(cut/10)*w_core);
        eps(1,tt)=eps_rcore;
    end;
end;
```

APPENDIX J

3D CONTOUR PLOTTING CODE

The following are the codes for the 3D contour surface plot for both FEM solved TE and TM mode fields.

```
%Matlab codes for plotting all the solved TE modes fields in 3D surface
contour
%=====
[eig_vectorte,eig_valuete]=eig(Kdel_TE,K_TE);
eig_vector_TE=eig_vectorte(:,eig_values_indices_TE);
eig_vector_TE=eig_vector_TE(:,index_sorted);
[g,h]=max(index_sorted);

for pp=1:g;
    eig_vector_TE2=eig_vector_TE(:,pp);
    eig_vec_TE_matrix=zeros(cut+1);
    for ii=1:total_global_num;
        eig_vec_TE_matrix(1+fix((ii-1)/(cut+1)),rem(ii-
            1,(cut+1))+1)=(eig_vector_TE2(ii,1));
    end;
    num=1000+pp;
    figure(num)
    surfc(eig_vec_TE_matrix);
    colormap jet
    shading interp
end;
%end of program

%Matlab codes for plotting all the solved TM modes fields in 3D surface
contour
%=====
[eig_vectortm,eig_valuetm]=eig(Kdel_TM,K_TM);
eig_vector_TM=eig_vectortm(:,eig_values_indices_TM);
eig_vector_TM=eig_vector_TM(:,index_sorted);
[g,h]=max(index_sorted);

for pp=1:g;
    eig_vector_TM2=eig_vector_TM(:,pp);
    eig_vec_TM_matrix=zeros(cut+1);
    for ii=1:total_global_num;
        eig_vec_TM_matrix(1+fix((ii-1)/(cut+1)),rem(ii-
            1,(cut+1))+1)=(eig_vector_TM2(ii,1));
    end;
    num=2000+pp;
    figure(num)
    surfc(eig_vec_TM_matrix);
    colormap jet
    shading interp
end;

%end of program
```

APPENDIX K

MATHEMATICA PROGRAM FOR MARCATILI'S METHOD

The listed program is written in Mathematica Ver. 4.0 code for rectangular waveguides using the Marcatili's method.

```
(*Mathematica program for solving the rectangular waveguides using
  Marcatili method *)
(*user defined wavelength, index of refraction of the waveguides core,
  cladding, buffer layers *)
lambda = 2.47;
nclad = 1.458;
ncore = 1.466;

(*Newton-Raphson iteration method to solve the waveguide dispersion
  equations *)
FindRoot[{kx*(6*10^0) - (1 - 1)*Pi/2 - ArcTan[(ncore/nclad)^2 *
  Sqrt[(2*Pi/lambda*10^0)^2*(ncore^2 - nclad^2) - kx^2] / (kx^2)] == 0,
  ky*(6*10^0) - (1 - 1)*Pi/2 -
  ArcTan[Sqrt[(2*Pi/lambda*10^0)^2*(ncore^2 - nclad^2) - ky^2] / (ky^2)] == 0},
  {kx, 0.01}, {ky, 0.01}]

{kx -> 0.181608, ky -> 0.181102}

(*formula to solve for the b, propagations constant of the respective TM modes*)
((Sqrt[(2*Pi/(lambda*10^0))^2*(ncore)^2 - (%[[1]][[2]]^2 + %[[2]][[2]]^2)] *
  (lambda*10^0)/(2*Pi))^2 - (nclad)^2)/(ncore^2 - (nclad)^2)

0.565433
```


BIBLIOGRAPHY

- ¹ E. A. J. Marcatili, "Dielectric rectangular waveguide and directional coupler for integrated optics", *The Bell Syst. Tech. J.*, **48**, 2071-2102, (1969).
- ² T. Tamir, "Integrated Optics", *Berlin:Springer-Verlag*, Chapter 2, (1975).
- ³ A. Ankiewicz and G. D. Peng, "Generalized Gaussian Approximation for single-mode fibers", *IEEE J. of Lightwave Tech.*, **LT-10**, 22-27, (1992).
- ⁴ W. A. Gambling and H. Matsumura, "Simple Characterization factor for practical single-mode fibres", *Elec. Lett.*, **13**, 691-693, (1977).
- ⁵ D. Marcus, "Gaussian Approximation of the fundamental modes of graded-index fibres", *J. of the Optical Soc. Of America*, **68**, 103-109, (1978).
- ⁶ J. E. Goell, "A circular-harmonic computer analysis of rectangular dielectric waveguides", *The Bell System Tech. J.*, **48**, 2133-2160, (1969).
- ⁷ M. D. Feit and J. A. Jr. Fleck, "Light propagation in graded-index optical fibers", *Appl. Opt.*, **17**, 3990-3998, (1978).
- ⁸ Y. Chung and N. Dagli, "An accessment of Finite Difference Beam Propagation Method", *IEEE J. of Quantum Elec.*, **QE-26**, 1335-1339, (1990).
- ⁹ M. Niederhoff, W. Heinrich, and P. Russer, "The Finite-Integration Beam Propagation Method", *IEEE MTT-S Digest*, 483-486, (1995).
- ¹⁰ Y. Tsuji, M. Koshiba, and N. Takimoto, "Finite Element Beam Propagation Method for anisotropic optical waveguides", *IEEE J. of Lightwave Tech.*, **17**, 723-728, (1999).
- ¹¹ C. H. Henry and B. H. Verbeek, "Solution for the scalar wave equation for arbitrary shaped dielectric waveguides by two-dimensional Fourier analysis", *IEEE J. of Lightwave Tech.*, **LT-7**, 308-313, (1989).
- ¹² S.J. Hewlett and F. Landouceur, "Fourier Decomposition Method applied to mapped infinite domains: scalar analysis of dielectric waveguides down to modal cut-off", *IEEE J. of Lightwave Tech.*, **LT-13**, 375-383, (1995).

- ¹³ E. Schweig and W. B. Bridges, "Computer analysis of dielectric waveguides: a finite-difference method", *IEEE Trans. On Microwave Theory and Tech.*, **MTT-32**, 531-541, (1984).
- ¹⁴ K. Bierwirth, N. Schulz, and F. Arndt, "Finite-difference analysis of rectangular dielectric waveguide structures", *IEEE Trans. On Microwave Theory and Tech.*, **MTT-34**, 1104-1114, (1986).
- ¹⁵ N. Schulz, K. Bierwirth, F. Arndt, and U. Köster, "Finite-difference method without spurious solution for the hybrid-mode analysis of diffused channel waveguides", *IEEE Trans. On Microwave Theory and Tech.*, **MTT-38**, 722-729, (1990).
- ¹⁶ H. R. Schwarz, "Finite Element Methods", *London Academic Press*, (1988).
- ¹⁷ K. S. Chiang, "Finite Element Method for cutoff frequencies of weakly guiding fibres of arbitrary cross-section", *Optical and Quantum Elec.*, **16**, 487-493, (1984).
- ¹⁸ K. S. Chiang, "Finite Element Analysis of optical fibres with iterative treatment of the infinite 2-D space", *Optical and Quantum Elec.*, **17**, 381-391, (1985).
- ¹⁹ K. S. Chiang, "Finite Element Analysis of weak guiding fibres with arbitrary refractive-index distribution", *IEEE J. of Lightwave Tech.*, **LT-4**, 980-990, (1986).
- ²⁰ D. Jimenez, E. Bartolome, M. Moreno, J. Munoz, C. Domiquez, "An integrated silicon ARROW Mach-Zehnder interferometer for sensing applications", *Optics Communications*, **132**, 437-441, (1996).
- ²¹ S. Valette, S. Renard, J. Jadot, P. Gidon, C. Erbeia, "Silicon-based integrated optics technology for optical sensor applications", *Sensors and Actuators A*, 21-23, (1990).
- ²² A. Vadekar, A. Nathan, W. Huang, "Analysis and design of an integrated silicon ARROW Mach-Zehnder micromechanical interferometer", *IEEE J. of Lightwave Tech.*, **12**, 157-162, (1994).
- ²³ D. Naghski, J. Boyd, H. Jackson, S. Sriram, S. Kingsley, J. Latess, "An integrated photonic Mach-Zehnder interferometer with no electrodes for sensing electric fields", *IEEE J. of Lightwave Tech.*, **12**, 1092-1098, (1994).
- ²⁴ E. F. Schipper, A. M. Brugman, C. Dominguez, L. M. Lechuga, P. P. H. Kooyman, and L. Greve, "The realization of an integrated Mach-Zehnder waveguide

- immunosensor in silicon technology", *Sensors and Actuators B*, **40**, 147-153, (1997).
- ²⁵ R. G. Heideman, R. P. Kooyman, and J. Greve, "Performance of a highly sensitive optical waveguide Mach-Zehnder interferometer immunosensor", *Sensors and Actuators B*, **10**, 209-217, (1993).
 - ²⁶ B. J. Luff, J. S. Wilkinson, J. Piehler, U. Hollenbach, J. Ingenhoff, and N. Fabricius, "Integrated optical Mach-Zehnder biosensor", *IEEE J. of Lightwave Tech.*, **16**, 583-592, (1998).
 - ²⁷ W. Lukosz, Ch. Stamm, H. R. Moser, R. Ryf, and J. Dübendorfer, "Difference interferometer with new phase-measurement method as integrated-optical refractometer, humidity sensor and biosensor", *Sensors and Actuators B*, **38-39**, 316-323, (1997).
 - ²⁸ E. F. Schipper, S. Rauchalles, R. P. H. Kooyman, B. Hock, and J. Greve, "The waveguide Mach-Zehnder interferometer as atrazine sensor", *Anal. Chem.*, **70**, 1192-1197, (1998).
 - ²⁹ R. Kherrat, N. Jaffrezic-Renault, P. Greco, H. Helmers, P. Benech, and R. Rimet, "Integrated optical enlarged-field interferometer used as chemical sensor", *Sensors and Actuators B*, **37**, 7-11, (1996).
 - ³⁰ M. D. Degrandpre and L. W. Burgess, "Fiber-optic FT-NIR evanescent field absorbance sensor", *Appl. Spectroscopy*, **44**, 273-279, (1990).
 - ³¹ J. D. Jackson, "Classical Electrodynamics", John Wiley & Sons Inc., 3rd Edition, (1999).
 - ³² J. D. Love and W. M. Henry, "Quantifying loss minimization in single-mode fiber tapers", *Elec. Lett.*, **22**, 912-914, (1986).
 - ³³ W. J. Stewart and J. D. Love, "Design limitation on tapers and couplers in single-mode fibre", *Proceedings of the 5th European Conf. Of Optical Comm.*, 559-562, (1985).
 - ³⁴ J. D. Love, "Application of low-loss criterion to optical waveguides and devices", *IEE Optoelec. Part J*, **136**, 225-228, (1989).
 - ³⁵ N. Nagasima and H. Suzuki, *Journal of Electrochem. Soc.: Solid-State Science and technolog*, **V121**, No. 3, 434, (1974).

- ³⁶ W. A. Pliskin and H. S. Lehman, *Journal of Electrochem. Soc.: Solid-State Science and technology*, **V112**, No. 8, 1013, (1965).
- ³⁷ R. Courant, "Variational methods for a solution of problems of equilibrium and vibrations", *Bull. Amer. Math. Soc.*, **49**, 1-23, (1943).
- ³⁸ J. H. Argyris, "Energy theorems and structural analysis", *Aircraft Engineering*, **26**, 347-356, (1954).
- ³⁹ S. C. Charpa, and R. P. Canale, "Numerical methods for engineers", McGraw-Hill, NY 2nd ed., (1988).
- ⁴⁰ R. F. Harrington, "Time-harmonic electromagnetic fields", McGraw-Hill, (1961).
- ⁴¹ I. Stakgold, "Boundary value problems of mathematical physics", *Macmillan*, NY, vol. **1 & 2**, (1968).
- ⁴² O. C. Zienkiewicz, "The finite element method", *McGraw-Hill*, NY, **3rd ed.**, (1979).
- ⁴³ J. M. Jin, "The finite element method in electromagnetics", John Wiley & Sons, NY, (1993).
- ⁴⁴ P. Silvester, "Construction of triangular finite element universal matrices", *Int. J. Numer. Methods Eng.*, **12(2)**, 237-244, 1978.
- ⁴⁵ C. J. Reddy, M. D. Deshpande, C. R. Cockrell, and F. B. Beck, "Finite element method for eigenvalue problems", *Tech. Report, NASA Tech. Paper*, **3485**, 1994.
- ⁴⁶ N. Marcuvitz, "Waveguide handbook", MIT Rad. Lab. Series, 1965.
- ⁴⁷ I. S. Duport, P. Benech, and R. Rimet, "New integrated-optics interferometer in planar technology", *Appl. Opt.*, **33**, 5954-5958, (1994).
- ⁴⁸ H. Helmers, P. Greco, R. Rustad, R. Kherrat, G. Bouvier, and P. Benech, "Performance of compact, hybrid optical evanescent-wave sensor for chemical and biological applications", *Appl. Opt.*, **35**, 676-680, (1996).
- ⁴⁹ B. Maisenhölder, H. P. Zappe, R. E. Kunz, M. Moser, and P. Riel, "Optical refractometry using a monolithically integrated Mach-Zehnder interferometer", *IEEE Transducers*, 79-80, (1997).

- ⁵⁰ R. E. Kunz, "Miniature integrated optical modules for chemical and biochemical sensing", *Sensors and Actuators B*, **38-39**, 13-28, (1997).
- ⁵¹ L. M. Lechuga, A. T. M. Lenferink, R. P. H. Kooyman, J. Greve, "Feasibility of evanescent wave interferometer immunosensors for pesticide detection: chemical aspects", *Sensors and Actuators B*, **24-25**, 762-765, (1995).
- ⁵² M. Silveira and A. Gopinath, "Analysis of dielectric guides by transverse magnetic field finite element penalty method", *IEEE J. of Lightwave Tech.*, **13**, 442-446, (1995).
- ⁵³ G. R. Hadley and R. E. Smith, "Full-vector waveguide modeling using an iterative finite-difference method with transparent boundary conditions", *IEEE J. of Lightwave Tech.*, **13**, 465-469, (1995).
- ⁵⁴ A. A. Boiarski, R. W. Ridgway, J. R. Busch, G. Turhan-Sayan, and L. S. Miller, "Integrated optic biosensor for environmental monitoring", *SPIE, OE/Fibers '91, Chem, Biochem, and Environmental Fiber Sensors III*, (1991).
- ⁵⁵ R. M. Bostock, J. D. Collier, R.-J. E. Jansen, R. Jones, D. F. Moore, and J. E. Townsend, "Silicon nitride microclips for the kinematic location of optic fibres in silicon V-shaped grooves", *J. of Micromechanics and Microengineering*, **V8**, No. 4, 343-360, (1998).
- ⁵⁶ B. Maisenhölder, H. P. Zappe, R. E. Kunz, M. Moser, P. Riel, and M. Moser, J. Edlinger, "A GaAs/AlGaAs-based refractometer platform for integrated optical sensing applications", *Sensors and Actuators B*, **38-39**, 324-329, (1997).
- ⁵⁷ D. L. Veasy, J. M. Gary, J. Amin, and J. A. Aust, "Time-dependent modeling of Erbium-doped waveguide lasers in Lithium Niobate pumped at 980 and 1480 nm", *J. of Quantum Electronics*, **33**, 1647-1662, (1997).
- ⁵⁸ T. Rasmussen, A. Bjarklev, J. H. Povlsen, O. Lumholt, and K. Rottwitt, "Numerical modeling of an integrated Erbium-doped glass laser", *Fiber and Integrated Optics*, **10**, 239-243, (1991).